Thermal Characterization and Modeling of an Energy Storage System

by

Branson Chea

A thesis submitted to the School of Graduate and Postdoctoral Studies

in partial fulfillment of the requirements for the degree of

Master of Applied Science in Mechanical Engineering

Faculty of Engineering and Applied Science

University of Ontario Institute of Technology (Ontario Tech University)

Oshawa, Ontario, Canada

September 2020

THESIS EXAMINATION INFORMATION

Submitted by: **Branson Chea**

Master of Applied Science in Mechanical Engineering

Thesis title: Thermal Characterization and Modeling of an Energy Storage System

An oral defense of this thesis took place on August 28, 2020 in front of the following examining committee:

Examining Committee:

Chair of Examining Committee	Dr. Amirkianoosh Kiani
Research Supervisor	Dr. Martin Agelin-Chaab
Examining Committee Member	Dr. Bale Reddy
Thesis Examiner	Dr. Haoxiang Lang

The above committee determined that the thesis is acceptable in form and content and that a satisfactory knowledge of the field covered by the thesis was demonstrated by the candidate during an oral examination. A signed copy of the Certificate of Approval is available from the School of Graduate and Postdoctoral Studies.

ABSTRACT

The thesis reports a virtual design tool that was developed to predict and analyze thermal loads in an electric vehicle charging system. The tool was designed using computational fluid dynamics techniques and validated with experiments to provide a system-level view of the temperature profiles of all components and airflow patterns inside the charging system. The existing configuration of the charging system indicated that the cooling was capable of maintaining a maximum surface temperature of 35.61℃ for the lithium-ion batteries. Using the virtual design tool, the placement of the air conditioner and configuration of the battery fans were modified, resulting in an improvement in the cooling distribution of the batteries where the maximum surface temperature was decreased to 34.99℃. A novel method of quantifying battery surface temperatures through the use of a Rack Cooling Index was presented for examining the cooling effectiveness in the system.

Keywords: CFD; thermal characterization; charging system; lithium-ion batteries

AUTHOR'S DECLARATION

I hereby declare that this thesis consists of original work of which I have authored. This is a true copy of the thesis, including any required final revisions, as accepted by my examiners.

I authorize the University of Ontario Institute of Technology (Ontario Tech University) to lend this thesis to other institutions or individuals for the purpose of scholarly research. I further authorize University of Ontario Institute of Technology (Ontario Tech University) to reproduce this thesis by photocopying or by other means, in total or in part, at the request of other institutions or individuals for the purpose of scholarly research. I understand that my thesis will be made electronically available to the public.

Branson Chea

STATEMENT OF CONTRIBUTIONS

I hereby certify that I am the sole author of this thesis and that no part of this thesis has been published yet. However, a technical report based on this work has been submitted to eCAMION Inc. who is the industry partner of the project. I have used standard referencing practices to acknowledge ideas, research techniques, or other materials that belong to others. Furthermore, I hereby certify that I am the sole source of the creative works and/or inventive knowledge described in this thesis.

ACKNOWLEDGEMENTS

I would like to express my sincerest gratitude to my supervisor, Dr. Martin Agelin-Chaab, who has provided me with so many valuable opportunities and guidance that I will use throughout my academic and professional career. Working with him provided me with confidence that I could complete any task given to me.

A special thank you goes to my parents and family who have given me the tools to succeed. The support that they have given me was endless all throughout my studies. There are no words that can adequately express my gratitude for all that they have done for me.

During my studies, I was met with the loss of loved ones. Naomi Benoit, who never stopped believing in me and Kim Kheang, who was so kind and honest. May they rest in peace.

Thank you to all my close friends over the years who helped me succeed, make me a better person, and impacted me in more ways than words can describe. Andre Bolt, West Rockbrune, Jules Enriquez, Sam Hasan, Thomas Brooks, Tiyaz Sariffodeen, Dan Sivekumar, Paul Saoi, and Andre Vu.

Thank you to all my lab mates who supported and inspired me to work my very hardest. Sherif Rashwan, Khaled Al-Hamed, Farid Safari, Faran Razi, Alberto Giammarini, Maan Al-Zareer, Ahmed Halabi, Naseeb Siddiqui, Bismark Addo-Binney, Hayford Awenanya, Shaurya Rana, Mert Temiz, Yarkin Gevez, and Shaimaa Seyam.

Finally, thank you to Rick Szymczyk, Mehrdad Mastali, and eCAMION Inc. for giving me such a valuable opportunity to collaborate with an impactful company. Thank you to Ontario Centre of Excellence and eCAMION Inc. for providing the funding for this research.

TABLE OF CONTENTS

LIST OF TABLES

LIST OF FIGURES

NOMENCLATURE

D_ω	Cross diffusion term
E	Energy (J)
$\vec{F}$	External body forces (N)
$\vec{g}$	Gravitational acceleration (9.81 m s^{-2})
G_k	Production of turbulent kinetic energy
G_ω	Generation of ω
I	Unit tensor
S_m	User defined function for continuity equation
S_k	User-defined source term
S_ω	User-defined source term
$T_{surface}$	Measured surface temperature of batteries (℃)
$T_{operating,max}$	Maximum operating temperature of lithium-ion batteries (℃)
$\vec{v}$	Velocity (m s^{-1})
Y_k	Dissipation due to turbulence for k
Y_ω	Dissipation due to turbulence for ω

Symbols

ρ	Density (kg m^{-1})
k	Turbulence kinetic energy (J kg^{-1})
ϵ	Turbulence dissipation rate (J kg^{-1} s^{-1})
μ	Dynamic viscosity (P)
p	Static pressure (Pa)

$\bar{\bar{\tau}}$	Stress tensor
Γ_k	Effective diffusivity of k
Γ_ω	Effective diffusivity of ω

Acronyms

A/C	Air-conditioner
CAD	Computer-Aided Design
CFD	Computational Fluid Dynamics
DES	Detached Eddy Simulation
DNS	Direct Numerical Simulation
GHG	Greenhouse gases
HVAC	Heating, Ventilation, and Air-Conditioning
LES	Large Eddy Simulation
RANS	Reynolds Averaged Navier Stokes
RCI	Rack Cooling Index
SST	Shear Stress Transport

Chapter 1: Introduction

This chapter provides a brief background, the objective, and the structure of the thesis. The goals and standards set by the Canadian government for the transportation industry is briefly discussed. Electric vehicle and charging system infrastructure development are considered as part of the proposed actions to reduce emissions. The importance of thermal management techniques are discussed and employed to analyze charging system temperature distributions.

1.1 Background

As part of Canada's proposed actions to reduce emissions, the transportation sector, which accounts for 27% of Canada's greenhouse gas (GHG) emissions is an area of emphasis [1]. This results in increased focus towards modifications to the current infrastructure of Canada's transportation sector, including public transportation expansion and developments towards electric and alternative fuel infrastructure. The Canadian government aims to reduce greenhouse gas emissions by 30 megatonnes per year through the implementation of Canada's Clean Fuel Standard [2]. As a result, it has invested and is continuing to expand electric transit systems and charging infrastructure across the country [2].

In order to achieve the goals that are set by the Government of Canada, the adoption of electric vehicles must be accompanied by several other criteria, such as the appropriate facilities and the development of standard equipment. While emphasis is being placed on electric vehicles, another critical area that will facilitate widespread adoption and advancement is charging system infrastructure.

1.1.1 Charging system infrastructure and electric vehicles

In the 19th century, electric vehicles were introduced along with the internal combustion engine (ICE) vehicles. The electric vehicles did not perform well against their fossil fuel counterparts, mainly due to the inconvenience of charging and reduced range [3]. One inconvenience widely experienced is known as range anxiety, where the driver is fearful that their electric vehicle will run out of charge before reaching the destination [4]. Additionally, refueling time for internal combustion engines is much shorter than the recharging of electric vehicle batteries. The commonly used level 1 charger, which can be plugged into a standard home outlet, is only capable of fully charging an electric vehicle in 11-16 hours [5].

One method to alleviate range anxiety is the employment of level 2 charging systems, which are capable of recharging electric vehicles in 4-8 hours. This is a reduction of 7-8 hours compared to the level 1 charging systems. The development of ultrafast charging systems is referred to as level 3 charging systems. Level 3 charging systems can significantly reduce the time to recharge an electric vehicle, capable of charging to 80% of its capacity in 30 minutes to 1 hour [5][6][7]. The challenge of ultrafast charging systems is the ability to maintain the battery life and avoid any adverse effects that could result in a decrease in battery life [8]. The battery life can also be significantly affected by the high temperatures that result from these charging systems. While the advancement of technology brings reductions in charging time for electric vehicles, there is also increasing concern over the high temperatures produced, which affect the safety, performance, and cycle life of batteries [9].

The widespread implementation of charging systems is a critical part of outfitting Canada towards a cleaner future. As more electric and alternative fuel vehicles are being advanced, the infrastructure used to support them must also advance. Charging systems are outfitted with several electrical components that work in conjunction to support the charging of the electric vehicles. One of the most important components within these charging systems are the electric batteries in their energy storage systems. The selection of batteries is important as each type of battery has advantages and disadvantages.

Several charging systems use lithium-ion batteries for charging vehicles, including the charging system studied in this thesis. Lithium-ion batteries have suitable properties that make them an excellent option for use in electric vehicles and systems for charging and discharging, for example, their high energy density and low self-discharge rate [3]. One problematic area for the implementation of lithium-ion batteries in both electric vehicles and charging systems is that their optimal operating range is temperature-dependent. The operating range of lithium-ion batteries is between 25℃ and 40℃ [10]. Therefore, charging systems as a whole must be examined to ensure that they can maintain the temperatures of the components within their desired operating temperature range.

1.1.2 Thermal management

Thermal management has many advantages. It can greatly promote the life of the lithium-ion battery and other temperature-sensitive components. Additionally, the performance of the components, if they are maintained within their desired operating range, would be utilized to the highest efficiency. In the case of lithium-ion batteries, many of which are present within the charging system studied, thermal management plays an important role. Lithium-ion batteries are susceptible to reduction in life, safety, and performance if not

maintained within their operating temperatures [11]. Using thermal management as a tool will aid in the maintenance of these devices, by promoting methods that are capable of maintaining the temperature-sensitive components within their optimal operating conditions. These reasons show the importance of developing an effective thermal management system for both a component-by-component basis and also a full system analysis. As stated earlier, this is important because the performance and life of the batteries depend on the operating temperature range. While thermal analysis of lithium-ion battery packs is common in the literature, detailed thermal analyses of charging systems at the system level are not common, partly because the technology is generally proprietary, and not published in the open literature.

1.2 Objective

The objective of the project is to develop an integrated thermal model for an electric vehicle charging system. The analysis tool will be used for predicting the thermal loads. This analysis tool will be created with ANSYS Fluent CFD software.

The project is focused on a system-level analysis of the charging system, rather than a component by component analysis. Additionally, the air circulation inside of the charging system will be analyzed to identify stagnation regions and recirculation regions since they have an impact on the temperature distribution in the system.

1.3 Thesis Structure

This thesis contains 5 chapters and one appendix. Chapter 2 contains the literature review where research conducted on electric vehicles, charging system infrastructure, lithium-ion batteries, and various thermal management systems are explored. Chapter 3 discusses the methodology of the analysis. Within the methodology, the system description will

introduce the charging system and components studied while listing the process used to obtain the heat generation values. The methodology will also include details on ANSYS Fluent software, where the numerical approach, including the equations utilized for flow, energy, and turbulence. Chapter 4 discusses the results from the simulations performed, with temperature iso-surfaces, velocity volume renderings, an analysis of surface temperatures, temperature contours, velocity streamlines, and a review of the battery surface temperatures and what methods provide optimal temperature ranges. Chapter 5 concludes the research and provides recommendations. In Appendix A, the validation procedure is discussed, with validation data for the charging and discharging cycles as well as a steady-state analysis.

Chapter 2: Literature Review

Chapter 2 presents the existing literature for electric vehicles and their battery technology, charging systems and infrastructure developments, the importance of thermal management, and various techniques used for thermal management including examining the use of CFD for Heating, Ventilation, and Air Conditioning (HVAC) systems and lithium-ion battery cooling. The literature was chosen based on the function of the analysis. Many CFD systems are designed in order to optimize cooling through convection by analyzing the velocity fields generated in certain conditions. In the case of this literature review, the CFD simulations focused on two aspects of cooling: first for human occupancy and secondly for data centers. The two subjects together provide a more in-depth look at the functionality of CFD simulations and what they can be utilized for.

2.1 Electric Vehicles and Hybrid Electric Vehicles

Various research has been conducted on the use of rechargeable batteries in electric vehicles (EVs) and hybrid electric vehicles (HEVs). Table 1 summarizes the various research conducted for several batteries that are eligible for use in EVs and HEVs. Several advantages and disadvantages are discussed.

Table 1. EV and HEV battery type advantages, disadvantages, and properties

Battery type	Advantages	Disadvantages	Specific Energy (Wh/kg)	Energy Density (Wh/L)
Lead-acid	• Mature technology • Low initial cost • Rapid recharge capability	• Short cycle life (500 cycles) • Low specific energy	30-50 [12]	60-100 [12]
Nickel-cadmium (NiCd)	• Capable of enduring high discharge rates without losing capacity or being damaged	• Low capacity • Susceptible to memory effect (reduction in cell capacity) [13]	40-70 [14][15]	80-100 [12]
Nickel metal hydride (NiMH)	• Considered to be a battery of choice in EVs • Long cycle life (800-2000 cycles) • Environmentally friendly • Rapid recharge capability	• Expensive materials • High initial cost	60-80 [12][16]	140-300 [15][16]
Zinc halogen ($ZnBr_2$)	• Low material cost • Rapid recharge capability	• Low specific power • Requires frequent maintenance	65-75 [12]	60-70[12]
Lithium polymer (LiPo)	• High specific energy and energy density	• Short life cycle • Poor low-temperature performance (range of 60-80℃)	100-146 [17][18]	120-373 [17][18]
Lithium-ion (Li-ion)	• High specific energy and energy density in comparison to others on the list • Long cycle life	• High initial cost • Small operating range (range of 25-40℃) [19][9][20][10]	100-200 [21][22][23]	200-280 [21][23] [12]

In Table 1 it can be observed that the lithium-ion battery is one of the more popular choices in EVs and HEVs where they have begun to be implemented in vehicles. There is, however, some hesitance towards the full adoption of lithium-ion batteries in EVs and HEVs due to their limited driving range as well as the length of time for a full recharge [24][6][25]. The adoption of EVs is also hampered by the fragmented charging stations distributed throughout the regions that are aiming to fully adopt them, with long-range driving being the most susceptible [25].

2.2 Charging System Infrastructure

Common technology currently developed for charging systems can be categorized into three levels. Level 1 and level 2 charging systems are capable of charging EVs and HEVs to full within 2-11 hours, while level 3 fast charging systems can reduce that time to approximately 30 minutes to 1 hour [5][6][7]. These advancements assist tremendously in promoting the adoption of EVs and HEVs as the current charging system technology, and quantity restrict local and long-distance driving.

Charging system research is mainly focused on the internal components. Some advancements include the focus on improvements in the controller to maintain grid balance during different charging scenarios and maintain the battery temperature within its operating limits [26]. Other internal research focuses on the storage ability and grid impact through various changes in the hardware block (which communicates between vehicle and grid) to guarantee safe and reliable operation [27]. Control strategies for AC/DC and DC/DC converters are also developed based on existing architecture to reduce costs and improve reliability [28][29]. Another cost reduction method was the investigation of electrical storage systems, which additionally aided in reducing the impact on the grid [30].

The existing literature examines not only the internal structure of the charging systems but also the distribution of charging systems throughout the regions that will utilize the energy. Location placement is deemed critical for ease of access to charging systems, which enable drivers to move around freely without having to worry about recharging [31]. The placement of charging stations will help further develop EVs as it makes the use of them more convenient and creates a more efficient traffic network [32]. The convenience of charging is consequential to the driver's ability to freely access charging systems, which affects traffic conditions and performance. Several other models incorporate the use of parking locations, estimated demand, accessibility, local employment, and population to identify optimal locations for charging infrastructure installation [33]. A charging infrastructure model also considered the energy consumption required in specific routes and used that to plan for an optimal charging system coverage area [34]. It is common to see charging system infrastructure incorporating the use of energy storage systems. Within these energy storage systems, lithium-ion batteries are a common choice [35][36][37]. Although research for charging system infrastructure is common, it was identified that there is no extensive research focusing on the thermal distribution within these charging systems.

2.3 Lithium-Ion Batteries

Lithium-ion batteries are a popular choice for integration with hybrid electric vehicles (HEVs) and electric vehicles (EVs) due to their favourable qualities such as high specific energy and energy density [10][20][38][39][40] as well as low self-discharge rates when compared to their nickel-metal hydride counterparts [20]. The use of lithium-ion batteries does not come without disadvantages as it is still encountering issues for widespread

adoption, such as susceptibility to high and low temperatures as the range of optimal operation is between 25-40℃ [9][10][19][20] and the temperature distribution from the pack to pack should be maintained at 5℃ or less [9][10][20]. Temperature plays a crucial role in the operation, efficiency, reliability, and expected life [9] of the battery. Degradation of the lithium-ion battery is also noted to be heavily affected by temperature, current rates, and state of charge (SOC) where internal aging caused by this can reduce precision in estimating battery life [40][41].

Lithium-ion batteries are a widely researched topic with focus placed on various aspects, such as the internal structure. For example, the anode materials undergo research to identify if they are capable of improving or prolonging the lifetime of the battery. One case applied a technique that coated the anode material to strengthen its already favourable properties. Tamirat et al. [42] conducted research on a Mg_2Si coating on the anode of lithium-ion batteries to enhance stability over various applied charge rates. Additionally, many heat dissipation techniques are researched for the internal structure, such as the research performed by Ye et al. [43], which focuses on the heat dissipation structure of the battery pack. An area of emerging focus is the research conducted for external thermal management techniques that focus on heat dissipation and management through external methods.

2.4 Thermal Management

The nuances of lithium-ion batteries necessitate the aid of thermal management, which is a widely utilized and researched method. In the case of lithium-ion batteries, due to their narrow operating temperature range, there is a growing need to apply thermal management practices with the aim of maintaining the performance of the battery cells while also

increasing the lifetime without affecting safety [19][38][9][39][20][10]. The use of thermal management allows for a more in-depth understanding of the temperature distribution that results during charge and discharge cycles, as well as maintaining awareness of the sensitivity that affects life, efficiency, reliability, and safety of the batteries [38][20].

Thermal management techniques are practiced through physical and virtual methods. Physical experiments have been constructed to identify effective methods of thermal management. The use of virtual tools, such as CFD, can prove to be effective as it has become a part of engineering design, which allows it to have an influence on assessing the performance of new devices and processes before they are physically introduced [44]. These advantages allow for flexibility where condition alterations can result in reduced costs, ease of implementation, and increased safety [45][46][47][48].

In the researched literature, it is common to see physical models that utilize forced air convection to cool battery packs [49][50][51][52]. It is also common to see the use of virtual methods through CFD testing. It has been found that the use of CFD is capable of reasonably agreeing with experimental methods where Li et al. [50] noted that the experimental results were able to confirm the CFD model with a maximum error estimated to be 5-10%. Sun et al. [53] determined that there was a 5% change between simulation and experiment when analyzing a lithium-ion battery that undergoes several driving cycles. Xie et al. [54] examined several parameters to determine the optimal configuration that resulted in the greatest heat dissipation when using forced air cooling, where the configuration of 2.5° inlet and 2.5° outlet resulted in a temperature decrease of 12.82% and 29.72%, respectively. In addition to thermal management for lithium-ion batteries, the analysis of air conditioners in rooms is widely researched.

Additional CFD models were used to develop thermal management systems using phase change materials (PCM) as a passive cooling management system. Greco et al. [55] used this system to identify the cooling effectiveness for lithium-ion batteries by installing heat pipes that produced desirable conductive heat transfer from the battery cell, where it was noted that a decrease of 20℃ was possible in the tested configuration compared to one that relied on convective cooling. Ramandi et al. [56] used a CFD model to analyze a double series PCM shell configuration that was capable of delaying the battery temperature change for up to 1.5 hours by using the PCM to absorb heat generated from the battery. Wu et al. [57] developed a paraffin/expanded graphite PCM module that was tested as a CFD model, where varying PCM materials were tested with and without the module. It was found that the inclusion of the module was capable of preventing high temperatures from developing in the battery cells, while also reducing the requirement for PCM materials with high heat transfer coefficient properties.

The charging system studied features both requirements of lithium-ion battery and electrical component cooling while contained within a room-like enclosure, where the main modes of cooling are via the air conditioner and circulation fans. The following literature examines the use of CFD in room cooling and also its use as a design tool.

2.5 CFD Utilized for Room or Single Location Analysis

The first CFD simulation involves analyzing heat loads generated in servers, conducted by Mikjaniec et al. [58]. In server rooms, there is a combination of ceiling, floor, and ductwork arrangements. This paper determined a design that was able to provide cooling based on the configuration of the data center presented. After developing a dropped ceiling design, outlet vents were modeled.

In this case, two dropped ceiling designs were modeled with the same vent configuration, and it was determined that at a ceiling drop of 1 ft, the temperature contours showed cooler air distributions [58]. Duct design was a secondary analysis, where exhaust flow was modeled.

The analysis proves that the adjustment of boundary conditions can be valuable in obtaining information on the effectiveness of configurations. It did not discuss the use of tools to identify other ductwork designs and capability for altering ceiling heights.

The second review features a human occupancy analysis, conducted by Serra et al. [59], where an occupant and a simulated heating load are used an office room. A specified supply and exhaust vent are placed in the room to determine the effect of cooling via displacement or mixing. The boundary conditions of importance used in this simulation are the conditions of a constant human temperature set to be 36℃, and a heat flux representing the human heat generation was set to be 100 W/m^2 [59].

The displacement ventilation was used with a radiative ceiling. The air is supplied closer to the ground level and causes circulation within the office room via buoyancy flow. The mixing method uses a larger supply from the inlet and outlet vents stationed in the room [59]. The authors noted that the vents were positioned in the same wall for both displacement and mixing simulations. However, the vents were positioned closer to the floor for the displacement analysis and closer to the ceiling for the mixing analysis.

The mixing simulation was noted to create the most uniform distribution in the office room, Serra et al. [59] noted that the efficiency of the mixing was highly dependent on the positioning of the inlet and outlet vents. Another conclusion found was that the priority of

the user affected what method should be chosen. The displacement approach has better efficiency primarily during cooling, but the mixing method behaves better in the office setting when cooling and heating methods need to be utilized, such as, during different periods of the year [59].

A review of the cooling effect on the human simulated was not included in the analysis. It is important to view the surface skin temperature of the human in those cases and if there are any imbalances in their cooling. For example, if their torso experiences higher temperatures than their legs. The authors were able to determine that the positioning of the vents would affect the efficiency of the mixing and displacement ventilation, another method to evaluate the effectiveness could involve a method that analyzed the vents in various positions around the room.

Iizuka et al. [60] analyzed mixing and losses within an air-conditioned room. Two simulations were conducted where cooling and heating loads were utilized. One simulation used the presence of a wall with a window to divide the cooling and heating supply air units from each other. The window provided an area for heat transfer to occur. As well as this, the placement of two air-supply units was kept constant, one supply air unit for heating being close to the floor and another one for cooling placed in the ceiling [60]. The analysis was done to compare the mixing inside of the room if they were divided and also if they were used in combination with each other. It was found that there is a large difference in how the air is distributed in the room due to the positioning of the supply air vent and the supply air temperature [60]. The placement of the ceiling supply air for cooling performed well due to its ability to mix the interior zone of the room. However, when the division

between the cooling and heating supply was removed, it was determined that a large temperature gradient was generated [60].

Iizuka et al. tabulated the data and found that losses occurred due to the configurations where the window was not present[60]. The authors did not discuss the use of insulation to divide the two rooms and circulation fans to improve the mixing of the air. With only two cases completed, there are additional ways to identify effective methods of cooling. Such as the recommendation to employ various placements and alterations to the boundary conditions of the room, by choosing different window materials and incorporating insulation between the rooms.

A radiative ceiling was implemented for room cooling by Catalina et al. [61]. The objective of the CFD simulation was to identify the effectiveness of cooling via radiative ceiling. The simulation considered 3-D steady-state, incompressible, and turbulent flow in its analysis. The ceiling involved convection and radiation cooling methods. Various analyses were done, with airflow being a large area of research along with identifying the resulting temperature distribution.

This proved to be a valuable analysis as it allowed them to identify what configuration would be suitable for several clothing and metabolism rates for humans occupying the space [61]. The parameters that were adjusted involved the height of the ceiling, different metabolism rates, and clothing. Using these parameters and the already defined system, they determined which simulations were able to cool the highest metabolism rates [61]. Although they found this information, they found that the velocity above the floor was higher than most regions in the room, and in the case of human occupancy, it would lead

to discomfort [61]. This is one case of parameters being adjusted to determine results, but it does not analyze a constant heat generation or employ circulation fans.

Yu et al. [62] designed a cooling method for the main transformer room. In the region of study, transformer stations had difficulty with heat dissipation and cooling. The authors used this as an opportunity to develop a method where they were able to change design parameters to identify the impact of vent placement and their effects on cooling inside of the transformer room.

The transformer room was designed with the dimensions 10m×10m×12m with a transformer placed on the floor with dimensions of 5.42m×4.92m×5.63m [62]. There were cooling air inlets positioned close to the floor, where they supplied 17.78 kg/s of ventilated air. On the same walls, the outlets were positioned close to the ceiling. Yu et al. identified that the maximum allowable temperature in the room should not be more than 35℃ in the summer [62]. In this study, the change in the air inlet and outlet dimensions and placement were analyzed as the main driving forces behind the cooling of the transformers. Several dimensions were utilized, with the working area (transformer area) and the upper working area (ceiling area) used as the measurement points.

The air inlet was elevated by approximately 0.25m with every analysis. The air inlet began at a location of 0.2m and ended at 2.6m. It was found that the working area was primarily affected by the location of the air inlet vents [62]. At a location of 1m or less, the author noted that the changes were not significant, and the impact on the temperature gradient positively affected the transformer room. In cases of 1m or higher placement, the author noted that this would adversely affect the temperature distribution inside of the transformer

room as the temperature increased by approximately 3℃, compared to if the inlet was placed at 0.2m [62].

The area of the air inlet was increased from 3.25m^2 to 5.25m^2. Each measurement was taken with a slight increase in the area, where the temperature drop was noted to be incremental until the last measurement was taken where the maximum temperature drop was 1℃.

The air outlet was observed to cause several differences in temperature fields as it was moved. At the lowest point of the air outlet placement a region of high temperatures above it was observed. The authors noted that the outlet, when placed at its highest position, resulted in a reduction in high-temperature airflow and vortices at the ceiling [62].

Similar to the air inlet conditions, the air outlet dimensions were varied. It was observed that the greater the area of the vent, the lower the temperatures measured in the region of focus, similar to the air inlet dimensions. The authors noted that it is not always practical to create the largest vent sizes possible as the design must adhere to the existing building ventilation guidelines [62].

This study provided an excellent view of the nuances of inlet and outlet vent placements and their importance in separating temperature fields. The study identified that in the transformer room, there was a large divide in temperature fields, where the ceiling region was observed to be higher than the working region by almost 10-15℃ [62]. It would be ideal to employ a method that resulted in more optimal mixing within the room, such as the utilization of circulation fans as it may improve the cooling ability of the room without having to impact the dimensions of the vents (which as mentioned would have to adhere to

ventilation guidelines). In addition to this, volume-based heat generation source terms were not found to have been applied to the transformers along with material specifications, which may impact the temperature distribution inside of the room.

2.6 CFD Analysis Functioning as a Tool

The following review of literature features an analysis of tools developed in HVAC CFD simulations. There are several unique tools analyzed that aid in identifying the usefulness of implementing such a tool in other applications.

The Rack Cooling Index (RCI) was introduced by Herrlin [63][64], where it was used as a measure of cooling effectiveness in data centers. The RCI analysis focuses on the temperature sensitive components and considered the operating temperature ranges. RCI has been utilized in various data center scenarios as a method of creating performance metrics of the cooling systems present [65]. It proves to be a useful tool that is capable of providing information on the maintenance of component temperatures within the specified guidelines.

In the first review, the cooling of a data center was optimized by Herrlin [63]. Using the commonly implemented method of raised floor cooling, the effects of altering temperature and flow rates were examined. CFD simulations were used to identify what configurations resulted in optimal conditions. RCI was developed in order to quantify the effectiveness of cooling on the data center racks [66]. An examination was also done on the ability to increase airflow over standard airflow rates.

The Rack Cooling Index used in this study identified a range of high-end temperature and low-end temperature [66]. It can be determined in two ways, the RCI for the high-

temperature ranges and the low-temperature ranges. It is important to include both as electrical equipment has an operating range, which features both a minimum and maximum allowable temperature. The equation is listed in Equation 1 [66]:

$$RCI = \left[1 - \frac{Total\ Over\ Temp}{Max\ Allowable\ Temp}\right] \times 100\% \quad (1)$$

Understanding the temperature ranges and the resulting ones from the data center, one is able to determine if the data center exceeds the temperature limits defined.

The model of the data center contains 48 equipment racks, each with a constant heat generation rate that totals 192 kW [66]. The airflow used to cool the equipment is 52,190 m^3/hr [66]. The simulation features an analysis of several supply air temperatures ranging from 13℃ to 21℃ [66]. In addition to altering the supply air temperatures, the evaporator supply airflow rate was altered from 80% of the standard capacity to 140% [66].

The RCI was used to identify the effectiveness of the combinations of supply temperature and flow rate. Herrlin et al. state that an RCI of 95% is a sign of a good system design [66]. The results for the high temperature range show that an increase of 120% and 140% airflow rate results in an RCI of 100% or more, a sign of good system design, regardless of the supply air temperature [66]. At 100% airflow rate, an RCI of 100% is determined for an air temperature of 13℃ to 18℃ [66]. Using this analysis, a combination of the optimal range of flow rates and supply temperatures can be identified.

On the other hand, an analysis of the low temperature range shows reduced effectiveness for the listed configurations compared to the RCI for higher temperature range, where the supply air temperature of 21℃ achieves an RCI of 100% at any airflow rate [66]. The other supply temperatures resulted in an RCI of 83% or less [66].

Based on the results, it was determined that in order to reduce the development of high temperature ranges, there are several combinations of supply air temperature and airflow rate that result in an optimal design [66]. If the design must consider preventing the development of low range temperatures, then the number of available combinations greatly decreases. Based on an analysis of obtaining the optimal RCI for both high temperature and low temperature prevention, the supply air temperature of 21℃ and 120% of supply airflow rate was determined to provide the optimal RCI for both cases [66].

This study provides an excellent structure in identifying optimal configurations. The use of RCI proves to be an advantageous method of displaying the effects into an easy to understand method. The study focused on a symmetric data center, with components in the room being kept in an organized fashion and remaining constant. In addition to this, velocity streamlines were not analyzed to identify areas of recirculation. The presence of circulation fans may improve the RCI for both cases without altering the supply air temperature or flow rates, but its effect was not analyzed.

Murakami et al. [67] analyzed various scenarios in order to determine the effectiveness of cooling by components. The scenario involves an atrium that is open to a warm summer day. The simulation aimed to identify an ideal configuration that was capable of maintaining the room at a target temperature of 26℃ [67]. A feedback tool was used to identify the ideal configuration.

Four cases were analyzed with two cases focusing on a radiation cooling panel and a supply air cooling system as the main sources of cooling [67]. The other two cases utilize an air curtain, which prevents the hot air from outside mixing with the cooler inside air [67]. In

order to simulate heat loads in the room, sensible and latent heat loads were considered as additional boundary conditions [67].

The feedback tool was developed to allow for editing of the boundary conditions based on previous simulations. The goal of the feedback tool is to allow refinement of boundary conditions to determine a suitable set of conditions that can achieve a target temperature for the human model [67]. The tool is able to estimate and compare the effects of an additional parameter in the simulations. The tool utilized in this case began from an initial simulation that first identified the resulting temperatures [67]. The boundary conditions were altered, and the simulation restarted, which allowed the feedback tool to determine what the resulting temperature was due to the changes in the boundary condition [67].

It was found that the radiative cooling panel did not provide optimal cooling within the atrium, even after the implementation of the air curtain, the temperature within the atrium did not achieve the desired target temperature [67]. On the other hand, the analysis of the supply air cooling system was found to achieve a target temperature without the air curtain, but the distribution of air was uneven in the room, which would affect the human model [67]. The inclusion of an air curtain greatly improved the distribution of cold air in the atrium, achieving a room temperature of 24.3℃ [67]. The cooling from the radiative panel found that the temperature decrease was between 1.1℃ when the air curtain was activated [67]. The supply air cooling condition saw a decrease of 1.5℃ when the curtain was activated [67].

The importance of circulation within the room and the prevention of warm air infiltration was displayed in this study [67]. The feedback tool proved to be useful in incorporating a

flexible strategy of altering boundary conditions to identify the effectiveness of several conditions.

This study presents the use of a tool for altering boundary conditions, but it did not display the feedback tool in higher heating load scenarios, such as rooms with electrical equipment or an electric vehicle charging system. Also, the presence of circulation fans was not considered. This provides an excellent opportunity to analyze temperature loads within a charging station, as most studies involve human occupants or data centers.

Based on the literature reviews, there are no existing virtual design tools that analyze the temperature loads inside electric vehicle charging systems. Additionally, the literature for charging systems and energy storage systems did not analyze the thermal loads generated within them, instead of focusing on the control strategies and distribution. The review also revealed that the use of the RCI did not incorporate quantification of battery temperatures. Additionally, many CFD simulations did not use any forms of air circulating devices to aid in cooling within the rooms.

Chapter 3: Methodology

The methodology is discussed in this chapter, in which the system description will examine the current system and the specifications of the components to be analyzed. Along with this, a review was made of every component to determine their applicability to the heat generation within the charging system. The numerical model for flow modeling, turbulence, and energy is discussed. The chapter of methodology provides an overview of the pre-processing and solving steps that are involved in the CFD process in the thesis.

3.1 System Description

A full charging system model was used for this study, which resembles the charging system model produced by eCAMION Inc., the industry partner. The charging system model has dimensions of 2.5 m × 2.5 m × 3.0 m, and houses a variety of unique assemblies, including a lithium-ion battery energy storage system. The cooling system used is an air conditioner with a rating of 2.93kW (10,000 BTU/hr) and an air supply rate of 0.136 m^3/s (287 CFM) [68][69].

The configuration of all components within the charging system is displayed in Figure 1 where the battery configuration and safety barrier is indicated within the charging system. Note that most components in the unit are hidden for confidentiality.

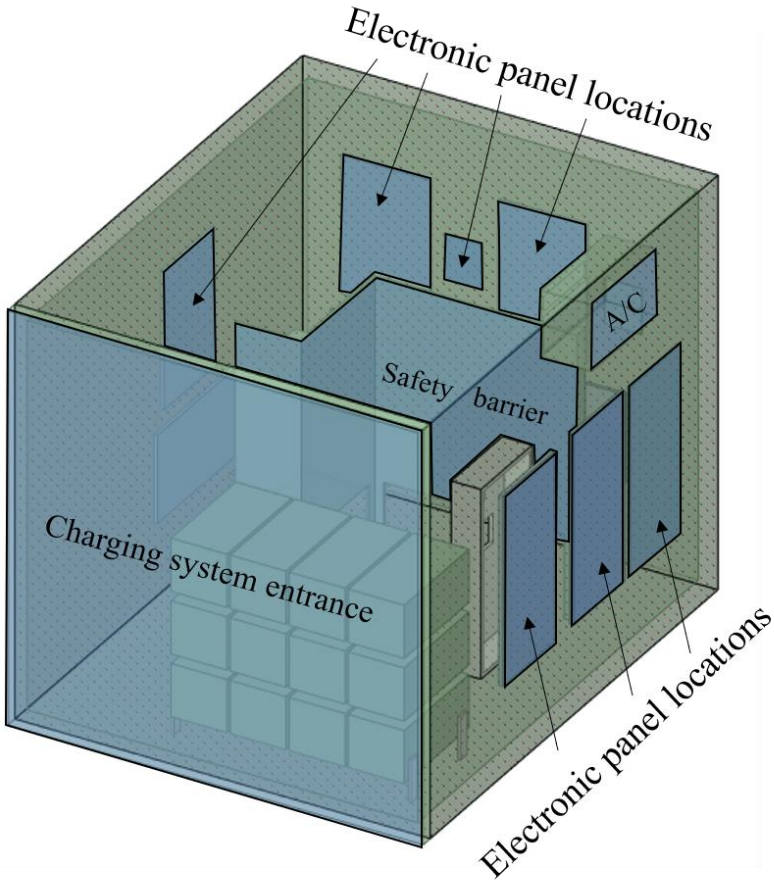

Figure 1. Battery configuration in the charging system studied with the safety barrier. Note that the electronic components in the unit are hidden for confidentiality.

A review of each component was conducted to determine its impact in the charging system through an investigation of their heat generation values and materials. In addition to this, the presence of air circulating fans were considered in the analysis.

The software used for the analysis is ANSYS Workbench and ANSYS Fluent. ANSYS Fluent is a program written in the C language that provides a variety of functions such as solver control and efficient data structures with the capability to couple with server architecture to run several processes [70]. ANSYS Fluent has the capability to solve fluid

flow, heat transfer, and chemical reaction problems. In fact, ANSYS Fluent is a Multiphysics software.

ANSYS Fluent can be accessed through an additional program, ANSYS Workbench, which provides the tools that structure workflow where easy integration between each task is capable of being transferred to the next task. The workflow in ANSYS Workbench first begins with a Computer-Aided-Design (CAD) program, SpaceClaim, then its own built-in Workbench Mesher, where it can be updated for use in ANSYS Fluent. Post-processing can be conducted using CFD-Post or within ANSYS Fluent itself.

3.2 Numerical Approach

The nature of the problem features both fluid flow and energy transfer via heat transfer. Therefore, the following equations were employed for flow, turbulence, and energy modeling.

3.2.1 Flow modeling

Equations 2 and 3 represent the continuity or conservation of mass equations. Equation 2 represents the equation in its full form, where S_m is a user-defined function, which can be developed by the user and represent any function of their choosing. Equation 3 is used when the fluid flow is deemed to be incompressible, and there are no user-defined functions employed. Equation 4 represents the momentum conservation equation.

The continuity equation is shown below [51][71]:

$$\frac{\partial \rho}{\partial t} + \nabla(\rho \vec{v}) = S_m \tag{2}$$

$$\nabla \vec{v} = 0 \tag{3}$$

The momentum conservation equation [71] can be determined from Equation 4, where the stress tensor is represented by $\bar{\bar{\tau}}$, the static pressure is represented by p, the gravitational force is $\rho\vec{g}$, and the external body forces are $\vec{F}$, the velocity vector is defined by $\vec{v}$ is represented in three dimensions for three dimensional problems.

$$\frac{\partial}{\partial t}(\rho\vec{v}) + \nabla\cdot(\rho\vec{v}\vec{v}) = -\nabla p + \nabla\cdot(\bar{\bar{\tau}}) + \rho\vec{g} + \vec{F} \tag{4}$$

The stress tensor, $\bar{\bar{\tau}}$, can be calculated by the following Equation 5, where μ is molecular velocity, and the unit tensor is represented by I [71].

$$\bar{\bar{\tau}} = \mu\left[(\nabla\vec{v} + \nabla\vec{v}^{T}) - \frac{2}{3}\nabla\cdot\vec{v}I\right] \tag{5}$$

3.2.2 Turbulence

In order to accurately solve the turbulence problems posed in CFD, the Navier-Stokes equations must be solved. The equations can be solved directly using the method known as Direct Numerical Simulation (DNS). However, DNS is computationally expensive, and hence the turbulence is usually modeled in other ways. Several turbulence models can be employed for this study, including Large Eddy Simulation (LES), Detached Eddy Simulation (DES), and Reynolds Averaged Navier-Stokes (RANS), in order of decreasing computational cost [12]. For the system-level analysis, which is the focus of this project, RANS models offer a much more economical approach to resolving turbulent flow problems. The commonly employed RANS models are the Spalart-Allmaras model, k-ϵ models, and k-ω models [70].

The Spalart-Allmaras model uses one equation to model turbulence. The use of this model was designed for use in the aeronautics and aerospace industry. ANSYS recommends

avoiding the use of this model for general purpose applications as it makes various simplifications due to its original aeronautics and aerospace focus [70]. Despite these simplifications, the Spalart-Allmaras model has fairly good results for boundary layers in select scenarios.

The k-ϵ models are a set of two-equation models that are widely used in the industry. Using k-ϵ models, two transport equations are solved, while the Eddy viscosity approach is used to identify the Reynolds stresses. Under the family of k-ϵ models is the realizable k-ϵ model, which is recommended by ANSYS when using k-ϵ models [70]. The k-ϵ models are able to provide reasonable accuracy, economy, and robustness for use in turbulent flow simulations, which helped it become popularized in industrial and heat transfer applications [70].

The final set of two-equation models are the k-ω models, which offer an improvement over the k-ϵ models, by providing the ability to solve the viscous sublayer through integration with additional terms. Although it offers this advantage, the k-ω model has a strong sensitivity to the freestream flow [70]. To combat this disadvantage, the k-ω Shear Stress Transport (SST) model was developed in 1994 by Menter et al. [72]. The solution to overcoming the freestream problem incorporates a blended function that switches between k-ϵ for freestream flow and k-ω for near wall flows.

The k-ω SST model will be employed in this study due to its proven ability to model flow and energy with robustness and a reasonable level of accuracy [73]. The equations employed are displayed below from Equation 6 to Equation 7 [71], where the production of turbulent kinetic energy is defined by G_k and ω is generated by G_ω. The dissipation due

to turbulence of k and ω is defined by Y_k and Y_ω. Any user defined source terms would be applied to S_k and S_ω.

$$\frac{\partial}{\partial t}(\rho k) + \frac{\partial}{\partial x_i}(\rho k u_i) = \frac{\partial}{\partial x_j}\left(\Gamma_k \frac{\partial k}{\partial x_j}\right) + G_k - Y_k + S_k \quad (6)$$

$$\frac{\partial}{\partial t}(\rho \omega) + \frac{\partial}{\partial x_j}\left(\rho \omega u_j\right) = \frac{\partial}{\partial x_j}\left(\Gamma_\omega \frac{\partial \omega}{\partial x_j}\right) + G_\omega - Y_\omega + D_\omega + S_\omega \quad (7)$$

3.2.3 Energy

The energy conservation equation can be defined by Equation 8 [51], where the total energy is defined by E, the density is represented by ρ, the specific heat capacity is represented by c_p, and k_T as the thermal conductivity.

$$\rho c_p \left(\frac{\partial E}{\partial t} + v_x \frac{\partial E}{\partial x} + v_y \frac{\partial E}{\partial y} + v_z \frac{\partial E}{\partial z}\right) = k_T \left(\frac{\partial^2 E}{\partial x^2} + \frac{\partial^2 E}{\partial y^2} + \frac{\partial^2 E}{\partial z^2}\right) \quad (8)$$

3.3 Computational Fluid Dynamics Analysis

To prepare the system for a CFD analysis, pre-processing is the first step, which includes the preparation of the geometry, mesh, and solver settings [74]. Following this, the solving process begins, ending with the post-processing where results are obtained and analyzed [74].

3.3.1 Geometry and defeaturing

Prior to the numerical approach, the complex geometry of various electrical components was defeatured into a simpler design to allow for meshing. The existing geometry needs to be examined for small features such as gaps or holes that make it impossible to mesh properly and must be removed.

3.3.2 Domain generation and shared topology

After defeaturing, the fluid domain must be generated. The fluid domain is generated by creating negative volumes of the objects. The domain studied features dimensions of 2500mm × 2500mm × 3000mm. Several components within the domain range from sizes of 90mm × 70mm × 30mm to 340mm × 340mm × 675mm. The combination of the negative volumes and fluid domain allows the CFD software to differentiate between the areas where the fluid can flow freely and areas where the fluid cannot flow.

Additional steps are required to prepare the geometry for the problem set-up. For example, the fan faces underwent the share topology before applying their boundary conditions. A display of the resulting shared topology for fan faces is shown in Figure 2.

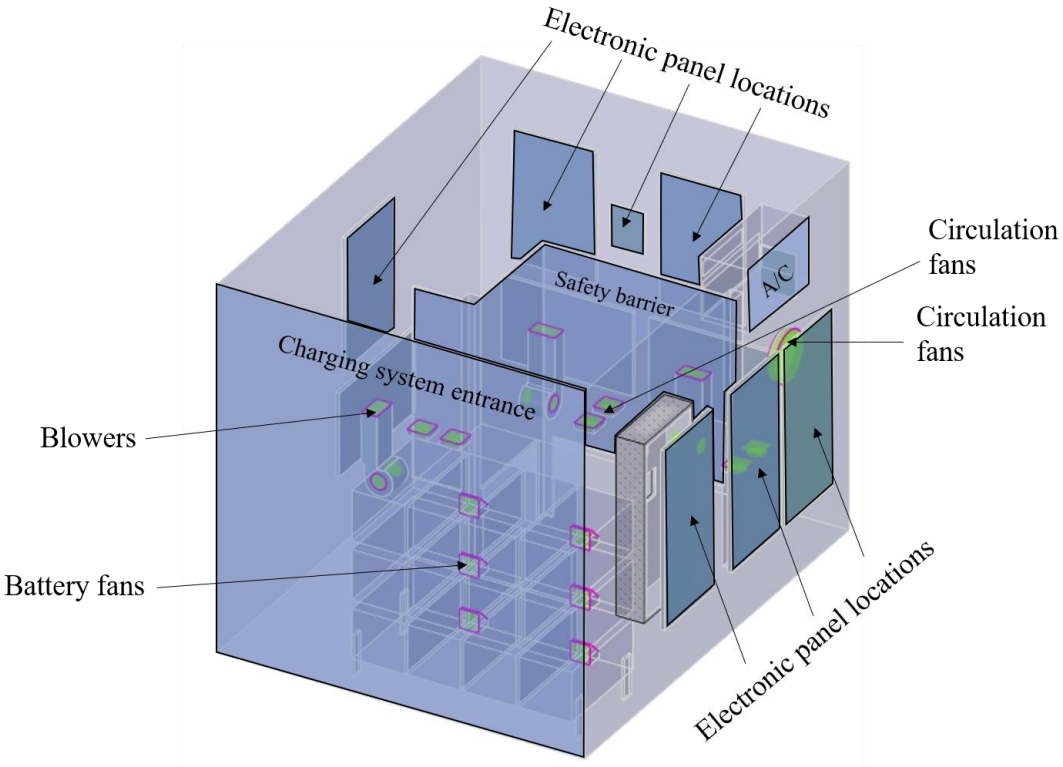

Figure 2. Shared topology with labeled fan locations. Note that most of the components of the unit are hidden for confidentiality

3.3.3 Mesh generation

3.3.3.1 Mesh independence study

A mesh independence study was conducted with 4 different mesh sizes. The outlet temperature and average battery temperature were used to monitor the convergence. These values were monitored using the area weighted average measurement method. The mesh independence study features approximately 10% changes in the total mesh size with each analysis. The coarse mesh size studied featured 25.17 million elements and the fine mesh size was generated with 38.76 million elements. As seen from Table 2, as the total mesh size increases from 25.17 million to 27.77 million, the change in temperature ranges from 2.28% to 5.26%. As it increases to 31.78 million elements, the change in temperature drops further, with the changes ranging from 0.89% to 2.02%. The final measurement featured a mesh size of 38.76 million elements, which resulted in the lowest increase recorded at 0.15% to 0.80%. These changes are also displayed in Figure 3. The time per iteration was also studied, as listed in Table 2, with each iteration ranging from 1.5 minutes to 2 minutes. It can be identified that between the mesh sizes of 27.77 million to 38.76 million, the time per iteration does not change drastically. As a result, the mesh used for this study was chosen to be 31.78 million elements to minimize computational cost while maintaining accuracy.

Table 2. Mesh independency parameters studied

Mesh Size (million)	Outlet Temperature (℃)	Battery Temperature (℃)	Time Per Iteration (mins:secs)	Percent Change Outlet (%)	Percent Change Battery (%)
25.17	26.32	34.95	1:36	N/A	N/A
27.77	26.92	33.11	1:51	2.28%	5.26%
31.78	27.16	32.44	1:53	0.89%	2.02%
38.76	27.2	32.7	1:59	0.15%	0.80%

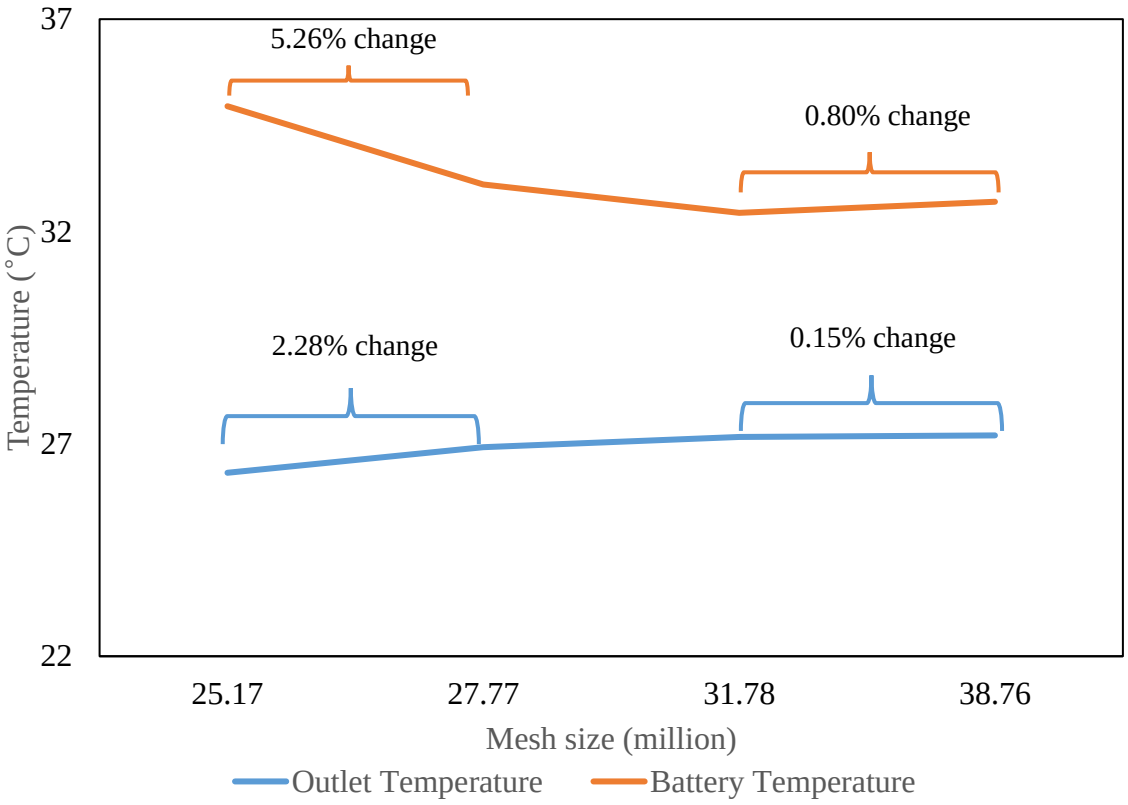

Figure 3. Temperature results from mesh independency study with respect to mesh size in the millions

3.3.3.2 Mesh details

As discussed in the mesh independence study, the resulting mesh was generated with 31.78 million elements with an average skewness of 0.23 and an average orthogonal quality of 0.77. The large number of elements is due to the range of sizes in the charging system,

beginning with the size of the charging system housing and ending with the various components housed within it, which results in the mentioned mesh size. The structure of the mesh features refinement at the body, faces, and shadow faces due to the complex heat transfer interface that was utilized. The body of each component required meshing due to the nature of the heat generated as it was specified to be volumetric heat generation that originates from the core. The face and shadow face mesh requirements are due to the interface between the solid body face and the face of the air in contact with it (known as a shadow face).

The mesh features both structured (e.g., Figure 4), and unstructured elements, which can be seen in various figures (e.g., Figure 5 and Figure 6). The majority of the mesh resulted in unstructured elements, but structured elements are most widely seen in the mesh generated on the battery solid and faces and other components that are similar to basic shapes, seen in Figure 4. Many strategies were used to produce a mesh that can obtain accurate results, one being the inclusion of refinement regions around several of the panels and the safety barrier. The importance of adding local refinement regions, especially around the safety barrier, is to allow for a finer solution resolution during computation of the problem. Lanfrit [75] discusses the advantages of using local refinement regions, although it is time-consuming, it is able to provide more accuracy compared to several of the other methods. The local refinement regions can be identified in Figure 5 and Figure 6.

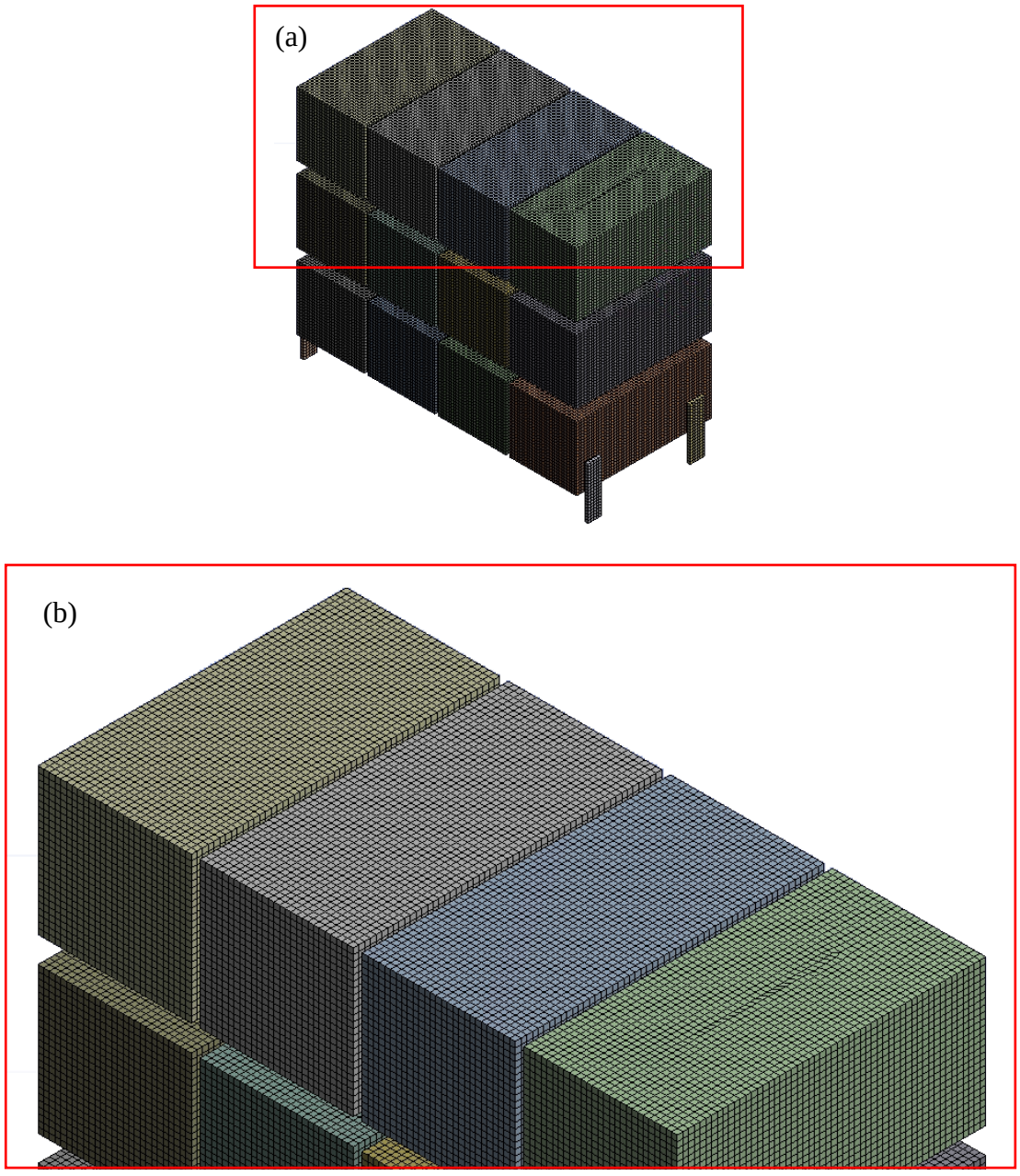

Figure 4. Structured surface mesh for the batteries (a) full view, and (b) close-up view of the red window

(a)

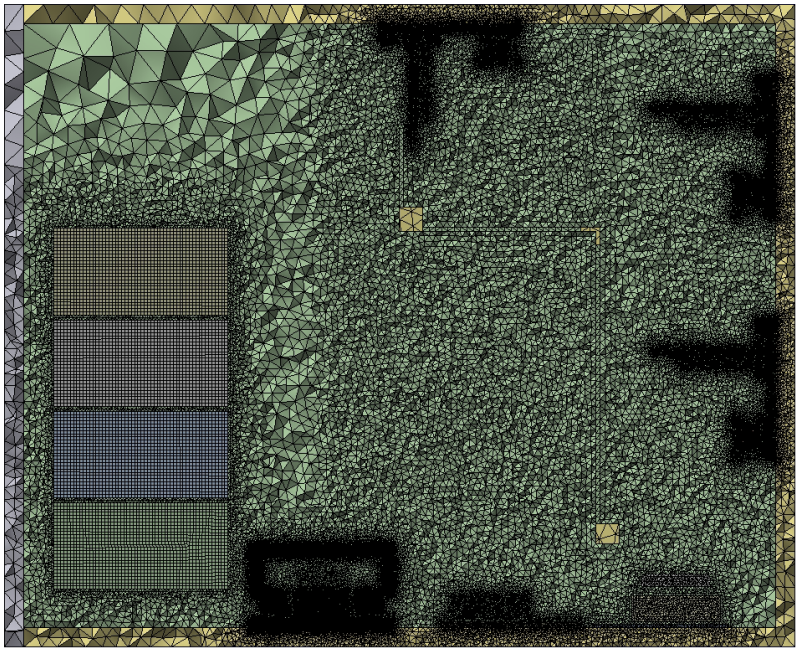

(b)

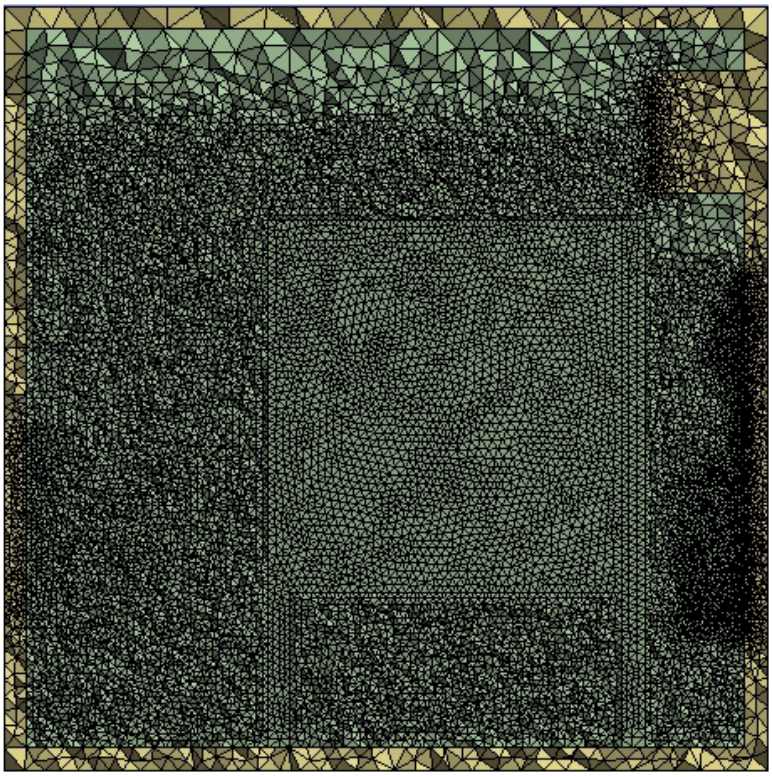

Figure 5. Image of full mesh (a) top view and (b) front view

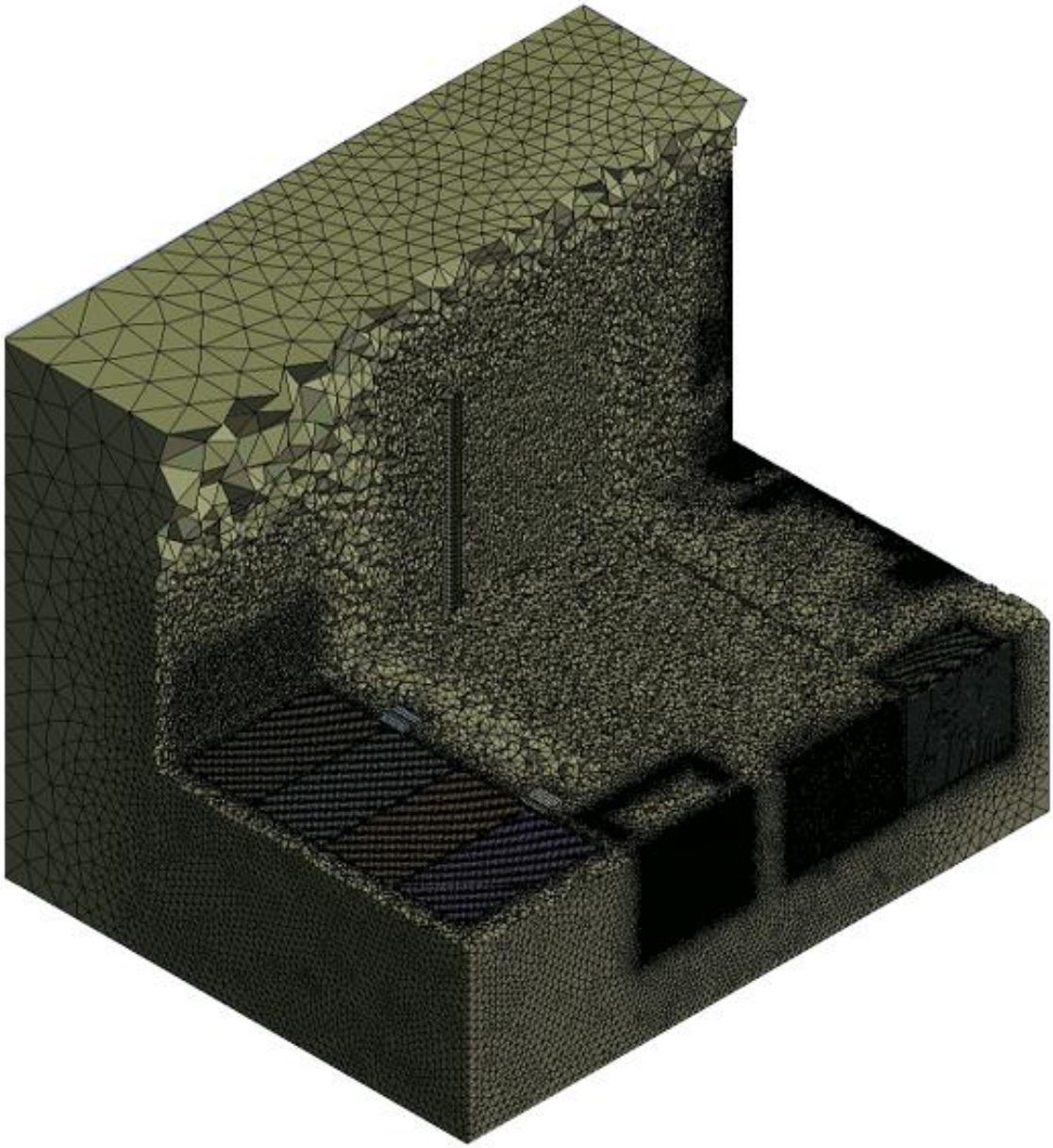

Figure 6. Three-dimensional view of volume mesh

The mesh parameters are listed in Table 3 and Table 4, where the mesh sizing is completed in millimeters. Table 3 lists the parameters for mesh sizing for the component body, face, and shadow face. Table 4 lists the mesh parameters for regions that do not meet the categorization shown in Table 3, this includes the fan and air conditioner faces. The refinement region mesh sizing parameters are included in this as well.

Table 3. Mesh parameters for body, face, and shadow faces

Component	Body Mesh Size (mm)	Face Mesh (mm)	Shadow Face Mesh (mm)
Battery	30	20	20
HVP	4	4	4
PLC	7.5	7.5	7.5
CHP	12.5	12.5	12.5
AXP	7.5	7.5	7.5
PLP	7.5	7.5	5
PDP	7.5	7.5	5
PCP	7.5	5	7.5
Container	100	-------	-------

Table 4. Mesh parameters for other components

Component	Mesh Size (mm)
Fans faces	15
Air conditioner faces	15
Refinement region	50

3.3.4 Model set up & solver settings

The model set-up and solver settings follow mesh generation. This aspect of the simulation includes the assignment of boundary conditions, materials, and interfacing contacts. Boundary conditions for the proposed virtual design tool can be broken down into the following:

1. Heat source generation
2. Inlet air conditions
3. Insulation and floor conditions
4. Fan conditions
5. Material assignments

The heat generation source terms were first identified through an analysis of each component's datasheet, which was viewed for information on its heat losses. This was

assumed to be approximate to the heat loss added into the charging system during operation. Following this, an initial simulation was performed to determine the resulting surface temperatures of the components. This initial data went through a verification process for its accuracy, after which it was adjusted to be more representative of the reported surface temperatures. The inlet air conditions were determined through an analysis of an air conditioner, with information provided by the manufacturer. The cooling capacity of the air conditioner is 2.93kW (10,000 BTU/hr) with an air supply rate of 0.136 m^3/s (287 CFM) [68], [69]. In order to make these conditions suitable for use in ANSYS Fluent, the velocity-inlet condition was used. This condition requires that a velocity parameter is input as a value and to do this, the dimensions of the air conditioner inlet were measured to be 0.03879m^2. Using the area and the inlet supply air conditions, the velocity was able to be determined to be 3.49 m/s.

The importance of insulation and floor conditions was also considered. These boundary conditions were included by applying a set of thin-wall thermal resistance parameters, which is advantageous because it does not require a thin mesh to be generated for ANSYS Fluent to recognize that it is a wall with set dimensions [70].

The final set of boundary conditions are the fan boundary conditions. The fan boundary conditions require an additional step during set-up, which was previously mentioned in Section 3.3.2. The fan boundary condition is used to calculate the flow through the desired fan regions by taking an input of a fan curve between velocity and pressure. The modeled fan in ANSYS Fluent is represented by a fan face that is infinitely thin [70], which is done by identifying the fan boundary as an interior zone using share topology as previously discussed and pictured in Figure 2.

The turbulence model used for the virtual design tool is k-ω SST, which is a two-equation RANS based model, as previously mentioned in Section 2.3.2. The boundary conditions are summarized in Table 5 and Table 6.

Table 5. Heat generation source terms categorized by the panel. Note that the component descriptions are not shown due to confidentiality.

Assembly	**Source Term** (W/m^3)
PCP	8000
	7868
	75,000
	90,000
PLP	13,500
	7868
	20,000
	7500
PLC	12,500
Batteries	1000
CHP	20,000
	7784
HVP	20,000
	4643
	40,000
	12,000
PDP	8889
	5000

Table 6. Other source terms applied

Object	Source Term Setting
Insulation	Convection coefficient: 10 W/m^{2}K
	Thickness: 30 mm
Floorboard	Convection coefficient: 10 W/m^{2}K
	Thickness: 28 mm
Outer walls	Temperature: 30 ℃
Ground	Temperature: 25 ℃
PCP fans	Pressure: 203.5 Pa
PCP blowers	Pressure: 329.5 Pa
CHP fan	Pressure: 72.5 Pa
Battery fans	Pressure: 72.5 Pa
Air conditioner	Supply air inlet: 3.49 m/s
	Supply air temperature[a]: 4.08 ℃

[a]The supply air temperature is based on the direction provided by eCAMION Inc.

Additional boundary conditions used were the assignment of materials for each component. Table 7 lists the material and assembly matches, which were determined through an analysis of each datasheet. Note that the full component names are not included due to confidentiality. Following this, the density, specific heat capacity, and thermal conductivity were identified. It was assumed that each of the components is a solid material.

Table 7. Materials and properties of components Note that the component descriptions are not shown due to confidentiality.

Assembly	Density (kg/m^3)	Specific Heat Capacity ($J/kg \cdot K$)	Thermal Conductivity ($W/m \cdot K$)
PLC	2719	871	202.4
Batteries	2719	871	202.4
PCP	1760 [76]	838 [76]	0.5 [76]
	7916 [77]	0.5 [77]	14 [77]
	2719	871	202.4
	1153 [78]	1300 [79]	2.55 [79]
	1153 [78]	1300 [79]	2.55 [79]
PLP	1760 [76]	838 [76]	0.5 [76]
	7916 [77]	0.5 [77]	14 [77]
	1150 [80]	1600 [81]	0.25 [82]
	2719	871	202.4
CHP	2719	871	202.4
	946 [83]	1800 [84]	0.22 [84]
HVP	1150 [80]	1600 [81]	0.25 [82]
	1760 [76]	838 [76]	0.5 [76]
	4000 [85]	386 [85]	398 [85]
	1500 [86]	1200 [86]	0.5 [86]
PDP	1150 [80]	1600 [81]	0.25 [82]
	1150 [80]	1600 [81]	0.25 [82]
Insulation [b]	7.9	1450	0.039
Floorboard [b]	790	1630	2.25

[a] The properties of aluminum are included in the Fluent database

[b] The properties for insulation and floorboard were provided by eCAMION Inc.

3.4 Simulations Performed

Simulations were conducted using steady-state conditions. The steady-state simulations were performed to determine what state the components would be in under normal use. Transient simulations were not used to obtain results due to the large computational load and time requirement, which would exceed several months. Steady state simulations are still proved valuable as they are capable of identifying surface temperatures and allow for ease in altering values to align the surface temperatures with what was reported in measurement data. The steady-state simulations were run using the coupled scheme with pressure, momentum, and energy with the second-order upwind spatial discretization scheme. The turbulent kinetic energy and specific dissipation rate were given first-order upwind schemes.

A total of 7 cases were performed, as listed in Table 8. Case 1 was conducted to identify what would occur in the scenario where the circulation fans and the air conditioner were all deactivated. Case 2 introduced information when the function of all circulation fans was deactivated, but the air conditioner was working. Case 3, outlined in green, represents the existing configuration of the charging system, which implies that the air conditioner and fans were all working. Case 4 was conducted to view the effect of changing the battery fan's blowing direction. Cases 5 and 6 involve changing the location of the air conditioner. Finally, Case 7 examines the changes that occur when the safety barrier is installed with perforations.

Table 8. List of simulations performed organized by case number

Case Number	Air Conditioner	Circulation Fans	Comments
1	✗	✗	Air conditioner and circulation fans deactivated
2	✓	✗	Circulation fans deactivated
3	✓	✓	Existing configuration
4	✓	✓	Battery fan boundary condition change
5	✓	✓	Air conditioning unit placed on the charging system entrance
6	✓	✓	Air conditioning unit placed on the opposite wall
7	✓	✓	Added perforations in the safety barrier

Chapter 4: Results and Discussion

Chapter 4 displays and discusses the results from the simulations performed as mentioned earlier. Among these results, temperature iso-surfaces are examined to view the volume of air within the charging system that is within specified ranges of 25℃ to 40℃, previously stated to be the operating temperature range for lithium-ion batteries. Thereafter, velocity volume renderings are displayed to examine the impact of fans in the charging system and the resulting air movement. The next set of results features an analysis of the surface temperatures for the components, as well as each individual battery from Case 2 to Case 7. The battery analysis also features a Rack Cooling Index (RCI) [66] study as a method of measuring the cooling effectiveness. The final set of results shows the temperature and airflow distributions inside the charging system for Case 3, the existing configuration. The temperature results are shown in terms of contours to provide readers with an easier analysis of the temperature distribution. On the other hand, the airflow or velocity distributions are shown by streamlines. The streamline results show airflow patterns inside the charging system, which provide information on what types of obstacles the airflow encounters and allows for identification of recirculation regions. The airflow is important to promote mixing and to cool components by convection. Together, the temperature contours and streamlines of the airflow provide the ability to assess how changing components positions or altering their geometry can promote airflow to components and affect the temperature distribution. The majority of the data is presented in two-dimensional planes. Therefore, the locations of these planes are indicated so that readers can easily follow them. The following results are obtained from a steady-state analysis of the charging system. A transient analysis requires far too much computational resources.

4.1 Temperature Iso-Surfaces

The temperature iso-surfaces are important in observing regions in the system that are within specified temperature ranges. In this case, the temperature ranges of 25-40℃ and 41℃ and greater are shown. The range of 25-40℃ represents the conditions that are optimal for lithium-ion battery operation [10]. Thus, it is important to examine whether or not the charging system is capable of maintaining that temperature range.

Figure 7 represents the 7 iso-surfaces that were generated within the range of 25-40℃. Observed in Case 1, there is little volume within these conditions. Any simulation after Case 2 displays a considerable increase in the volume of iso-surfaces generated within the charging system. Observing each iso-surface result, Cases 3 to 7 all contain the most volume generated for the specified temperature range of 25-40℃.

Additional iso-surface temperatures produced are shown in Figure 8, which represents the temperature range of 41℃ and greater. Similar to the Figure 7, there is a significant improvement in the overall volume inside of the charging system after Case 2. Case 1 shows that the majority of the charging system is within or above the range mentioned. Case 2 to Case 7 indicate that there is a low volume of high-temperature regions being generated. Additionally, the regions that observe high temperatures are due to the components generating heat that is in contact with the surrounding air. Furthermore, Case 3 to Case 7 show a distinctive improvement over Case 2, where the surrounding regions of the heat-generating components are further decreased. There is no significant decrease in the iso-surfaces from Case 3 to Case 7, where each location specified for the range of 41℃ and greater can be observed to be more or less similar.

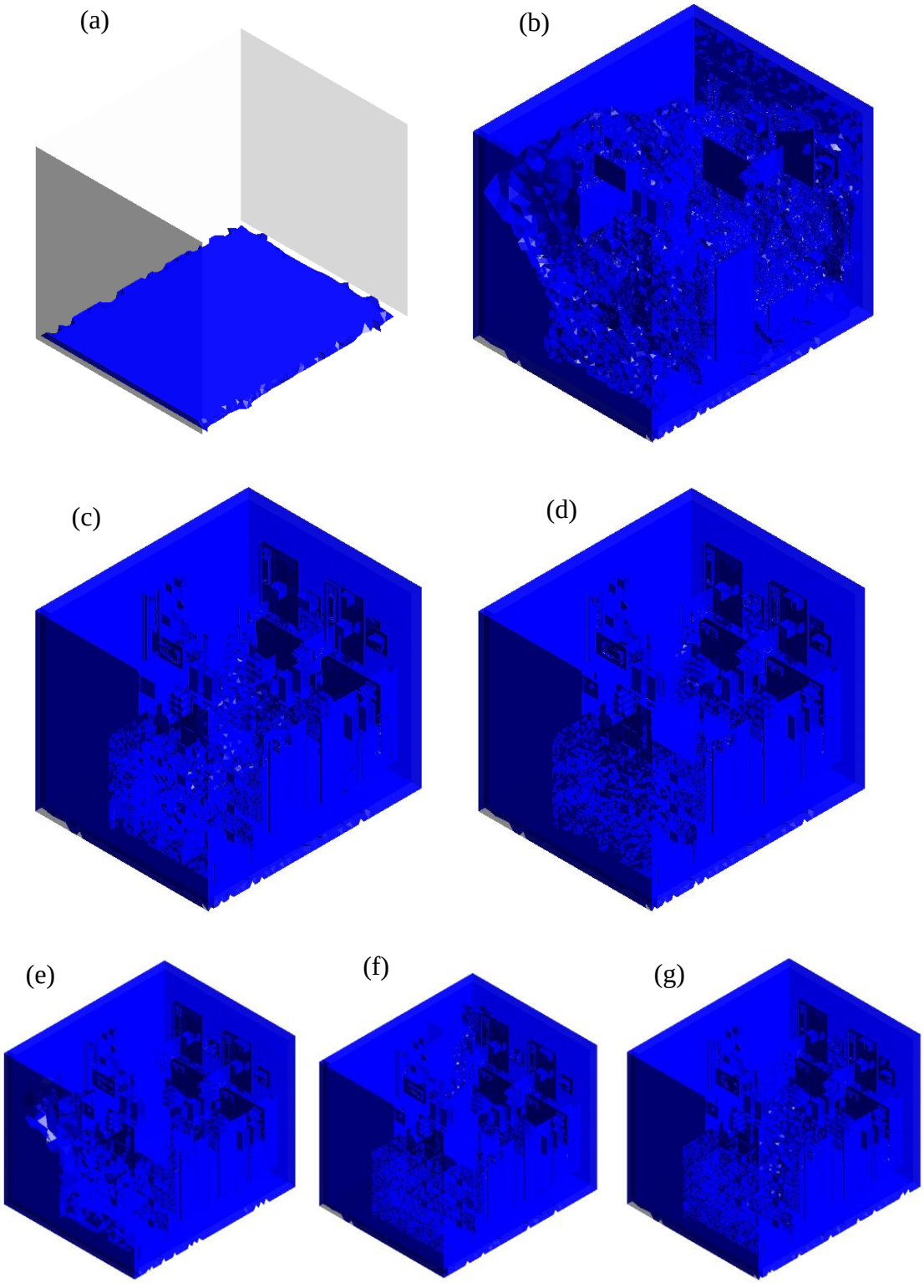

Figure 7. Temperature iso-surfaces for the temperature range of 25-40°C for (a) Case 1, (b) Case 2, (c) Case 3, (d) Case 4, (e) Case 5, (f) Case 6, and (g) Case 7

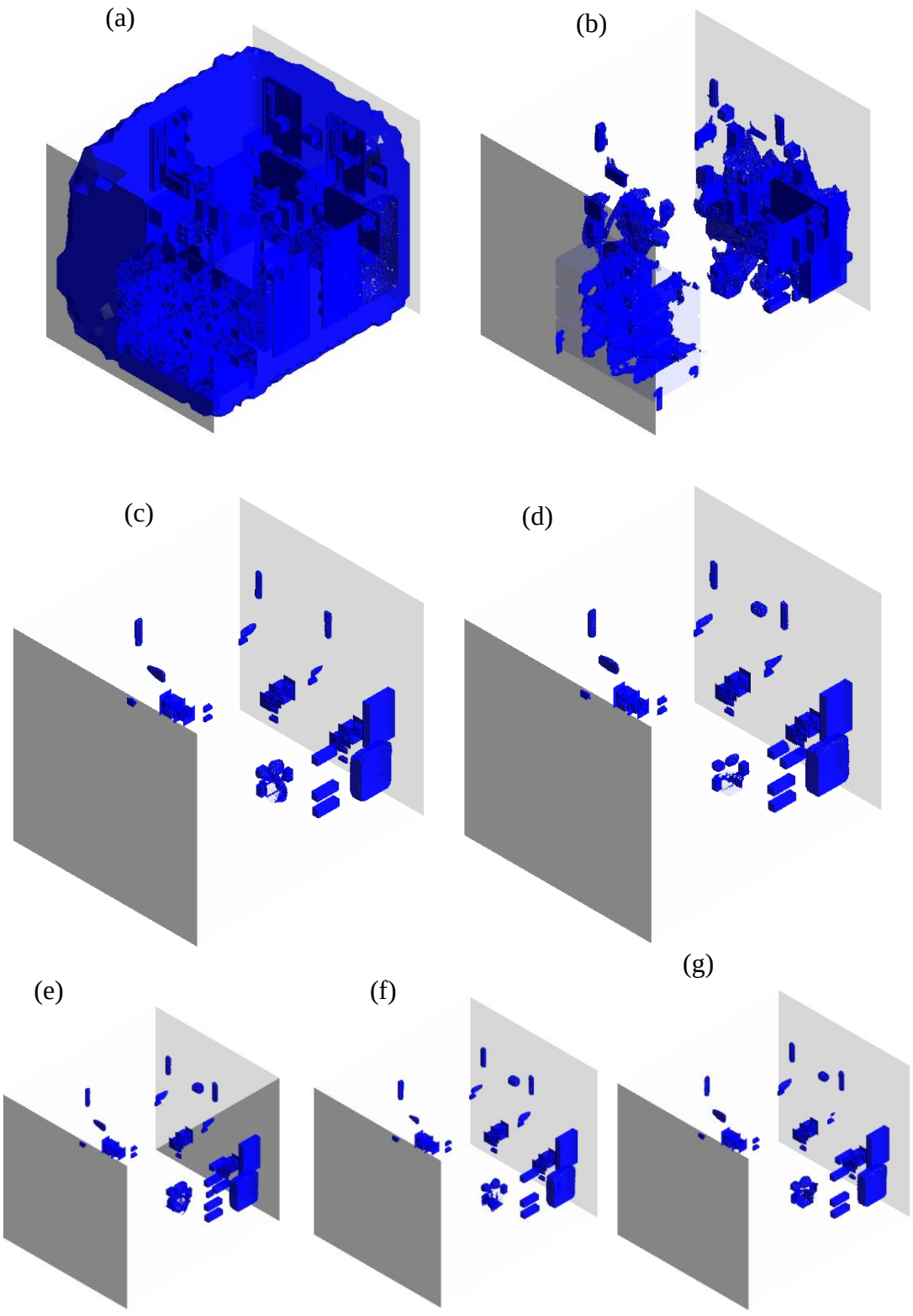

Figure 8. Temperature iso-surfaces for the temperature range of 41°C and greater for (a) Case 1, (b) Case 2, (c) Case 3, (d) Case 4, (e) Case 5, (f) Case 6, and (g) Case 7

4.2 Velocity Volume Rendering

The velocity volume renderings were included in the results to provide a more in-depth view of the circulation fan function in the charging system. In this section, three views are used to display the function of the circulation fans.

Figure 9a features a front view of the charging system, looking into it from the main entrance where the air conditioner (labeled A/C in each figure) can be identified in the top-right. Figure 9b displays a side view of the system. The direction of the battery fans can be observed in the view with the resulting airflow being measured at 6.43 m/s to 12.85 m/s. The blowers can also be identified, along with how their resulting airflow is impacted by the components on the electrical panel positioned above, where the stream can be identified by the 12.85 m/s to 19.28 m/s region.

Figure 10 displays a top view (or plan view) of the system. In this view, the batteries can be identified at the bottom of the figure and the safety barrier in the middle. The velocity volume rendering The battery fans, displayed at the bottom of Figure 10b move the air through the gaps in the battery pack with a velocity of 6.43 m/s to 12.85 m/s (indicated by the legend). The airflow is spread out, which can be observed.

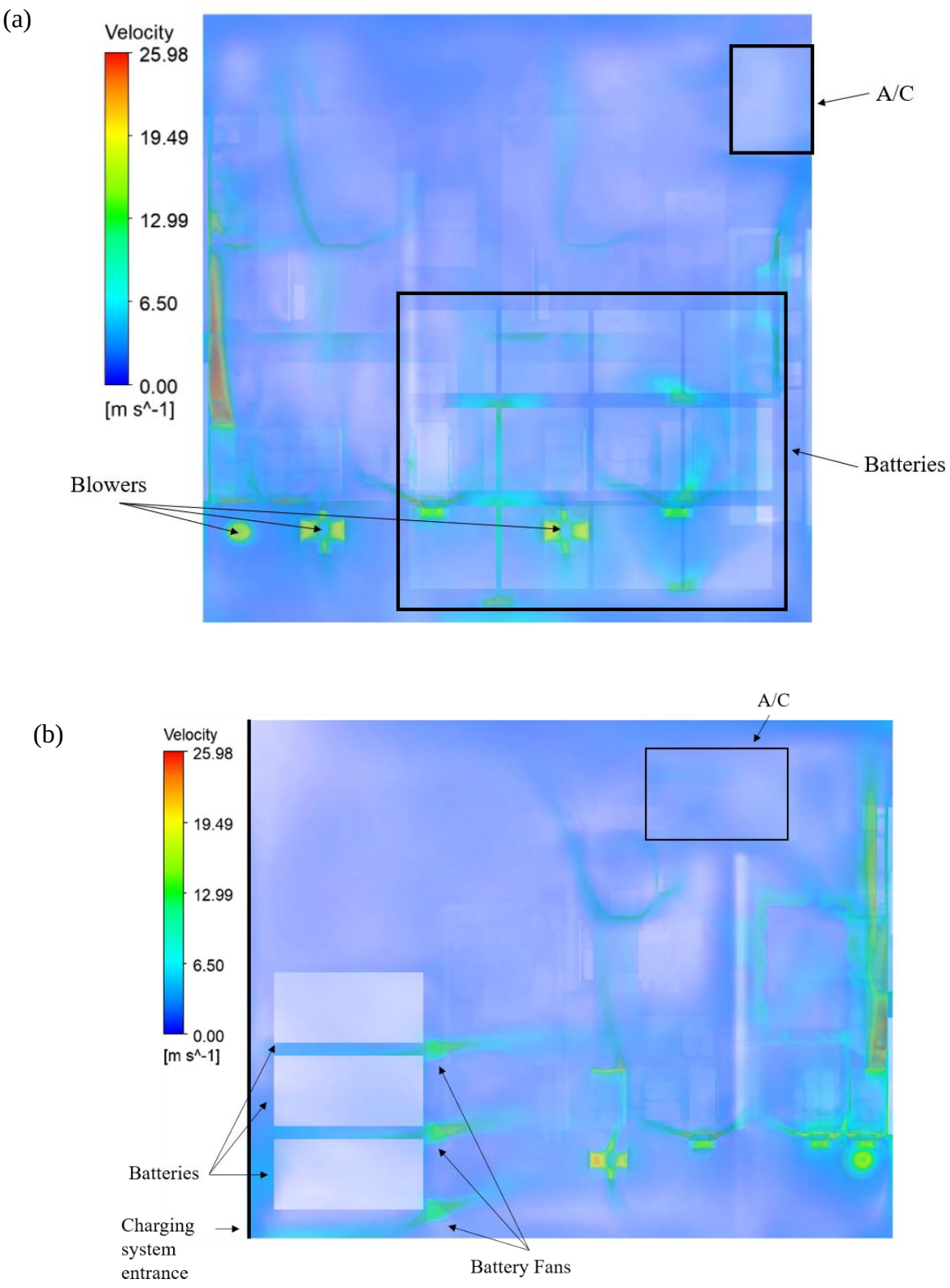

Figure 9. Velocity volume rendering of (a) front view and (b) side view

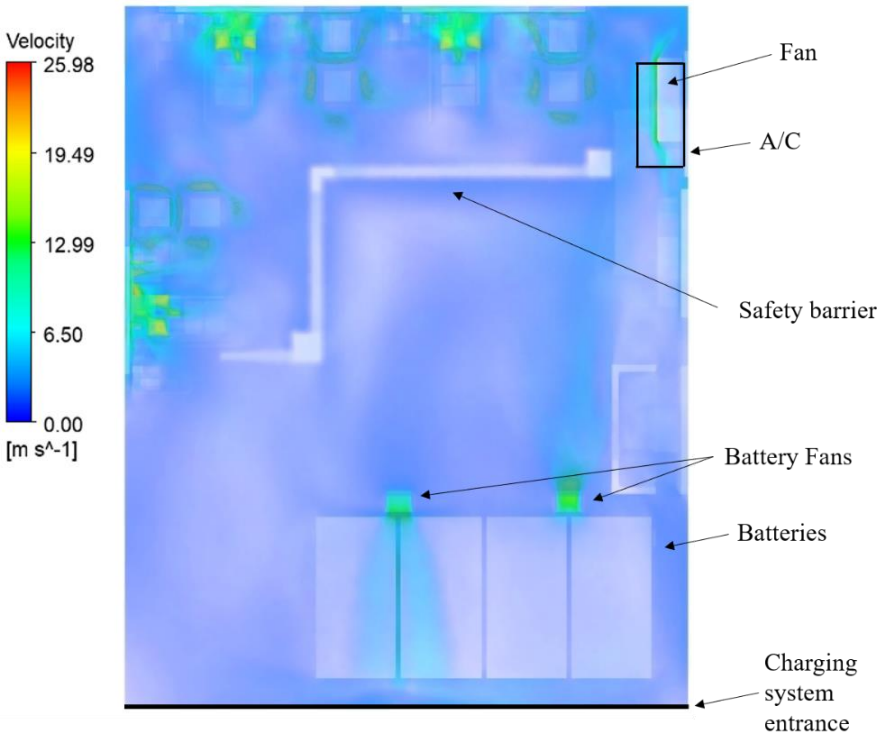

Figure 10. Velocity volume rendering of top view (or plan view)

4.3 Surface Temperatures of Components

The surface temperatures displayed in Figure 11 and Table 9 show the resulting maximum temperatures generated from Case 3. It should be noted that if there were multiples of the same component, the component displaying the highest temperature was chosen. In the case of the batteries, there was a range of surface temperatures generated, which differed with each battery. The resulting surface temperatures for each battery is discussed in Section 4.4. Please note that in this section the component names are changed due to confidentiality.

Figure 11a displays the resulting component surface temperatures from Case 2 to Case 7. The results from Case 2 cause a substantial skew to the graph due to a high temperature,

belonging to component #4, which was measured at 477.46℃. Case 2 was determined not to have the ability to optimally cool the components in the charging system. Figure 11a shows that the resulting temperatures from Case 2 is more than double that of any of other cases displayed. Figure 11b displays a more detailed view of Case 3 to Case 7 with the heavily skewed results removed. Component #13 resulted in the highest surface temperatures, which was found to be between 82.22℃ to 106.57℃, with Case 5 having the lowest temperature. Between each of the cases, the surface temperatures were found to be in the same range, however there were cases where the cooling was found to be less optimal. For example, this can be seen in component #6, measured from ranges 64.92℃ to 75.52℃, where Case 3 and Case 7 both exhibit a difference in temperature by approximately 10℃ for the same component.

Table 9 provides information on each configuration from Case 2 to Case 7. The lowest temperature for each component is marked in green to indicate the case that was able to cool it most effectively. The results from Case 2 show that the battery surface temperatures greatly exceed their operating limits at 68.28℃. Adding the various circulation fans improves the surface temperatures of all components, as shown in Case 3. From Case 4 to Case 7, modifications to the charging system were made, previously discussed in Table 7. Each configuration resulted in lower surface temperatures for different components. For example, in Case 5 where the air conditioner was placed on the entrance side of the system, the resulting temperature for component #5 resulted in a temperature of 64.92℃ versus in Case 3 where the compared temperature increased to 75.52℃. Case 3, however, has a maximum temperature of 37.49℃ for component #3 versus the maximum temperature of

36.67℃ in Case 5. This observation illustrates the effectiveness of some configurations to target the cooling of selected components of interest.

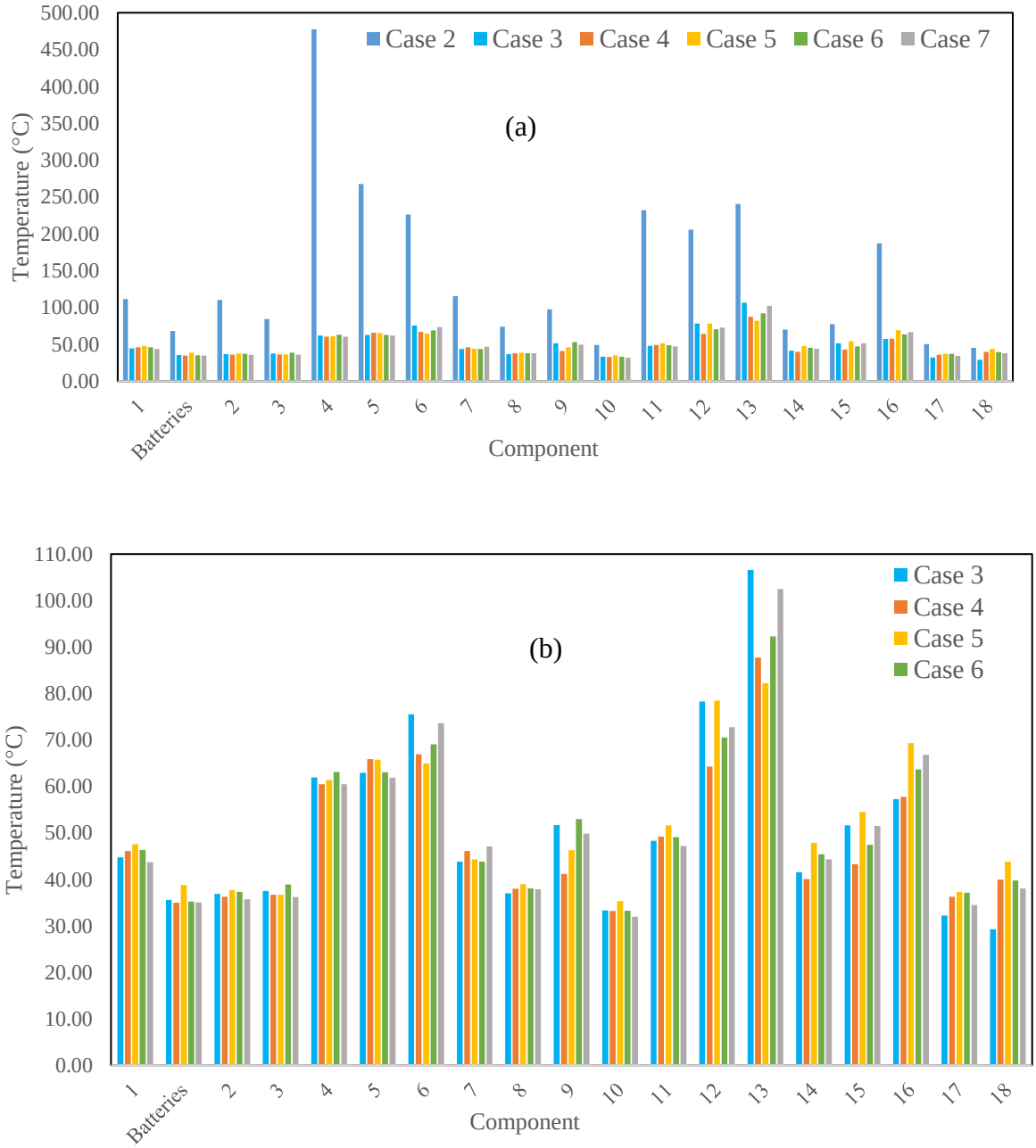

Figure 11. Component surface temperatures of (a) Case 2 through Case 7, and (b) a more detailed view of Case 3 through Case 7. Note that component names are not shown due to confidentiality.

Table 9. Maximum surface temperatures organized by panel and component. Note that component names are not shown due to confidentiality.

Assembly	Component	Resulting Max Surface Temperature (°C)					
		Case 2	Case 3	Case 4	Case 5	Case 6	Case 7
PLC	1	111.49	44.72	46.10	47.56	46.31	43.69
Batteries		68.28	35.61	34.99	38.76	35.24	35.01
PCP	2	110.33	36.89	36.28	37.66	37.32	35.73
	3	84.71	37.49	36.71	36.67	38.93	36.22
	4	477.46	61.93	60.49	61.39	63.09	60.48
	5	267.74	62.89	65.89	65.72	63.03	61.88
	6	226.41	75.52	66.94	64.92	69.06	73.58
PLP	7	115.58	43.79	46.10	44.32	43.79	47.06
	8	73.98	36.99	37.96	38.95	38.03	37.88
	9	97.87	51.69	41.15	46.25	52.97	49.84
	10	49.25	33.32	33.19	35.35	33.25	31.98
CHP	11	231.92	48.29	49.22	51.62	49.07	47.22
	12	205.84	78.26	64.29	78.46	70.51	72.76
HVP	13	240.67	106.57	87.73	82.22	92.30	102.50
	14	70.25	41.53	40.09	47.86	45.41	44.28
	15	77.59	51.63	43.27	54.48	47.42	51.49
	16	187.04	57.25	57.76	69.29	63.63	66.81
PDP	17	50.29	32.18	36.27	37.28	37.13	34.50
	18	45.52	29.27	39.96	43.80	39.76	38.01
Total[a]		0	5	5	2	0	7

[a]Total number of components with the lowest recorded temperature

4.4 Battery Surface Temperature Analysis

It is important to categorize each battery because the surface temperature for each individual battery differs. Each battery undergoes an individual analysis to obtain its resulting surface temperature. Figure 12 shows the categorization of the batteries present in the charging system.

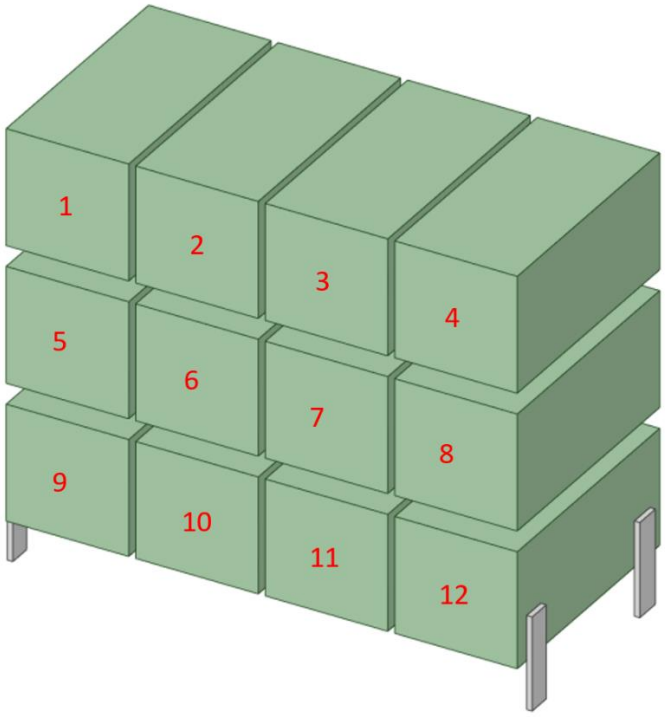

Figure 12. Individual battery number assignments

To determine the effectiveness of each cooling configuration from Case 2 to Case 7, the RCI method [66] was implemented, where the surface temperatures were recorded and used as input for the calculations with each battery's upper operating temperature limit in mind. The resulting value indicates the effectiveness of the air conditioner and fans. Based on Equation 1, if the RCI value is 100% or greater, it indicates that the system's cooling is very effective.

Herrlin [66] also states in the case of data center analysis, an RCI of 95% is a satisfactory system design, this was adopted for the analysis of battery RCI values as well. The maximum battery operating temperature is listed as 40℃ [10]. The resulting battery surface temperatures for each category are summarized in Table 10. The values were used to calculate the RCI for batteries, shown in Table 11.

Figure 13a and Figure 14 display the battery surface temperatures and RCI results from Case 2 to Case 7. Similar to Figure 11a, Case 2 results cause a skew in the results. It can be clearly observed that Case 2 has the highest battery surface temperatures by a wide margin. Figure 13b displays a more detailed view of Case 3 to Case 7 with the skewed results from Case 2 removed. It is observed that Case 5 often results in the highest battery surface temperatures when neglecting Case 2. Case 6 often registers high battery surface temperatures in comparison to the other cases as well. Case 3 and Case 4 results indicate that the temperatures in those simulations are among the lowest.

The lowest RCI recorded in Case 2 was 29.29% while in Case 3, the highest RCI was found to be 124.09%, as seen in Figure 14 and Table 11. This indicates that the design is able to retain the optimal battery operating range by adding circulation fans. It should be emphasized that the higher the RCI value, the better the cooling ability. Table 10 and Table 11 are marked with green cells that indicate the lowest resulting battery surface temperature in all the cases.

The results show that Case 3 was able to effectively cool all batteries with the highest temperature being 35.61℃ (RCI of 110.98%) and the lowest at 30.36℃ (RCI of 124.09%). The next highest temperature found in Case 3 was 34.84℃ (RCI of 123.85%). Case 4, Case 6, and Case 7 results show an improvement in the maximum temperature generated in the

batteries with a temperature of 34.99℃ (RCI of 112.52%), 35.24℃ (RCI of 111.91%), and 35.01℃ (RCI of 112.47%), respectively.

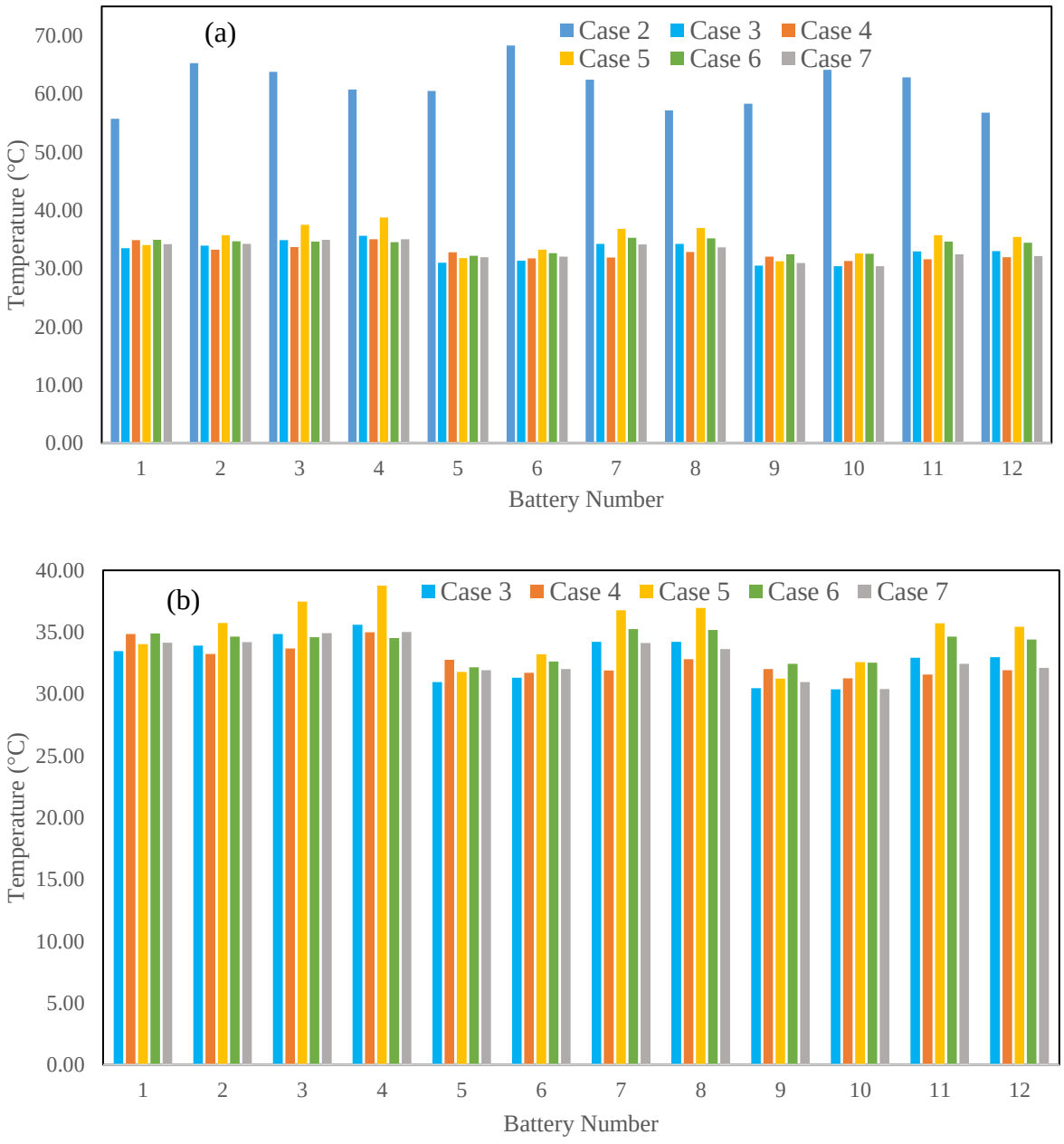

Figure 13. Battery surface temperatures of (a) Case 2 through Case 7, and (b) a more detailed view of Case 3 through Case 7

Table 10. Individual battery surface temperatures by case

Battery Number	Resulting Surface Temperature (℃)					
	Case 2	Case 3	Case 4	Case 5	Case 6	Case 7
1	55.69	33.46	34.84	34.02	34.91	34.15
2	65.27	33.91	33.23	35.73	34.64	34.20
3	63.76	34.84	33.68	37.48	34.59	34.93
4	60.72	35.61	34.99	38.76	34.53	35.01
5	60.47	30.96	32.77	31.77	32.16	31.93
6	68.28	31.32	31.70	33.21	32.63	32.01
7	62.44	34.23	31.89	36.78	35.24	34.13
8	57.15	34.23	32.80	36.96	35.18	33.63
9	58.31	30.46	32.02	31.24	32.44	30.96
10	64.12	30.36	31.26	32.58	32.52	30.39
11	62.82	32.92	31.58	35.72	34.63	32.43
12	56.74	32.97	31.91	35.43	34.40	32.11
Total[a]	0	5	6	0	1	0

[a]Total number of batteries with the lowest recorded temperature

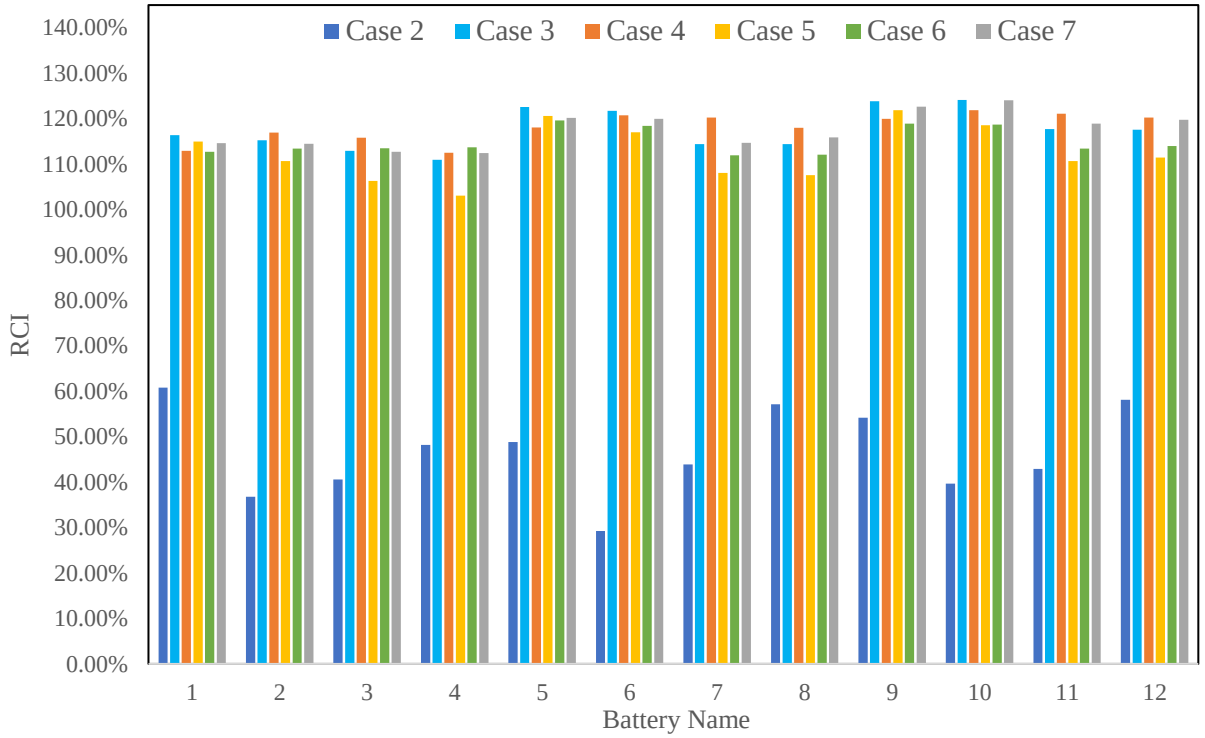

Figure 14. Resulting RCI values of Case 2 through Case 7

Table 11. RCI results organized by case

Battery Number	RCI					
	Case 2	Case 3	Case 4	Case 5	Case 6	Case 7
1	60.78%	116.36%	112.90%	114.95%	112.74%	114.62%
2	36.82%	115.24%	116.94%	110.68%	113.40%	114.50%
3	40.59%	112.89%	115.81%	106.30%	113.52%	112.69%
4	48.20%	110.98%	112.52%	103.10%	113.69%	112.47%
5	48.83%	122.60%	118.07%	120.58%	119.59%	120.19%
6	29.29%	121.71%	120.74%	116.98%	118.42%	119.98%
7	43.89%	114.44%	120.27%	108.05%	111.91%	114.68%
8	57.12%	114.44%	118.00%	107.60%	112.06%	115.92%
9	54.22%	123.85%	119.96%	121.90%	118.90%	122.61%
10	39.70%	124.09%	121.85%	118.55%	118.70%	124.04%
11	42.94%	117.70%	121.06%	110.70%	113.43%	118.94%
12	58.14%	117.57%	120.22%	111.43%	114.01%	119.73%

4.5 Component and Battery Improvement Assessment

Each battery and component from Sections 4.4 and 4.5 were analyzed against Case 2 (baseline) to illustrate the improvement in surface temperatures achieved by the incorporation of the fans and blowers. It should be noted that Case 3 to Case 7 have the air conditioner and circulation fans activated, while Case 2 only has the air conditioner. Please note that in this section the component names are changed due to confidentiality.

From Figure 15a, which presents the findings from the component surface temperatures in Table 9, it can be observed that all components experience improvements over the baseline case, Case 2. There were some cases where the improvements remained the same in all the cases performed, such as in component #4. However, some components experienced a significant improvement in comparison to the other cases. For example, component #18 showed a significant improvement of 34.70% for Case 3 compared to the next highest improvement of 16.49% for Case 7.

From Figure 15b, which presents the findings from the battery surface temperature listed in Table 10, it can be observed that each battery tremendously improved in surface temperature in comparison to Case 2 (baseline case). For example, 35.33% is the lowest improvement. These findings show that the battery surface temperatures are significantly impacted by the presence of the circulation fans inside of the charging system.

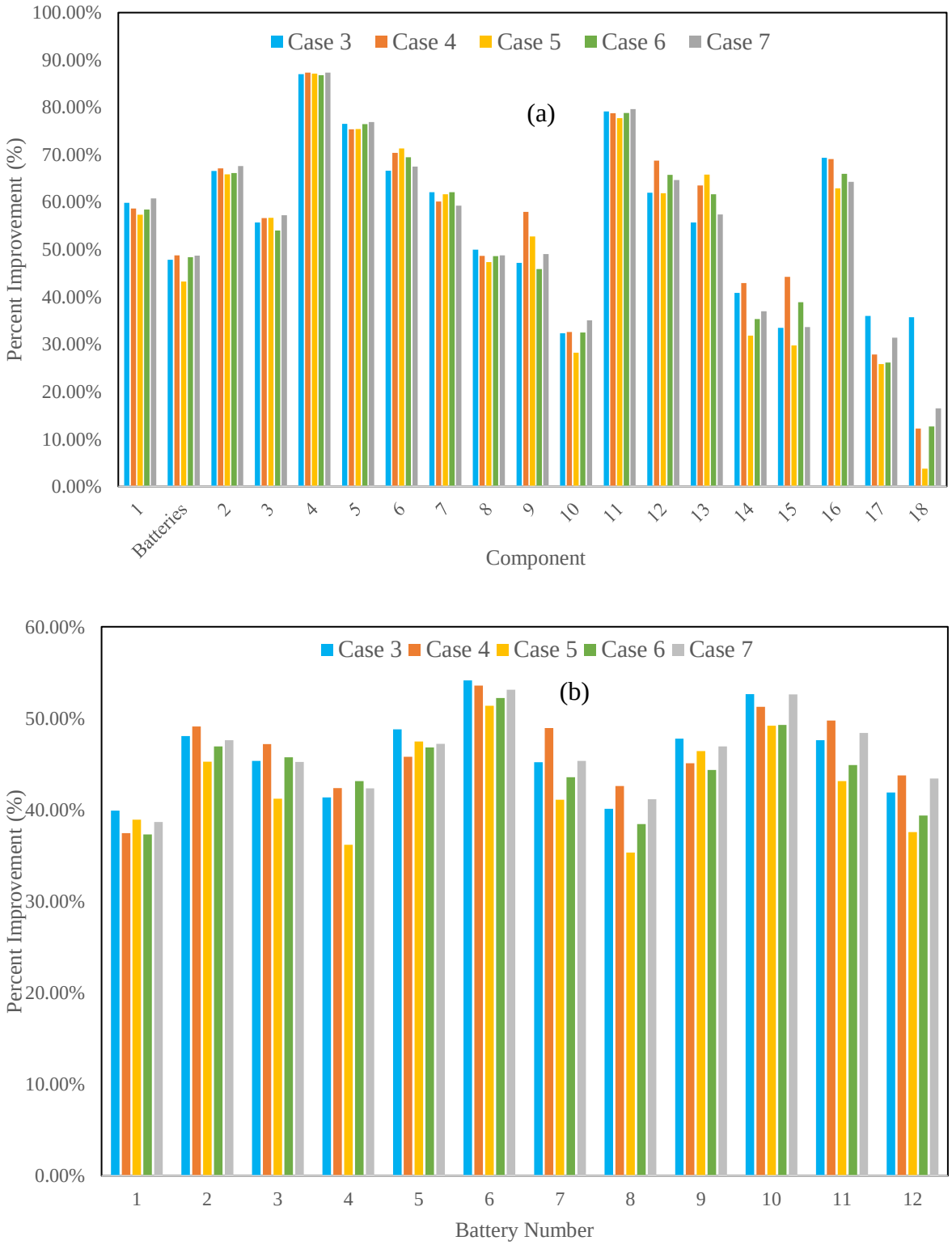

Figure 15. Percentage improvement for (a) components, and (b) batteries. Note that component names are not shown due to confidentiality.

4.6 Planes of Interest

This section describes the planes generated and their respective co-ordinates. Figure 16 provides a view of the co-ordinate system used in ANSYS Fluent.

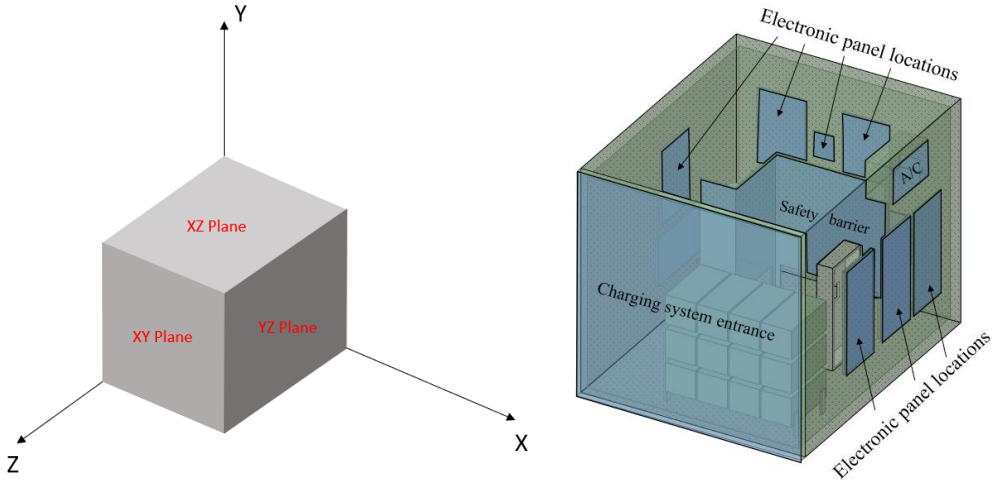

Figure 16. Co-ordinate system used and the three planes: XY, XZ, and YZ and how it corresponds to the locations matching the charging system. Note that the electronic components in the unit are hidden for confidentiality.

4.7 Temperature Contours

The temperature contours are displayed in planes generated following the co-ordinate system in Figure 16.

Table 12 lists the names of the temperature contours, as well as their corresponding plane names and numbers. It should be noted that each temperature contour is generated for a local temperature range. This causes the legend shown to heavily skew towards the highest temperature and lowest temperature in the contour plane. It is recommended to view the legend for each temperature contour plane as each contour will have different ranges.

The temperature contours from Figure 17 to Figure 26 show various views of the thermal profile inside the charging system. The analysis will be split into the 3 plane views that

were generated and discussed. The analysis begins in the XY plane view, then the YZ plane view, and finally, the XZ plane view.

Table 12. Temperature contours generated with corresponding planes

Plane Location	Plane Number	Plane
Plane-z0.35	1	XY Plane
Plane-z0.85	2	
Plane-z1.05	3	
Plane-z1.25	4	
Plane-z1.65	5	
Plane-z2.15	6	
Plane-x-1.3	7	YZ Plane
Plane-x-0.5	8	
Plane-x-0.1	9	
Plane-x0.4	10	
Plane-y0.15	11	XZ Plane
Plane-y0.55	12	
Plane-y0.65	13	

4.7.1 Temperature contours in the XY plane

It was determined that 6 planes in the XY Plane were necessary to analyze the thermal profiles inside the charging system. Figure 17 identifies those six planes, as shown.

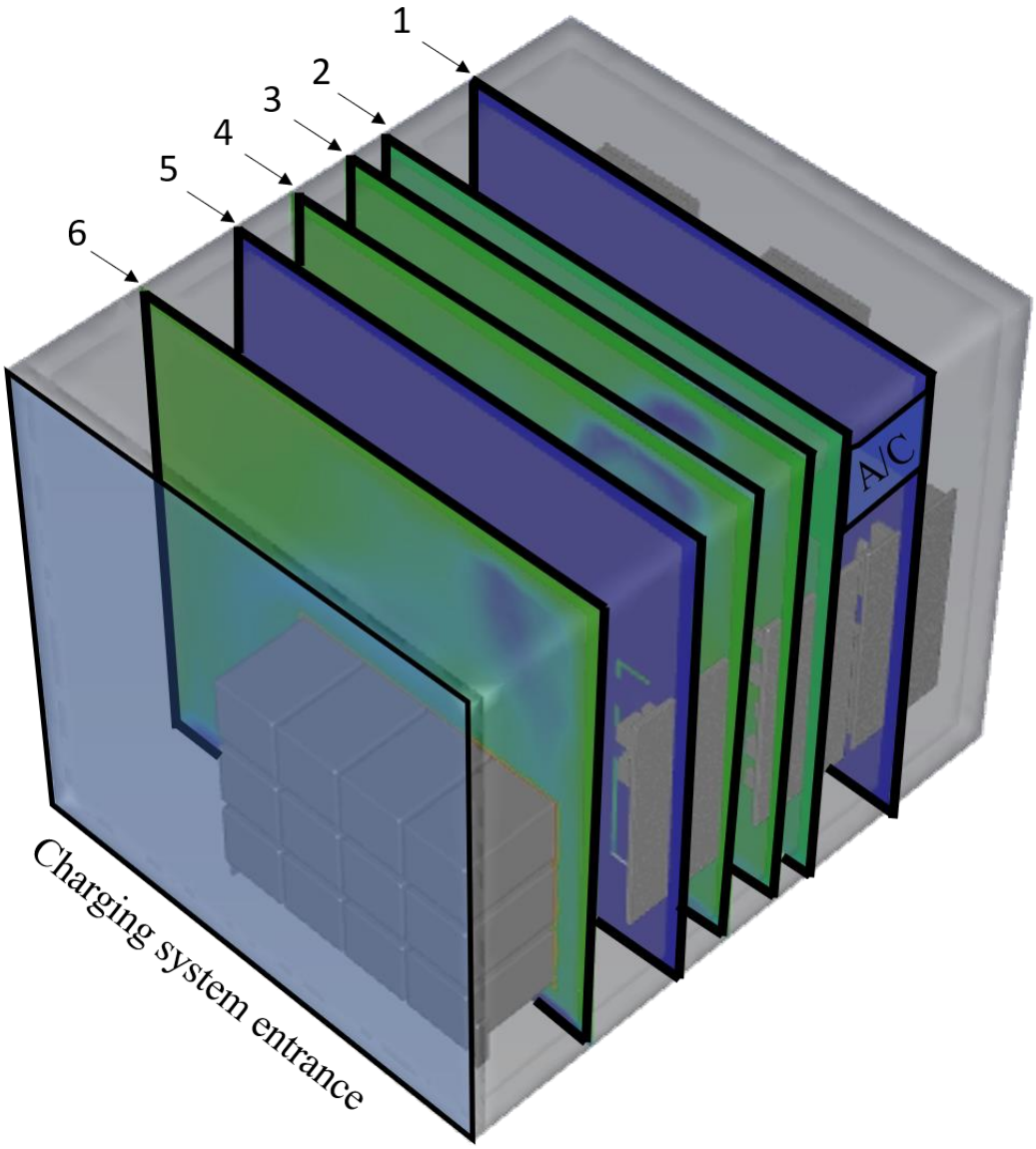

Figure 17. Planes (numbered from 1 to 6) used to display the temperature contours in the XY plane

Figure 18a displays the contours in Plane 1, which show that the temperature everywhere is less than 41.42℃, except in the two regions on the right side of the figure. The hottest region contains a component in the charging system (component #12 from Table 9). It shows that the temperature decreases from 189.24℃ at the core to 78.26℃ at its surface. The high core temperature is expected because the convective cooling does not have any effect inside the component. The surface temperature is also quite high compared to other surfaces due to the high core temperature.

Figure 18b, representing the contours of Plane 2, displays a high-temperature region (i.e., a temperature of 64.50℃.) representing another component within the charging system (component #4 in Table 9). However, a low-temperature region of 4.08℃ to 16.16℃ can be identified at the top-right of the figure. This low-temperature region is linked to the presence of the inlet air from the air conditioner as well as the air movement from the circulation fans. The velocity streamline results in Section 4.8 will aid in understanding the movement of the supply air pattern from the air conditioner.

Figure 19a represents the contours of Plane 3 and features another low-temperature region with temperature ranging from 15.32℃ to 21.21℃. Again, this low-temperature region is related to the cold air supply from the air conditioner. On the right side of this figure, it can be seen that the there is a panel of components (representing component #1) resulting in temperatures ranging from approximately 35.92℃ to 44.76℃, while the surrounding air temperature is between 24.15℃ and 32.98℃.

Figure 19b displays the contours of Plane 4 and shows a few patterns consistent with those in Figure 19b. In addition to this, Figure 20a displays a high-temperature region on the left

that ranges from 34.51℃ to 37.76℃, representing component #3 (in Table 9) of the charging system. Additionally, the middle of the figure shows a low-temperature region ranging from 21.50℃ to 26.38℃, which represents the movement of the cold airflow generated by the air conditioner as it travels away from the air conditioner inlet (shown in Figure 17).

Figure 20a contains the contours for Plane 5. In Figure 20a, the resulting temperature contour represents a majority of the temperature ranging from 23.23℃ to 37.99℃. This solid blue colour is due to the high temperatures generated which can be observed at the right side of the figure, where the highest temperature is 170.91℃ at the core of component #13 (in Table 9). The resulting surface temperature results in 107.57℃. This high temperature on the legend has skewed the colour assignments.

Figure 20b, representing the contour of Plane 6 shows a view of the battery packs, as identified by the high-temperature regions ranging from 32.41℃ to 35.58℃. The surrounding temperature was identified to be between 27.12℃ and 31.35℃ indicated by the blue and green coloured regions. In the figure, the bottom left quadrant of the high-temperature zone ranges from 29.23℃ to 31.35℃, while the other regions of the high-temperature zone, display a temperature of 32.41℃ or greater. This difference in temperature is due to the configuration of the battery fans and the direction in which they are blowing air. At the bottom left quadrant, the fans blow air to the batteries, but at the bottom right quadrant, they blow air away from the batteries. In addition, the top row of batteries experiences less cooling due to the placement of the fans being closer to the bottoms of the battery pack. The configuration of the fans is shown in Figure 9.

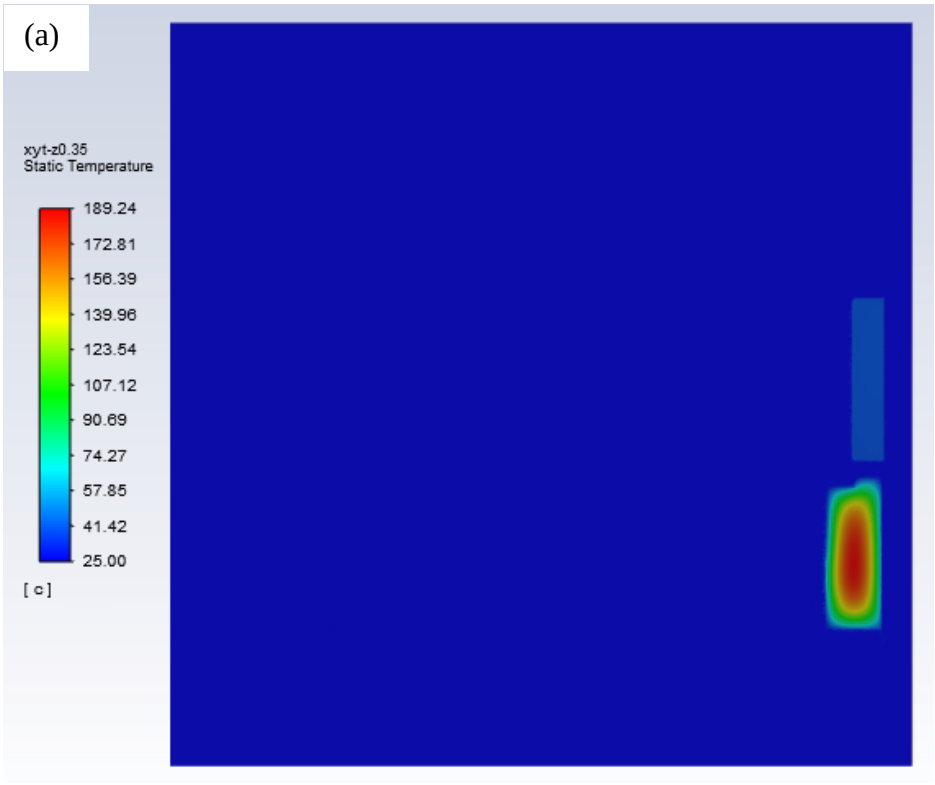

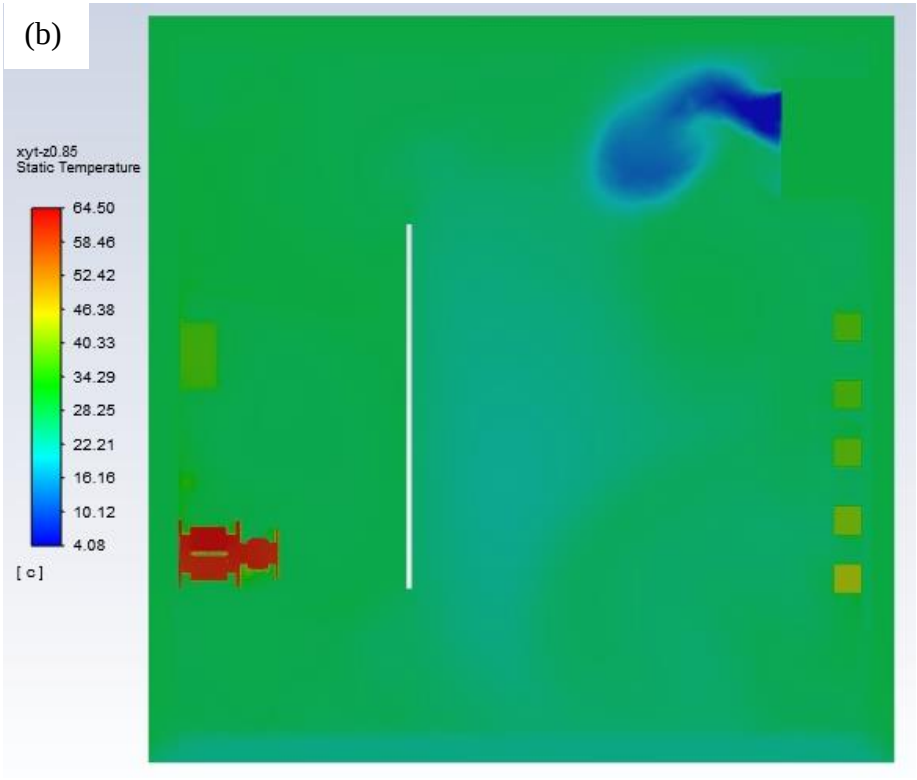

Figure 18. Temperature contours in (a) Plane 1 and (b) Plane 2

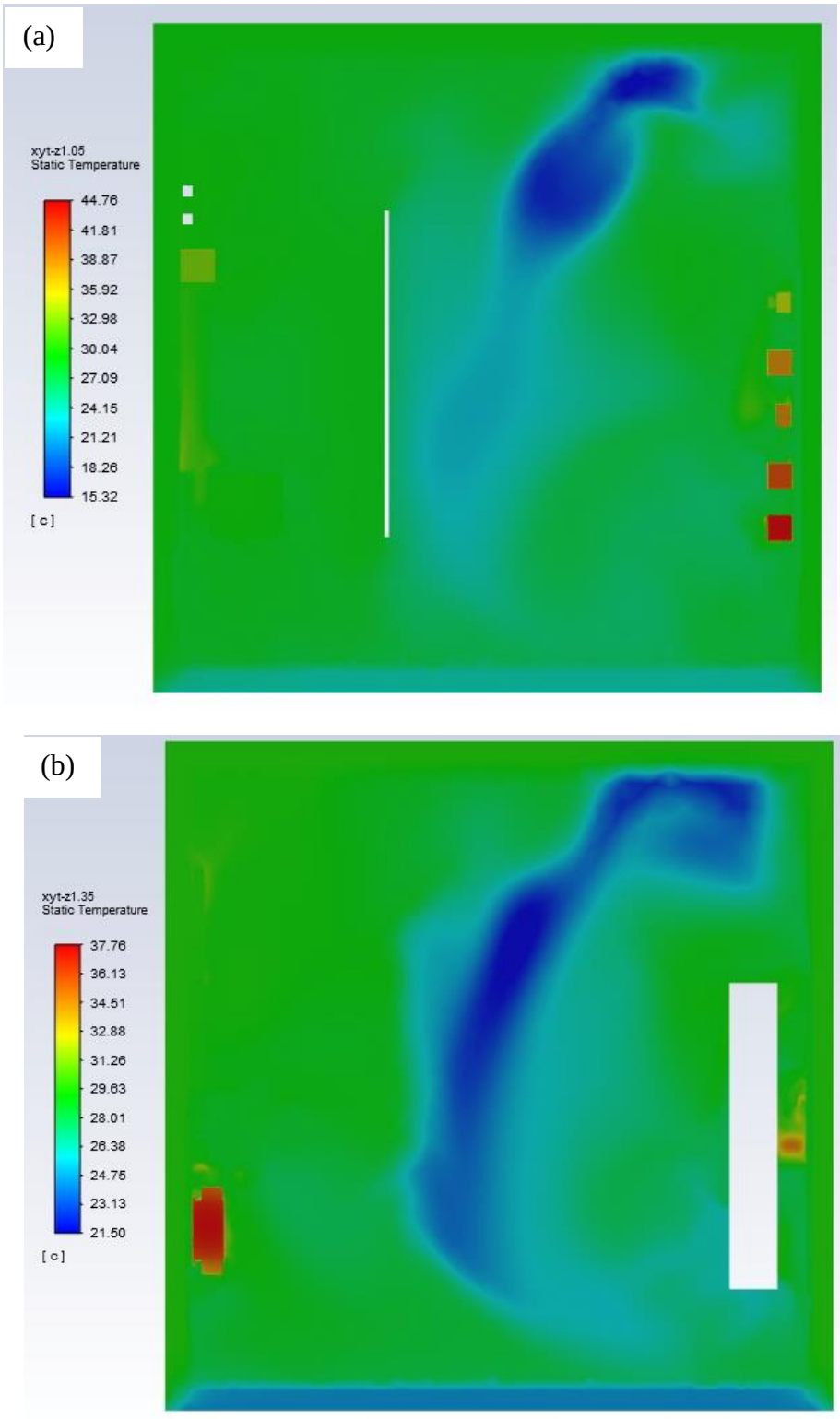

Figure 19. Temperature contours in (a) Plane 3 and (b) Plane 4

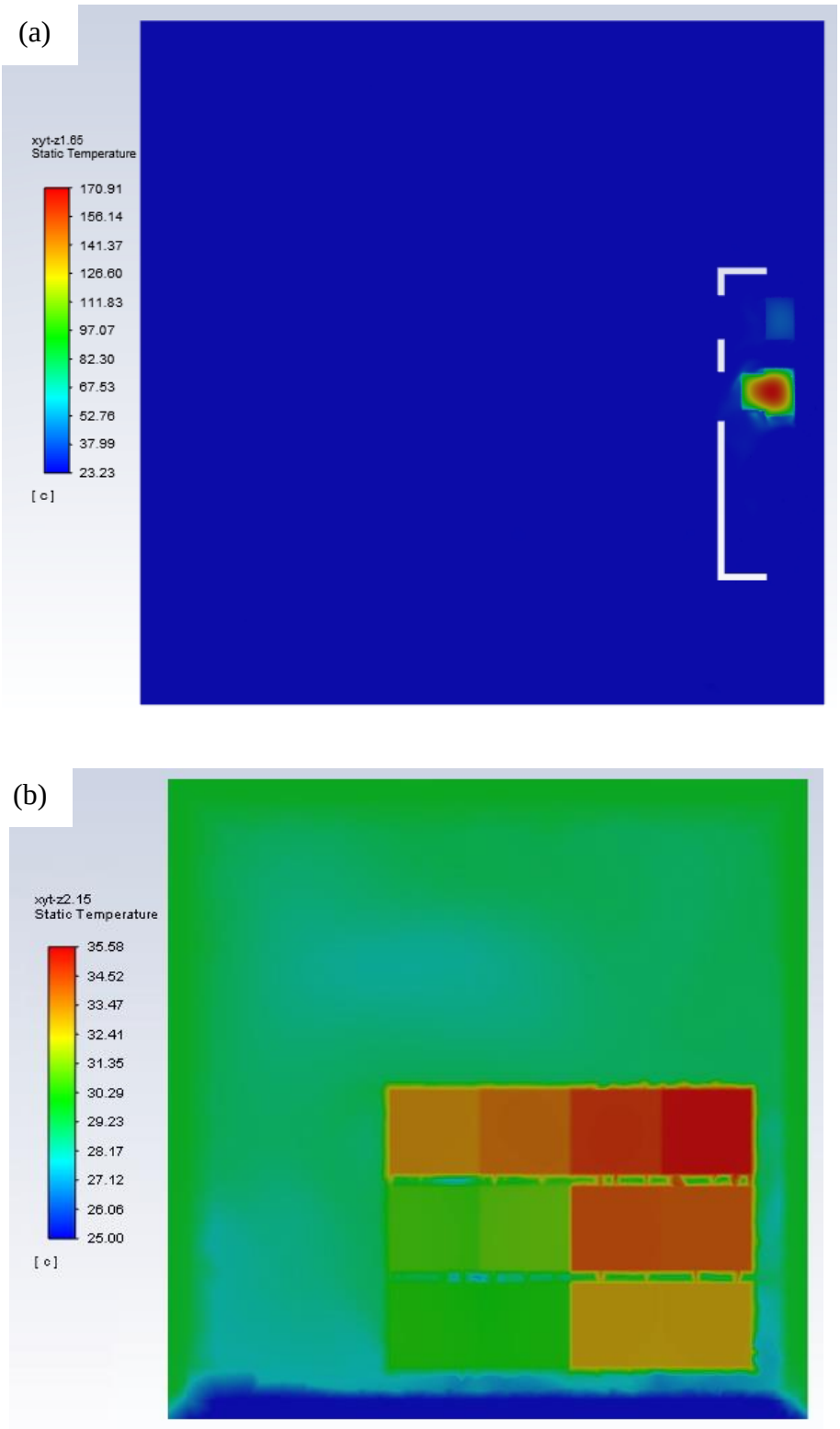

Figure 20. Temperature contours in (a) Plane 5 and (b) Plane 6

4.7.2 Temperature contours in the YZ plane

In this section, the temperature contours in the YZ plane are reported. It was determined that 4 planes were necessary to illustrate the temperature distribution and thermal profile. Figure 21 identifies the 4 planes as shown below.

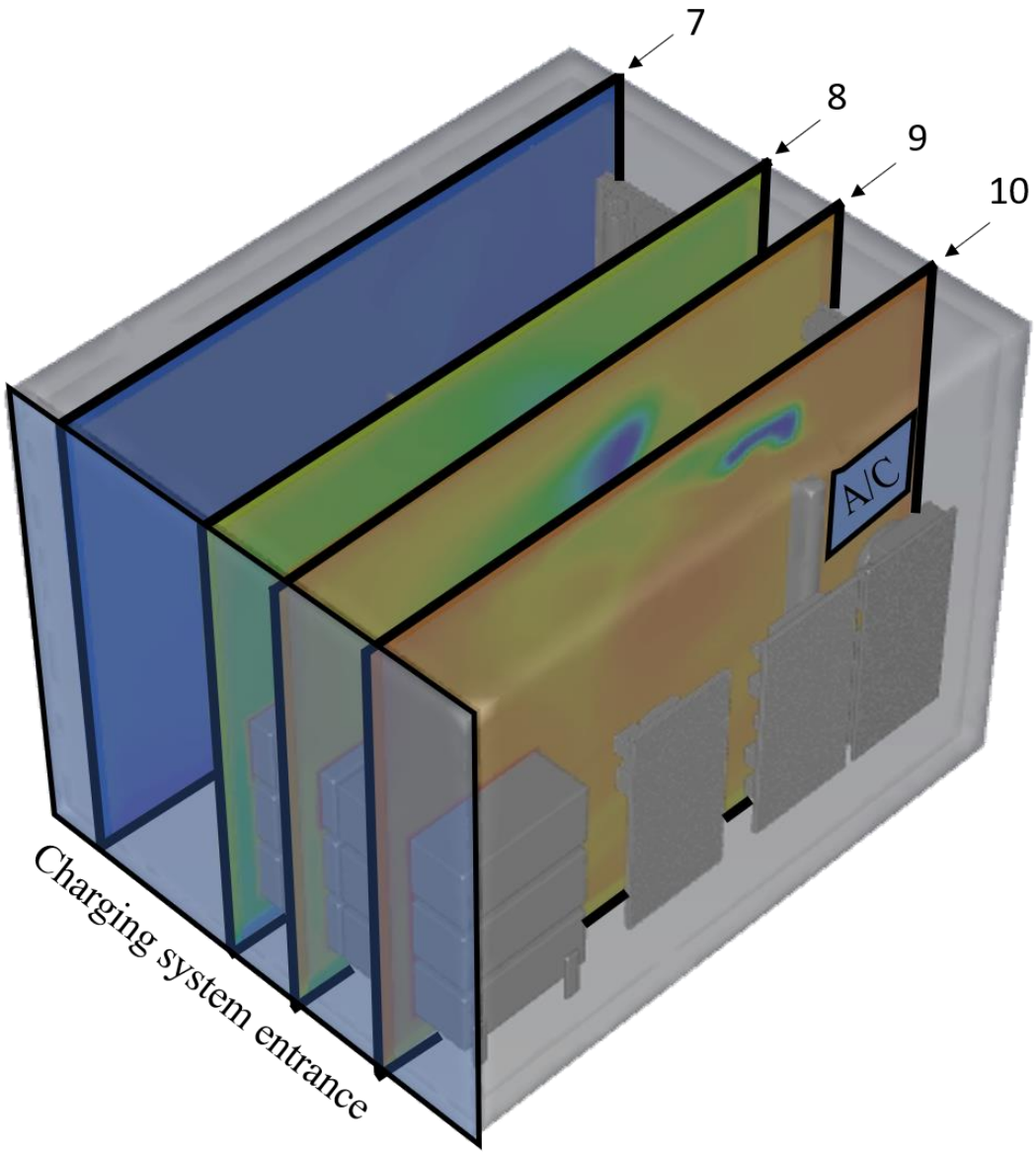

Figure 21. Planes (numbered from 7 to 10) used to display the temperature contours in the YZ plane

Figure 22a displays the contours for Plane 7, with the majority of the temperature contours showing the temperature ranging from 25℃ to 32.65℃, indicated by the blue colour. The high-temperature regions displayed approximately in the middle of the figure shows temperatures ranging from 47.96℃ to 63.26℃, which represent several components used in the charging system (components #3, #4, #7, and #8 in Table 9) . The components show temperature ranges on a single panel ranging from 40.30℃ to 47.96℃ and temperatures ranging from 32.65℃ to 36.48℃. Two of the listed components are identified with temperatures ranging from 60.35℃ to 75.51℃ and from 55.51℃ to 63.26℃ represent the remaining two components listed previously on a different electrical panel in the charging system. In Figure 22a, it can be seen that there is a region with a temperature of 32.65℃ surrounding component #4 with the temperature range of 60.35℃ to 75.51℃, partly due to the presence of the fans and blower.

Figure 22b, contains the contours of Plane 8, with a high-temperature region ranging from 30.95℃ to 33.50℃ in the bottom-middle of the figure which represents a portion of the battery packs. It is important to note that this figure represents the temperature contours for 3 battery packs out of the 12 shown in Figure 12. A large cold air region can be observed in the middle of the figure, where the low temperatures range from 23.41℃ to 25.43℃. This can be explained by the movement of the cold airflow entering the charging system from the air conditioner and its behaviour due to the fans, which will be further explained by the streamlines.

Figure 23a, displaying Plane 9, shows three main temperature regions: a low-temperature region from 16.85℃ to 20.28℃, a medium-temperature region from 23.70℃ to 27.13℃, and a high-temperature region from 30.55℃ to 33.97℃. The lowest temperature region can

be identified to be close to the center of the figure. This is due to the placement of the battery fans, which are located at the left of the figure. Based on Figure 19, the contour is generated at the location where the fans function to draw air in between the batteries, which can explain the behaviour of the medium temperature region moving towards the high-temperature regions, which can be identified to be the battery packs, as discussed in Figure 21a.

Figure 23b, displaying Plane 10 features a view of a different portion of the battery packs, which can be identified in Figure 21. The portion displayed features the fans blowing air away from the battery packs, which can be followed by viewing the bottom yellow region of temperatures 25.18℃ to 28.18℃ being blown towards the white region representing the safety barrier. This can explain the movement of cold air, identified to be the region of 4.14℃ to 19.17℃, where it is observed to be moving towards the left side of the figure. This is further examined in the discussion of the velocity streamline results and further explains the trends seen in Figure 32 to Figure 34.

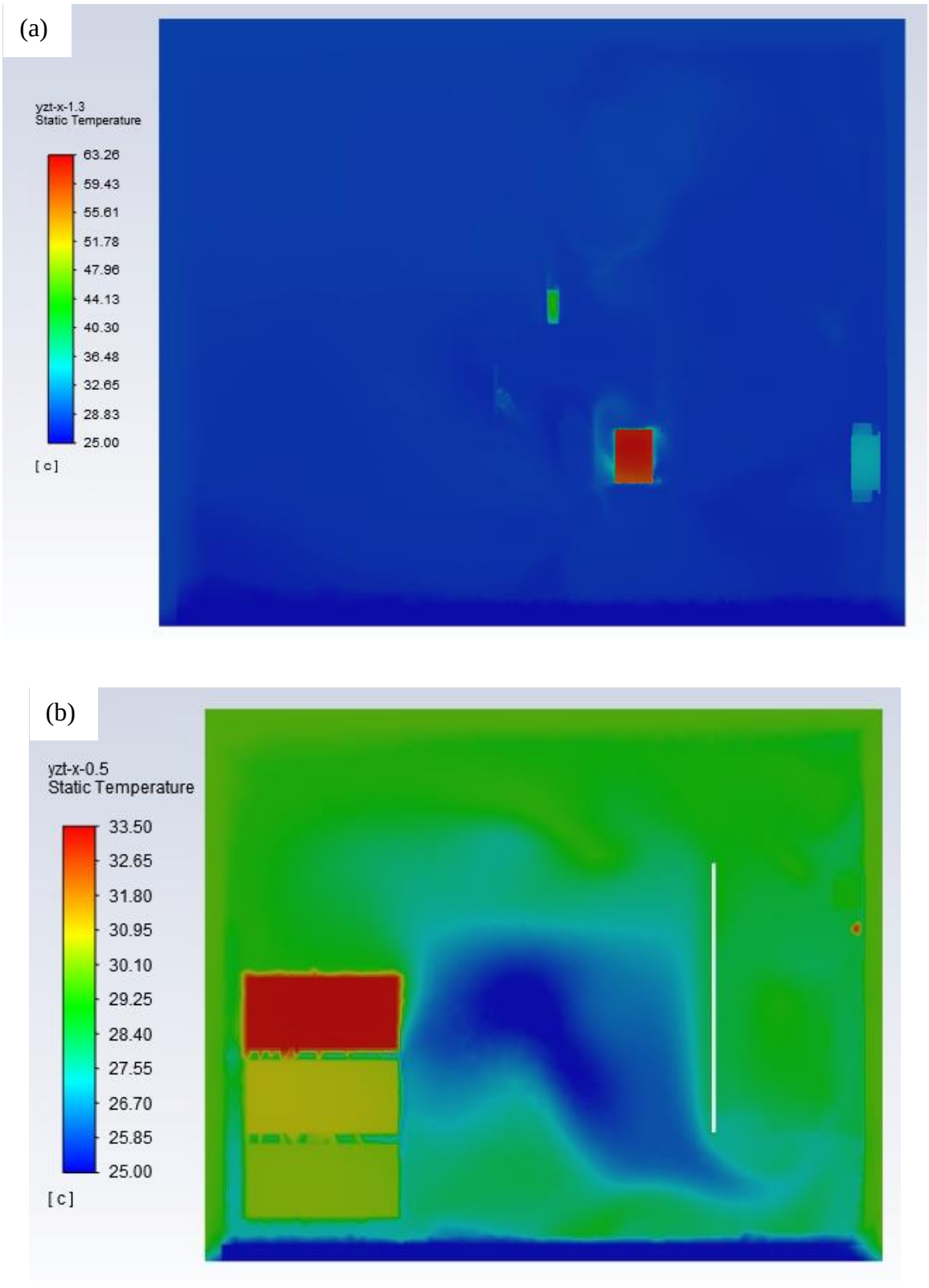

Figure 22. Temperature contours in (a) Plane 7 and (b) Plane 8

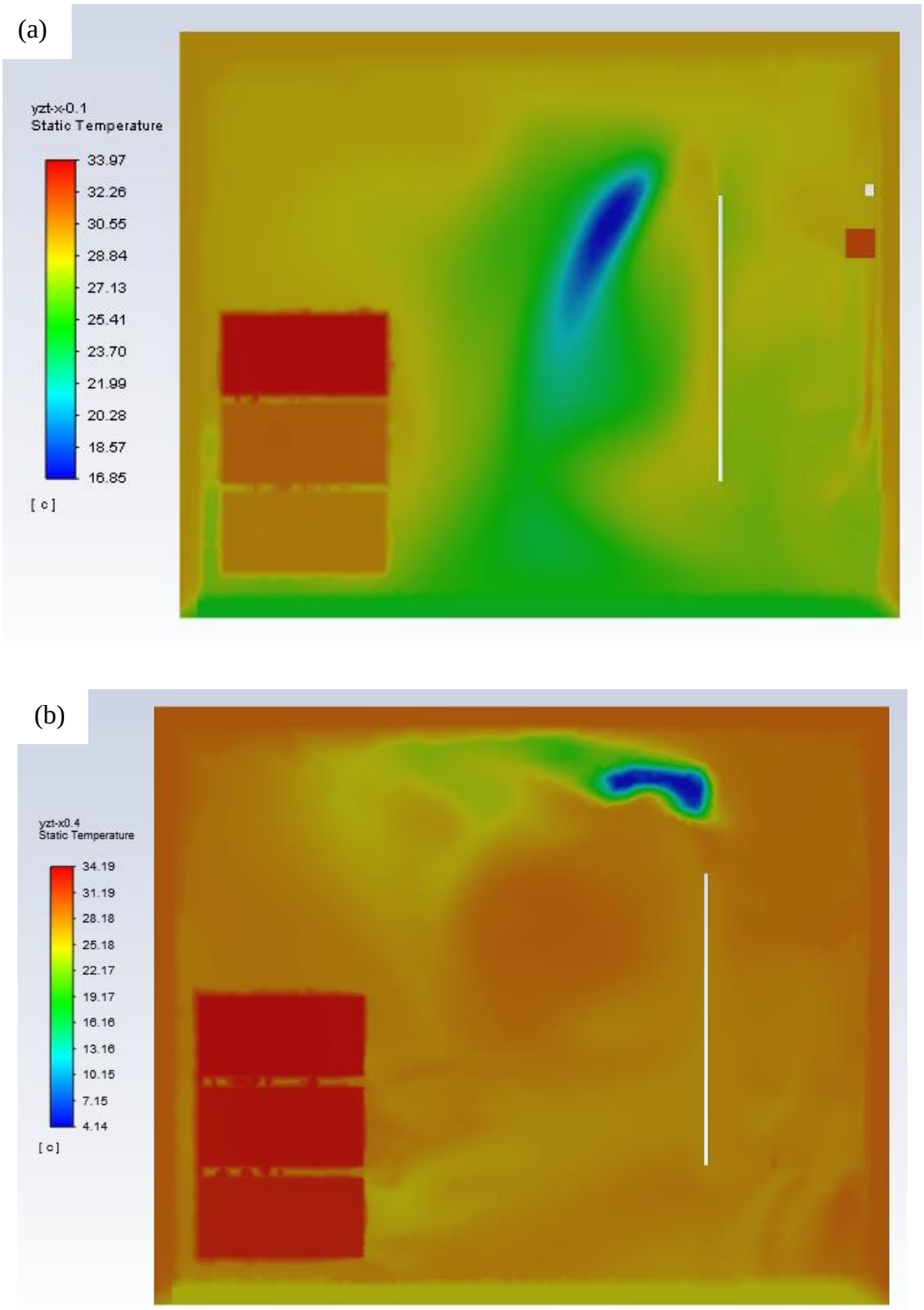

Figure 23. Temperature contours with the white vertical line representing a section of the safety barrier in (a) Plane 9 and (b) Plane 10

4.7.3 Temperature contours in the XZ plane

The last set of temperature contour results are in the XZ plane, where it was determined that temperature contours in 3 planes were necessary to display the thermal profile. The respective planes are shown in Figure 24.

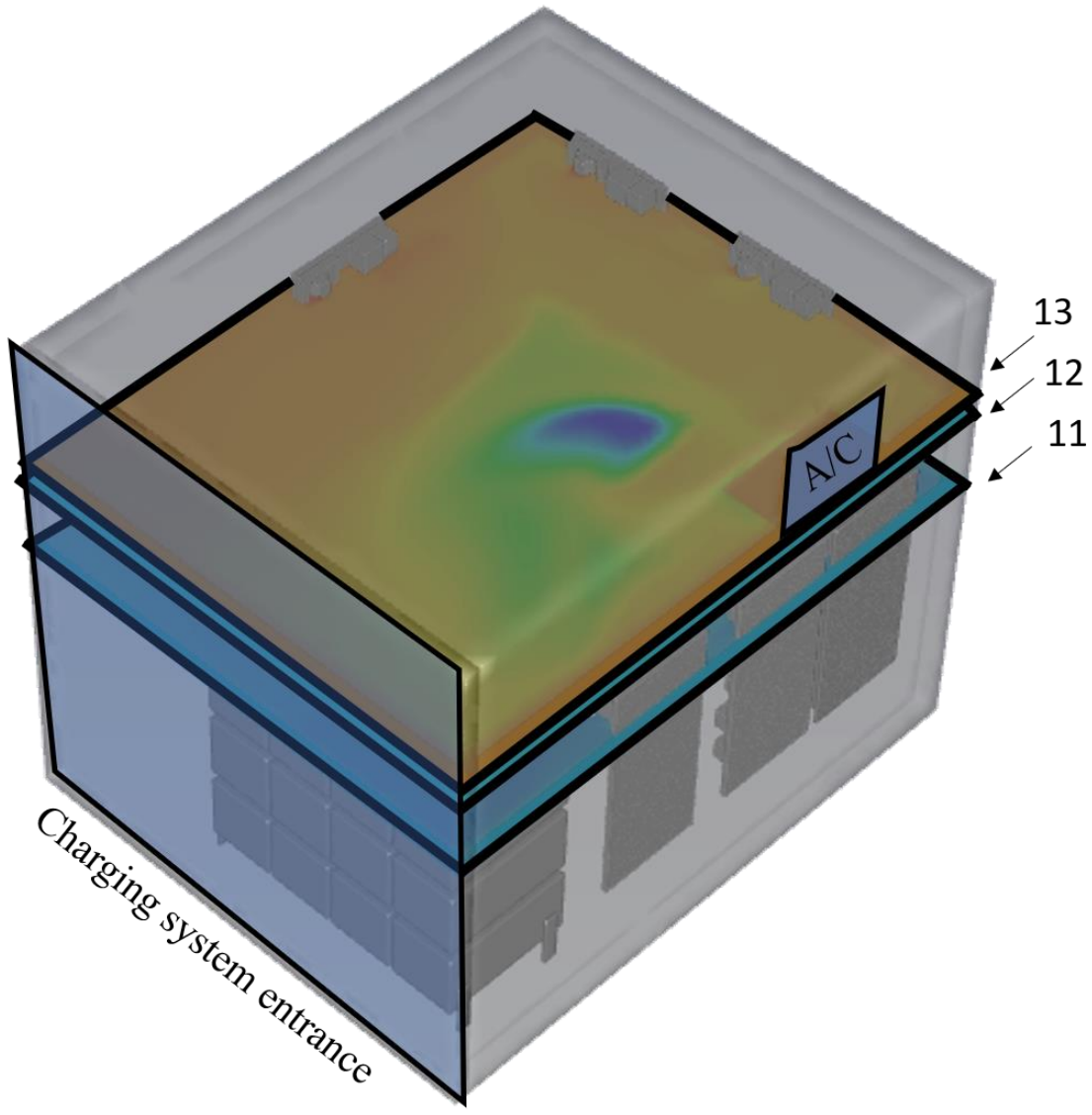

Figure 24. Planes (numbered from 11 to 13) used to display the temperature contours in the XZ plane

Figure 25a, displaying Plane 11, shows that there is a low-temperature region ranging from 21.89℃ to 28.42℃ in the middle of the charging system. It can be observed due to the presence of the safety barrier, indicated by the white region in the top-center of the figure, the cold air region is unable to mix with the region on the other side. There are three high-temperature regions generated, observed on the bottom-right side. On the top right side, a component can be observed with the temperature range from 44.76℃ to 48.03℃. On the middle right side, a region with temperatures ranging from 48.03℃ to 54.56℃ representing two components (components #14 and #15) installed on an electrical panel.

Figure 25b displays Plane 12, a similar low-temperature region can be observed to also be present in this region of the charging system. The location of this plane is shown in Figure 24. The presence of the low-temperature region ranges from 18.14℃ to 22.58℃ shows the behaviour of the air in different regions of the charging system. Additionally, there are 3 high-temperature regions generated due to the presence of component #9, which is installed on separate panels. The regions can be identified with temperatures from 35.88℃ to 62.50℃.

Figure 26 displays Plane 13 and shows a surrounding region with temperatures from 29.53℃ to 32.80℃, represented by yellow, orange, and red regions. The cold regions are in the middle of the figure, with temperature ranging from 16.43℃ to 26.25℃ (i.e., green and blue colours). It can be observed that the low-temperature region is also at the bottom of the image, which is where the battery packs are located. This is due to the air conditioner inlet air, where the air conditioner can be observed at the top right of the figure.

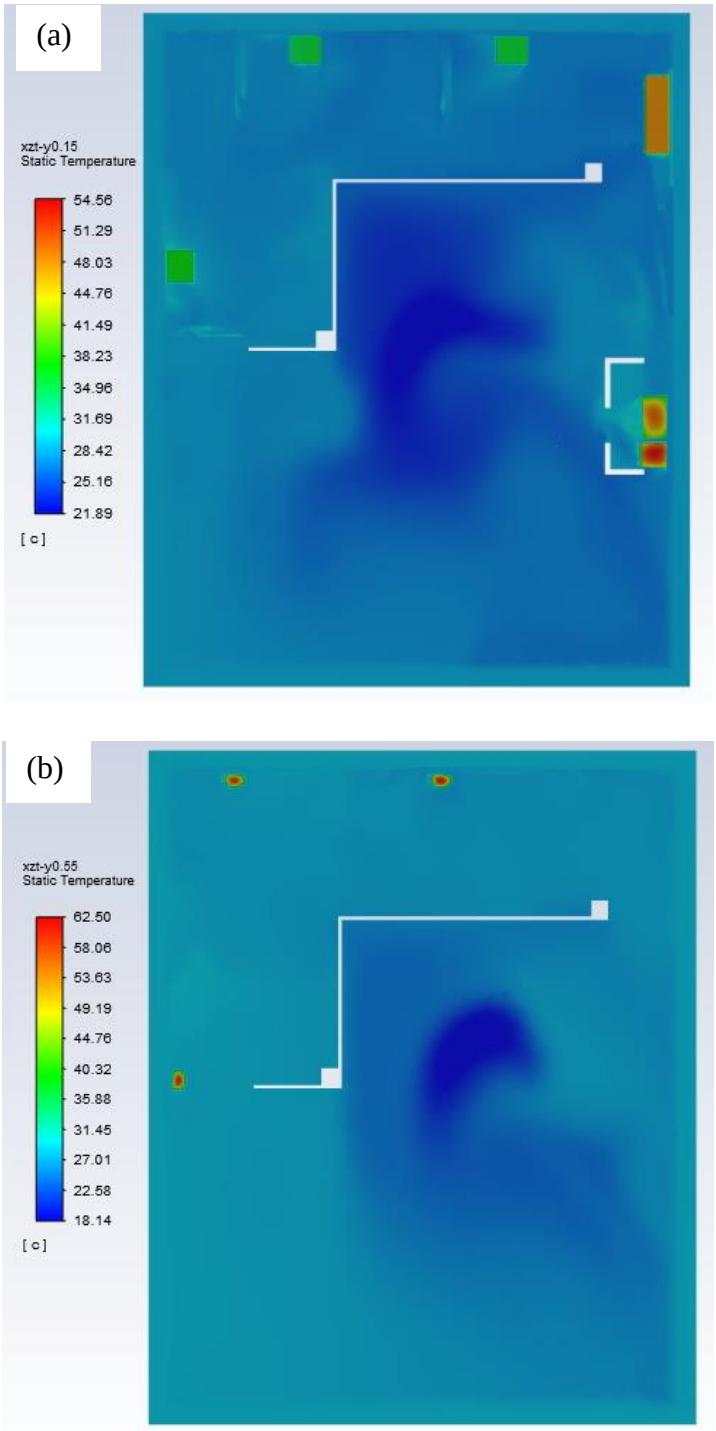

Figure 25. Temperature contours in (a) Plane 11 with the white lines at the top representing the safety barrier and the bottom white marks representing the electrical cover panel and (b) Plane 12 with the white lines representing the safety barrier

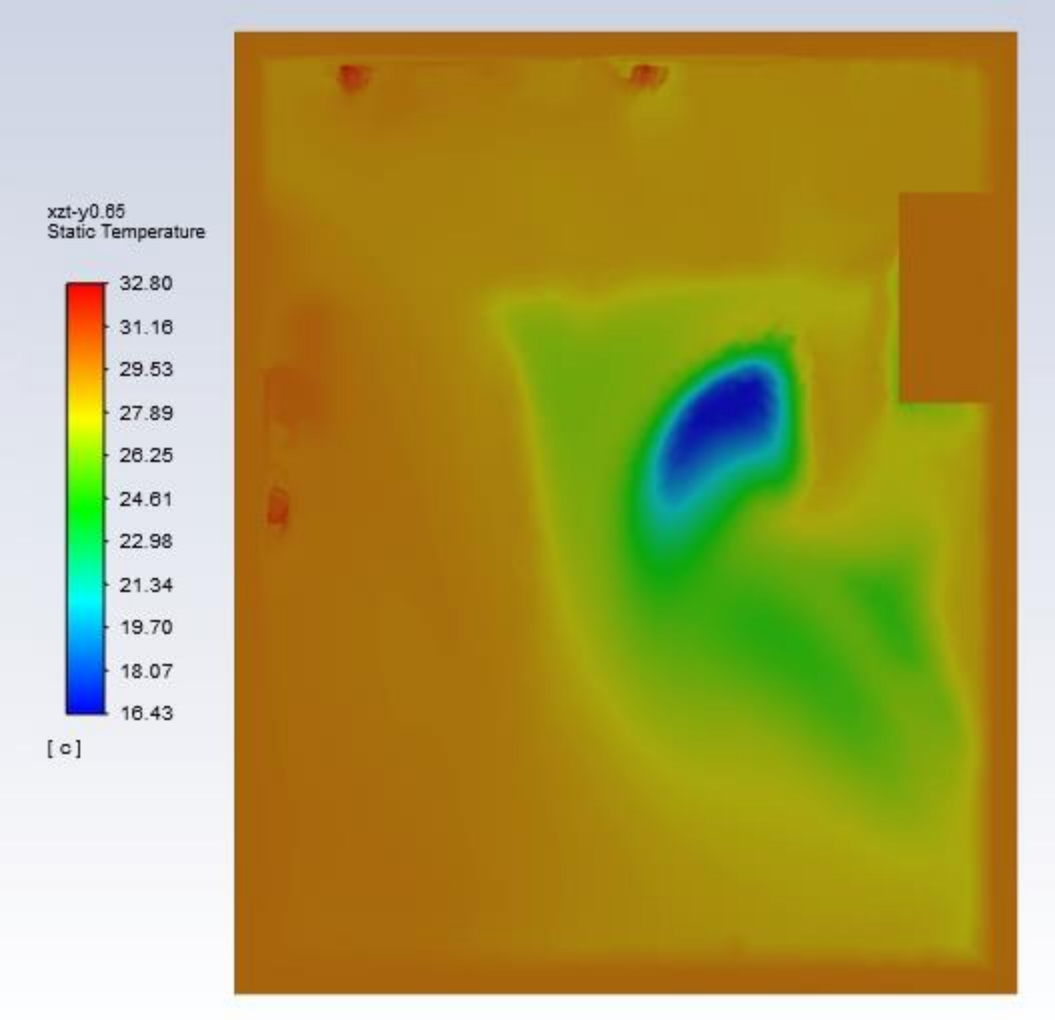

Figure 26. Temperature contours in Plane 13

4.8 Velocity Streamlines

The velocity patterns are represented by the mean velocity streamlines, which are generated in a similar manner to the temperature contours by following the coordinate system in Figure 16. Table 13 lists the names of the velocity streamline, its corresponding plane, and the plane number. It is important to generate velocity streamlines as it allows for an in-depth view of airflow inside the charging system, allowing for identification of high flow regions, low flow regions, regions of recirculation, and regions of stagnation.

The velocity streamlines shown from Figure 28 to Figure 38 are represented by various views. Similar to the temperature contours, the analysis of the mean streamlines will be split into the 3 plane views. The analysis begins in the XY plane view, then the YZ plane view, and finally, the XZ plane view.

Table 13. Velocity streamlines generated with corresponding planes

Plane Location	Plane Number	Plane
Plane-z0.15	14	XY Plane
Plane-z0.65	15	
Plane-z1.15	16	
Plane-z1.25	17	
Plane-z1.35	18	
Plane-x-1.4	19	YZ Plane
Plane-x-1.0	20	
Plane-x-0.9	21	
Plane-x-0.8	22	
Plane-x-0.6	23	
Plane-x-0.5	24	
Plane-x-0.4	25	
Plane-y-0.05	26	XZ Plane
Plane-y0.45	27	
Plane-y0.65	28	
Plane-y0.85	29	

4.8.1 Velocity streamlines in the XY plane

It was determined that 5 planes in the XY plane were necessary to analyze the velocity streamlines generated. The respective planes are shown in Figure 27.

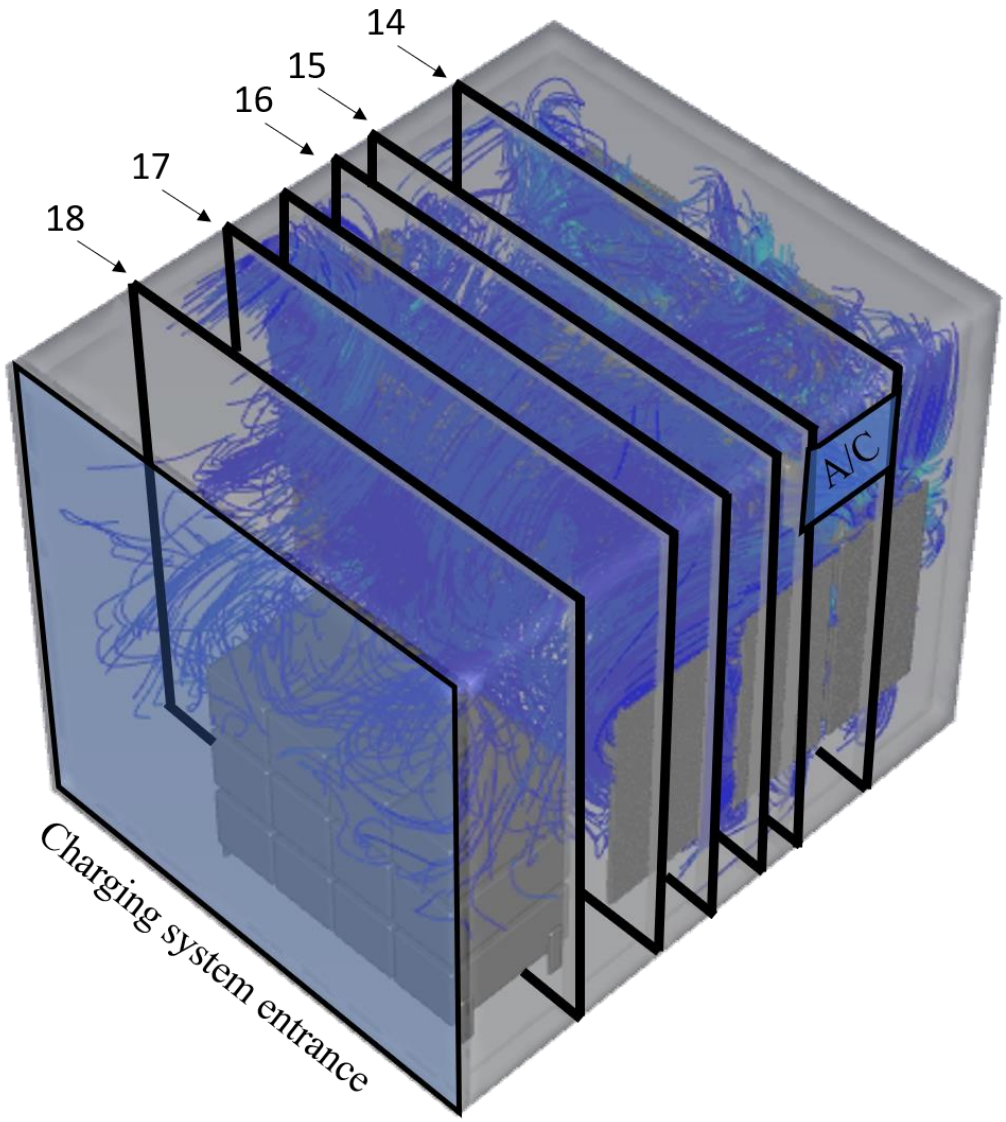

Figure 27. Planes (numbered from 14 to 18) used to display the velocity streamlines in the XY plane

Figure 28a displays the streamlines in Plane 14. The velocity streamlines with the velocity readings from 7.93 m/s to 13.22 m/s represent fans installed on an electrical panel. It is observed that they spread due to an impact with components in the corresponding panel. Various stagnation and recirculation regions are generated in the figure, which can be identified on the left-side, right-side, and the middle of the figure. The recirculation regions indicate that mixing within the system is optimal.

Figure 28b displays the streamlines in Plane 15, where it was observed to have a region that was directly impacted by the presence of the safety barrier. The region impacted can be seen on the right side of the figure, where the movement of the velocity streamlines spread outwards. A view of the fans, mentioned previously, are observed to have the same movement as Figure 28a.

Figure 29a shows the streamlines in Plane 16, indicating that at the left side of the figure is a high-velocity region ranging from 10.58 m/s to 26.45 m/s. It is indicative of the presence of the powerful blower, previously identified in Figure 9a. It can be seen that this streamline travels upwards moving from the left side (where the blower is present) to the right side. There is also a circulation region which can be seen in the middle of the figure. There is a large amount of air movement in the middle region of the charging system, which is further explored later.

Figure 29b and Figure 30 displaying Plane 17 and Plane 18 show the downward movement of airflow, examined at the center of the figures, which originates from the fan and air conditioner settings. This continuation is from the observation made from Figure 29a. It can also be explained when examining the YZ plane view of Figure 33a as it displays the airflow that is caused by the battery fan and its impact on this velocity streamline. On the

right side of Figure 30, the velocity streamlines surround a region which is identified to be the cover panel of an electrical panel.

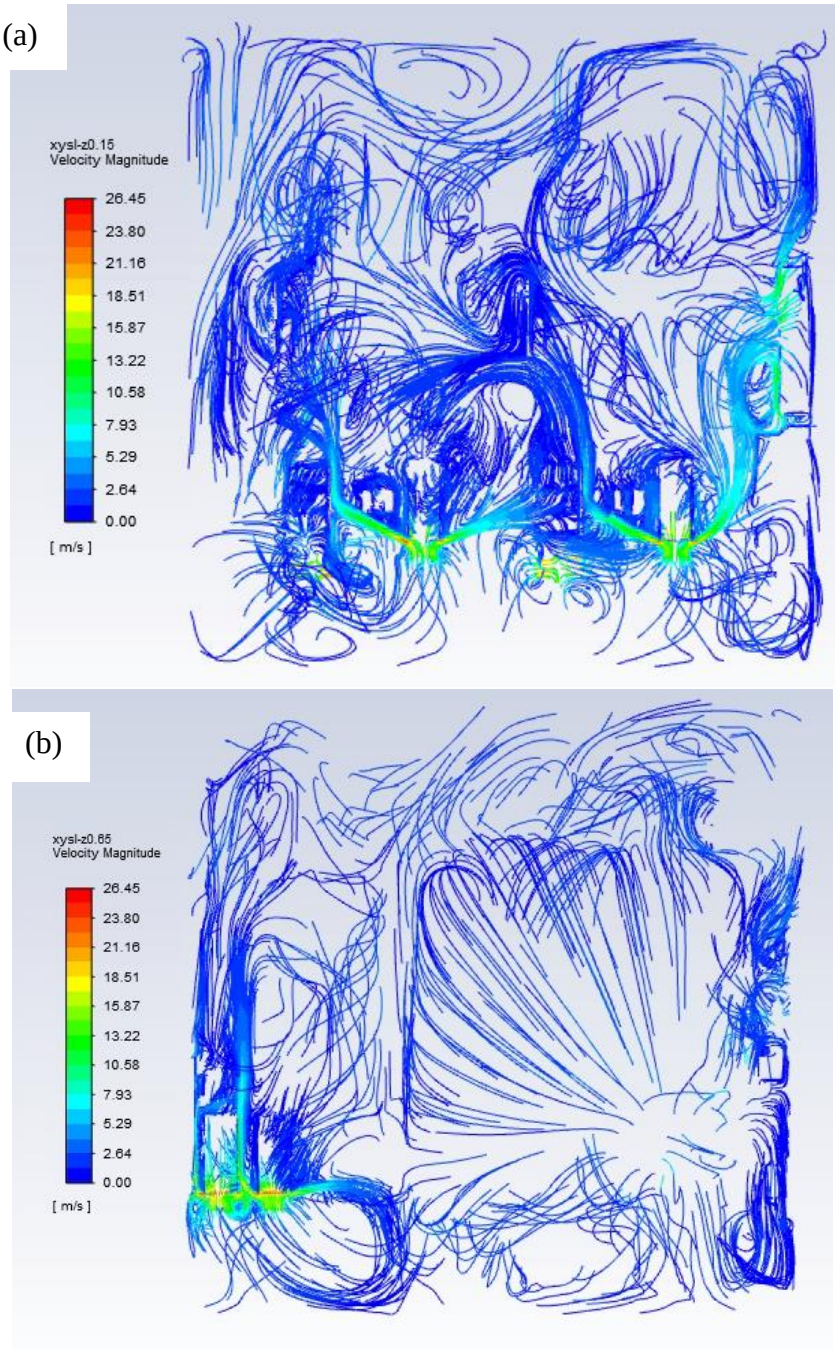

Figure 28. Velocity streamlines of (a) Plane 14, and (b) Plane 15

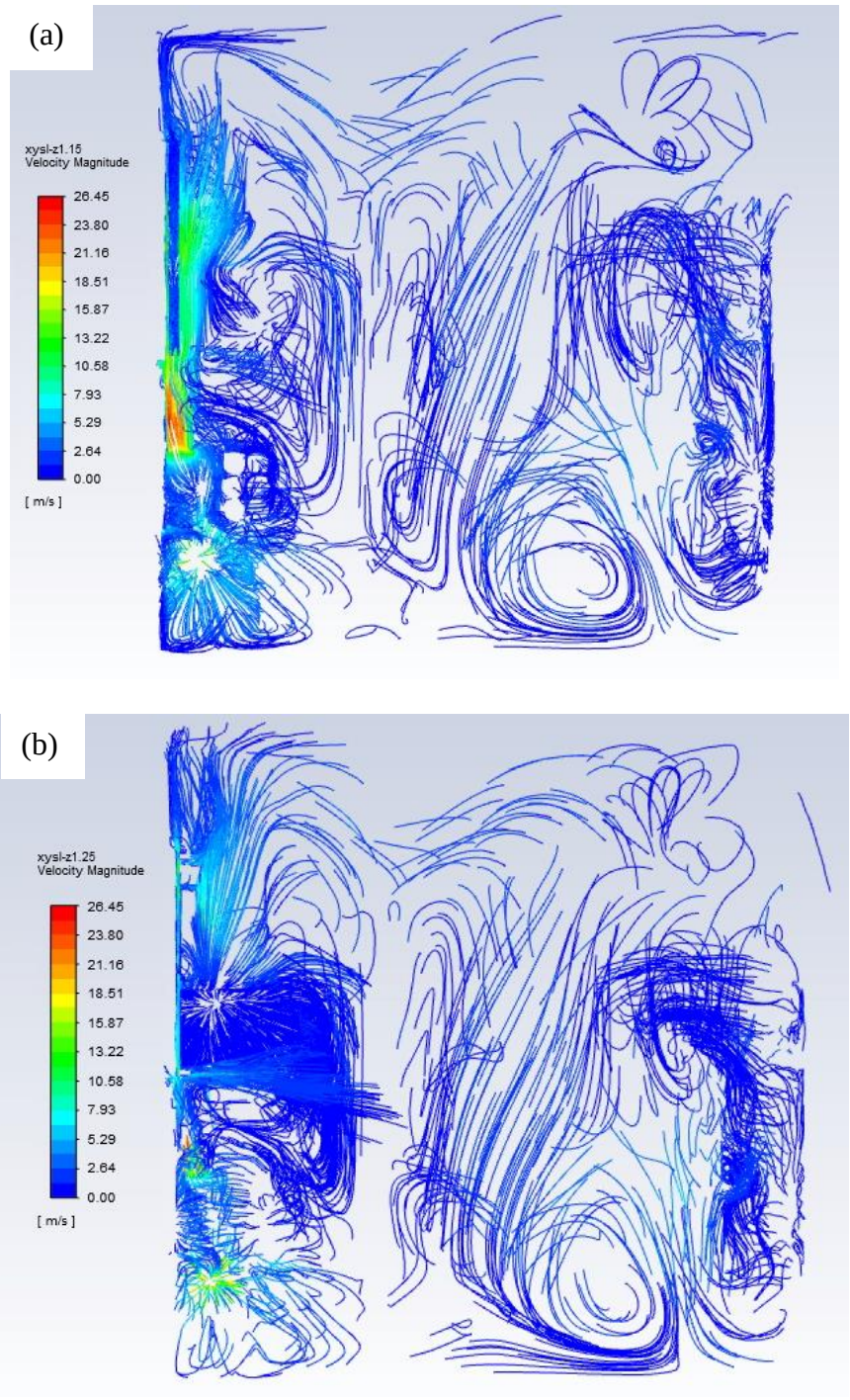

Figure 29. Velocity streamlines of (a) Plane 16, and (b) Plane 17

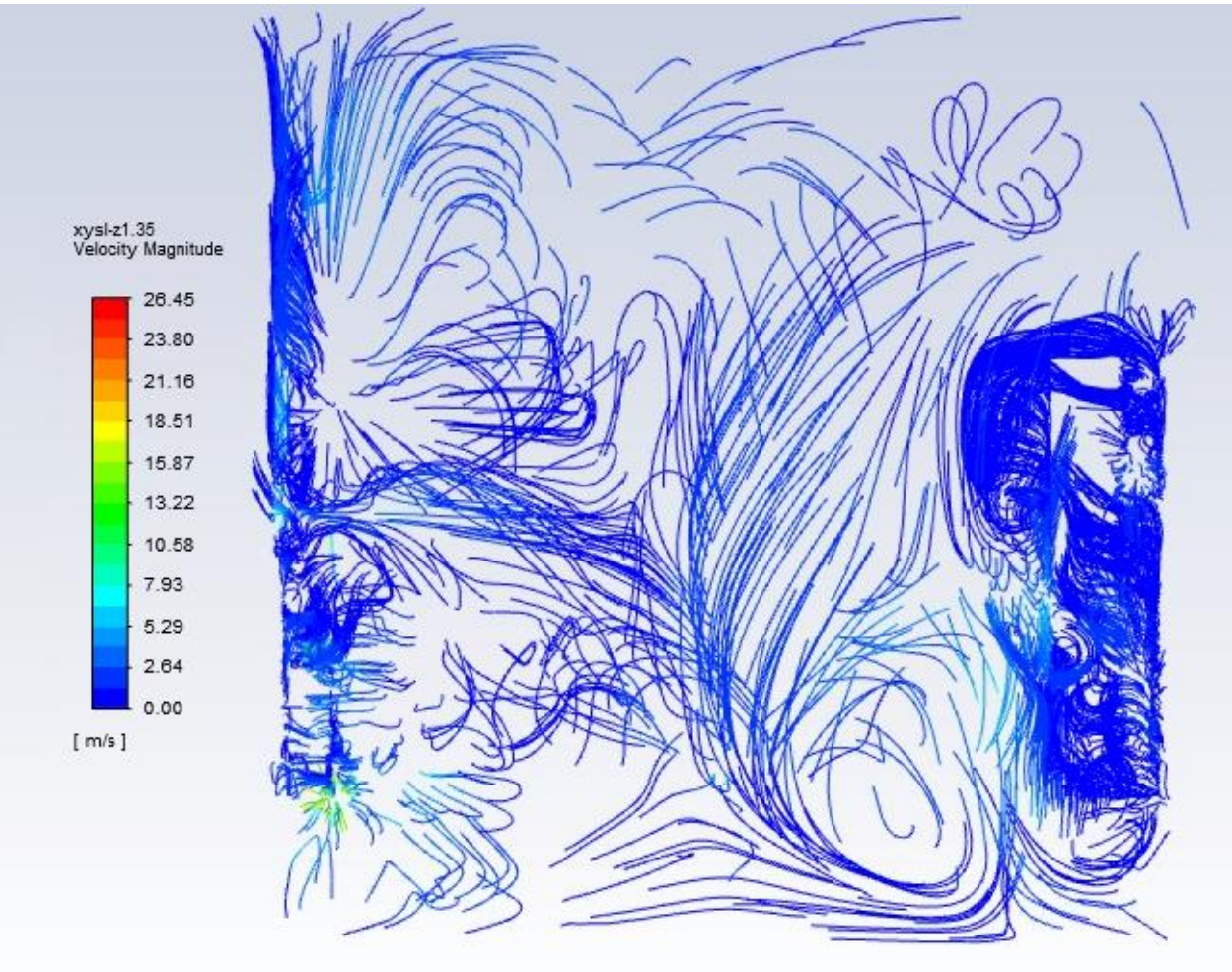

Figure 30. Velocity streamlines of Plane 18

4.8.2 Velocity streamlines in the YZ plane

It was determined that 6 planes were necessary to analyze the velocity streamlines in the YZ plane. The corresponding planes are shown in Figure 31.

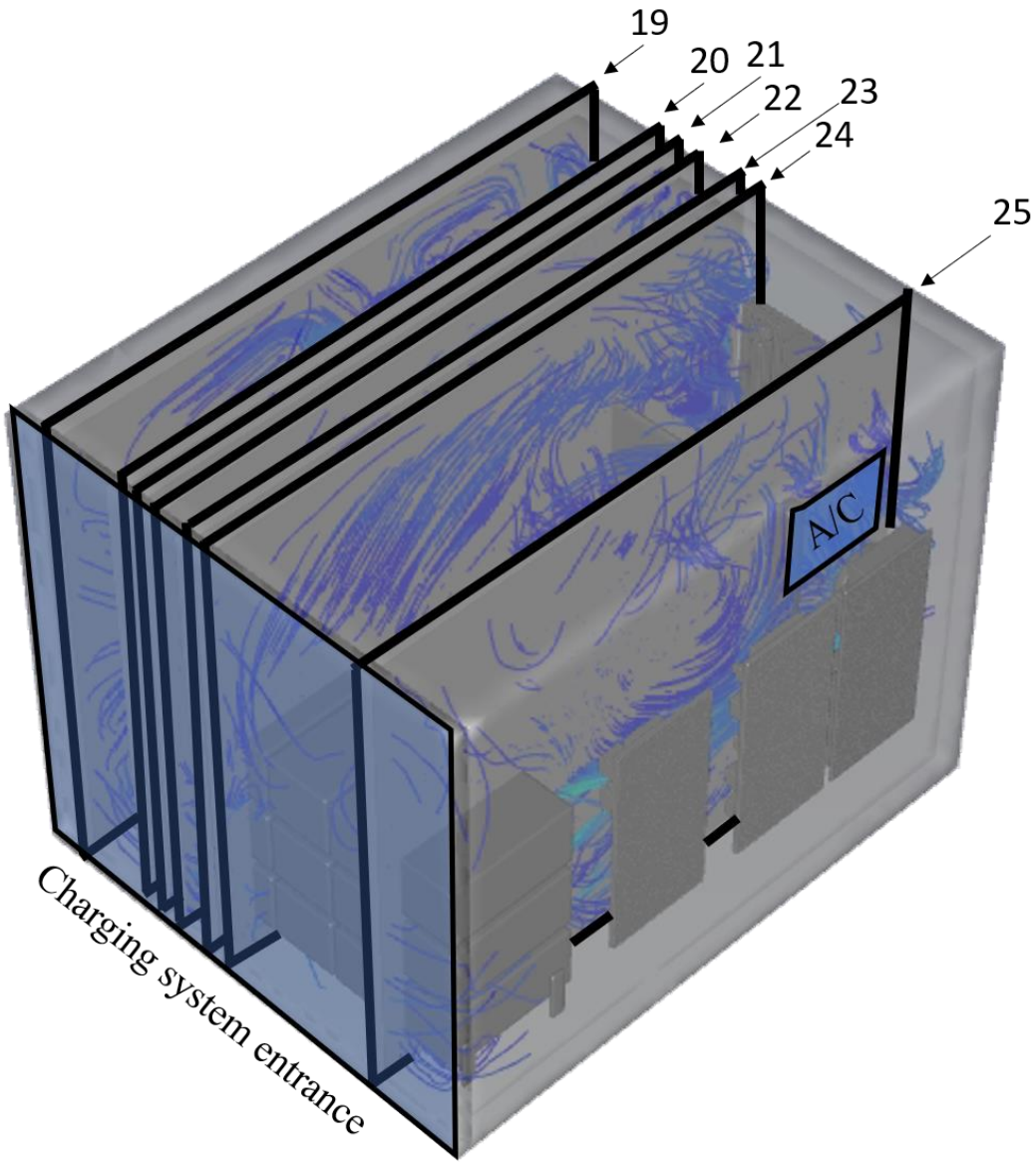

Figure 31. Planes (numbered from 19 to 25) used to display the velocity streamlines in the YZ plane

Figure 32a displays the results in Plane 19 which features a view of the airflow from 7.51 m/s to 12.52 m/s in the middle of the figure. The velocity streamlines cover several electrical panels. It can be identified that due to the fans, the streamline patterns are upwards towards the roof.

Figure 32b representing Plane 20, features an additional view of the blower, which can be identified by the high-velocity region on the right-side view of the figure. In addition to this, at the top and bottom of the figure, it is observed that the air moves in a large circular pattern, moving from the top right side where it reaches the left side, then from the left side towards the right side via the bottom of the charging system. This illustrates that the airflow is causing regions to develop complex patterns within the charging system. Within Figure 32b, it is observed that in the middle of the figure a vortex is generated that travels from the top of the figure to the bottom.

Figure 33a and Figure 33b display the results in Plane 21 and Plane 22, which features additional views of the evolution of the streamlines in different regions of the charging system. The circular motion of the air, similar to Figure 32b can be observed to continue in this region as well. Figure 33a features the vortex generated in the charging system with stagnation regions in the bottom left corner. Figure 33b features a mix of stagnation and recirculation regions as a result of the circular motion of the air in the charging system.

Figure 34a and Figure 34b displaying Plane 23 and Plane 24 show the impact of the air movement at the roof of the charging system and how it travels towards the battery packs. This movement of air can be attributed to a combination of the fan and blower combinations. As observed in Figure 32b, the blower causes the air to move upwards, which results in the air moving towards the battery packs.

Figure 35 displays the results in Plane 25, which provides valuable information on the airflow caused by the battery fans, which can be identified in the velocity regions ranging from 7.93m/s to 15.87m/s. The battery fans are located on the left side of the figure. This can also explain cold airflow from the air conditioner displayed in Figure 23 and Figure 26 from the temperature contour results.

It should be noted that the battery fans blow air in a different direction based on the location of the battery fan, as they were set differently. The locations can be referenced in Figure 30.

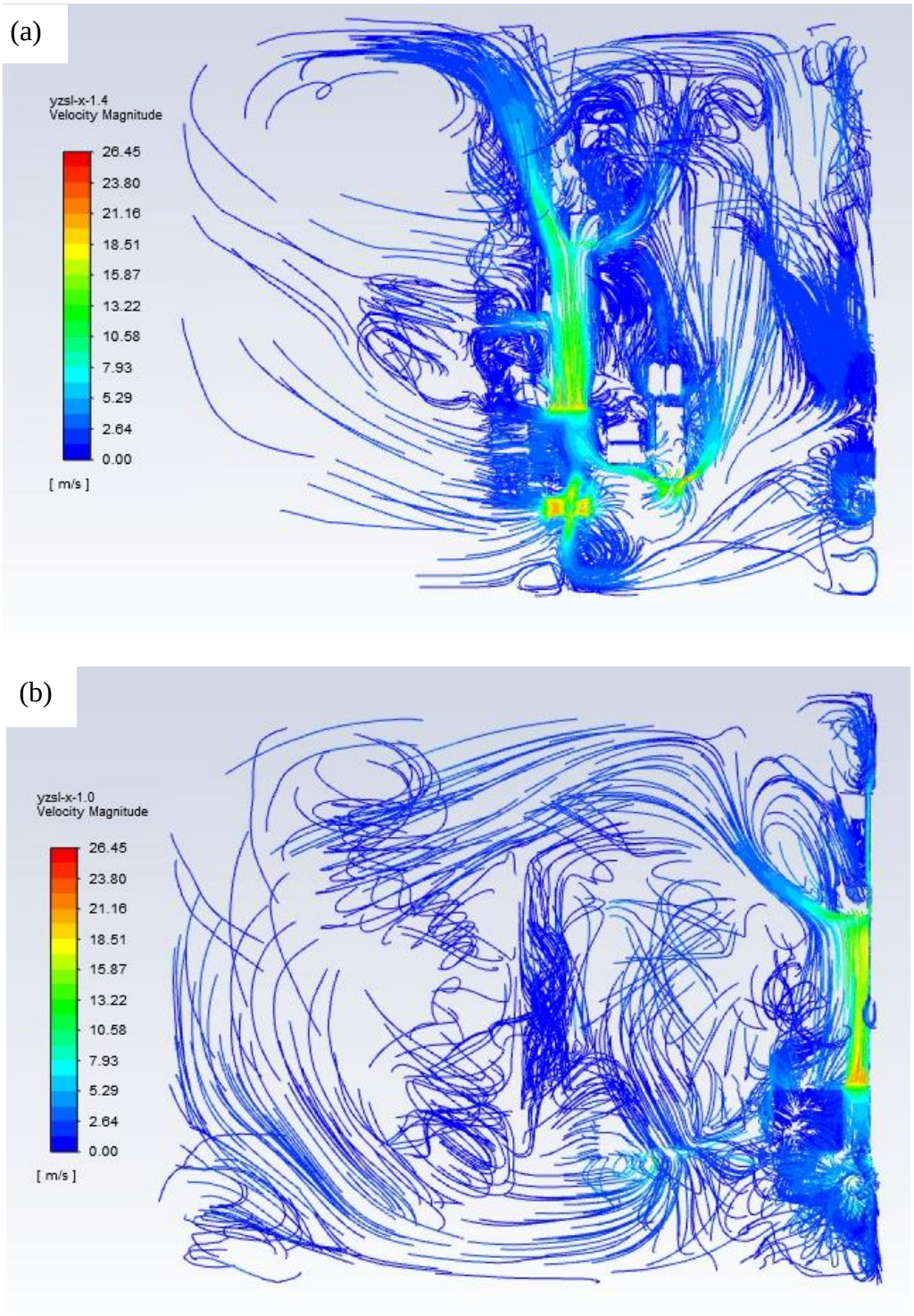

Figure 32. Velocity streamlines of (a) Plane 19, and (b) Plane 20

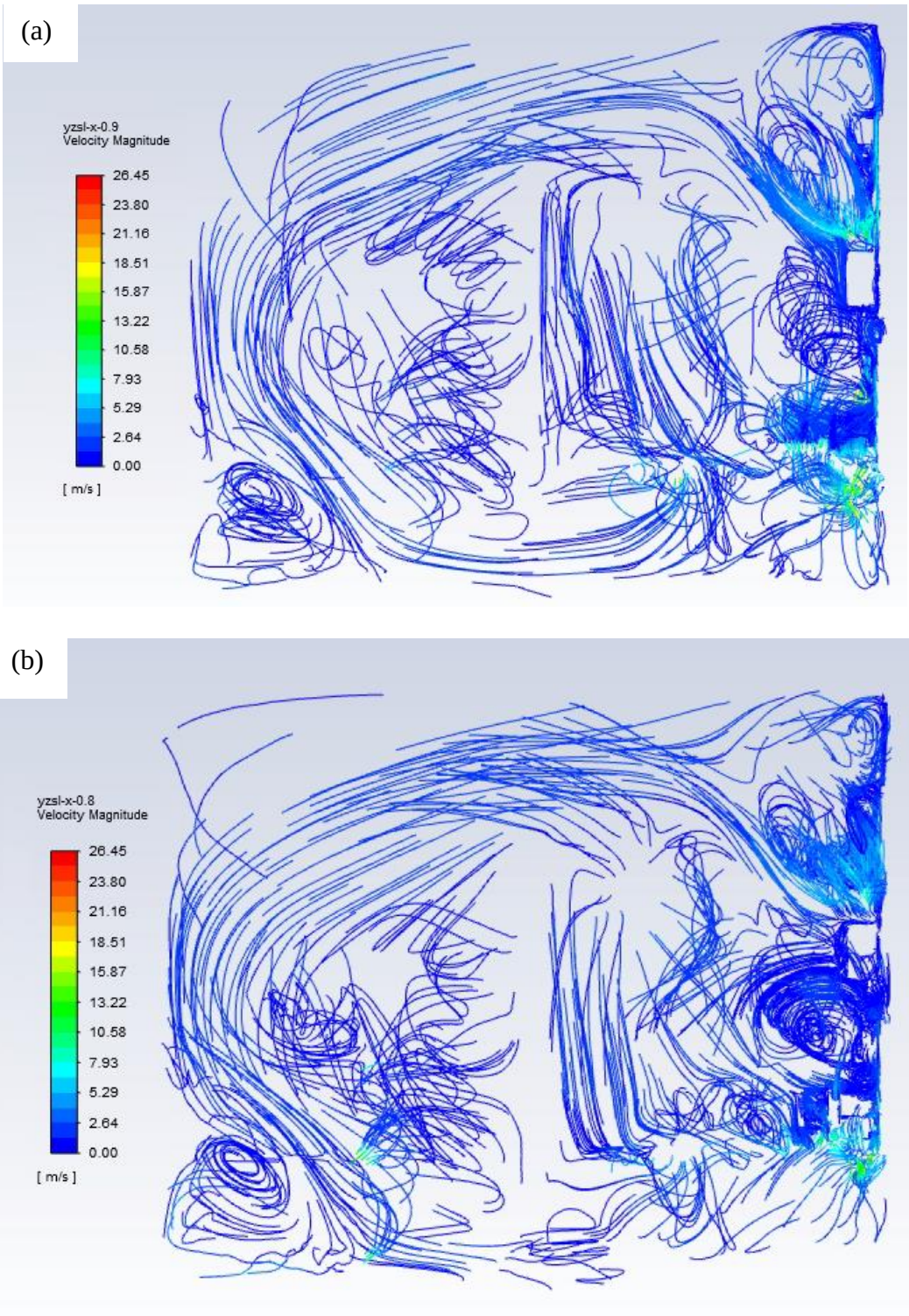

Figure 33. Velocity streamlines of (a) Plane 21, and (b) Plane 22

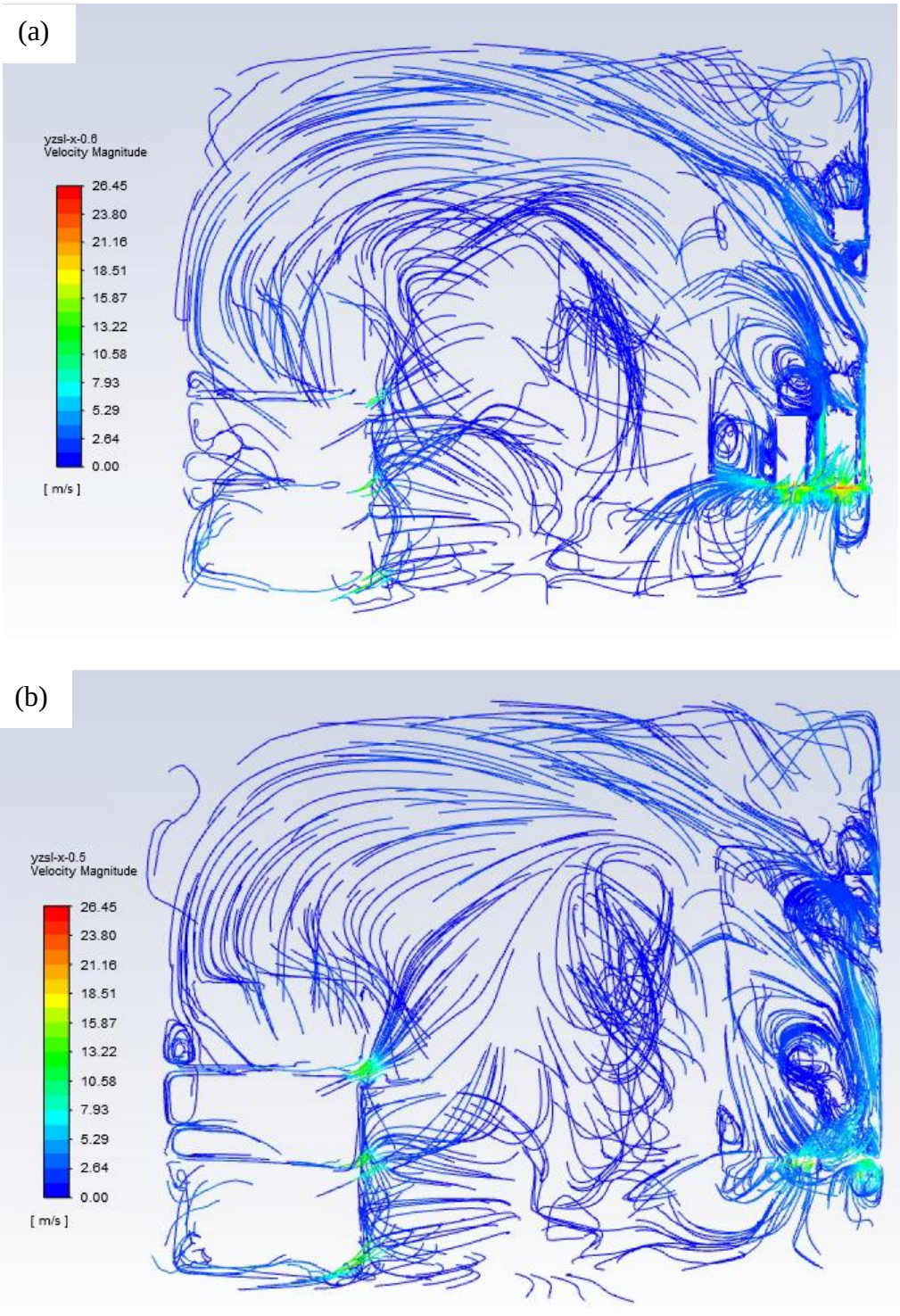

Figure 34. Velocity streamlines of (a) Plane 23, and (b) Plane 24

Figure 35. Velocity streamlines of Plane 25

4.8.3 Velocity streamlines in the XZ plane

It was determined that 4 planes in the XZ plane were necessary to analyze the velocity streamlines generated. The planes used in the analysis are shown in Figure 36.

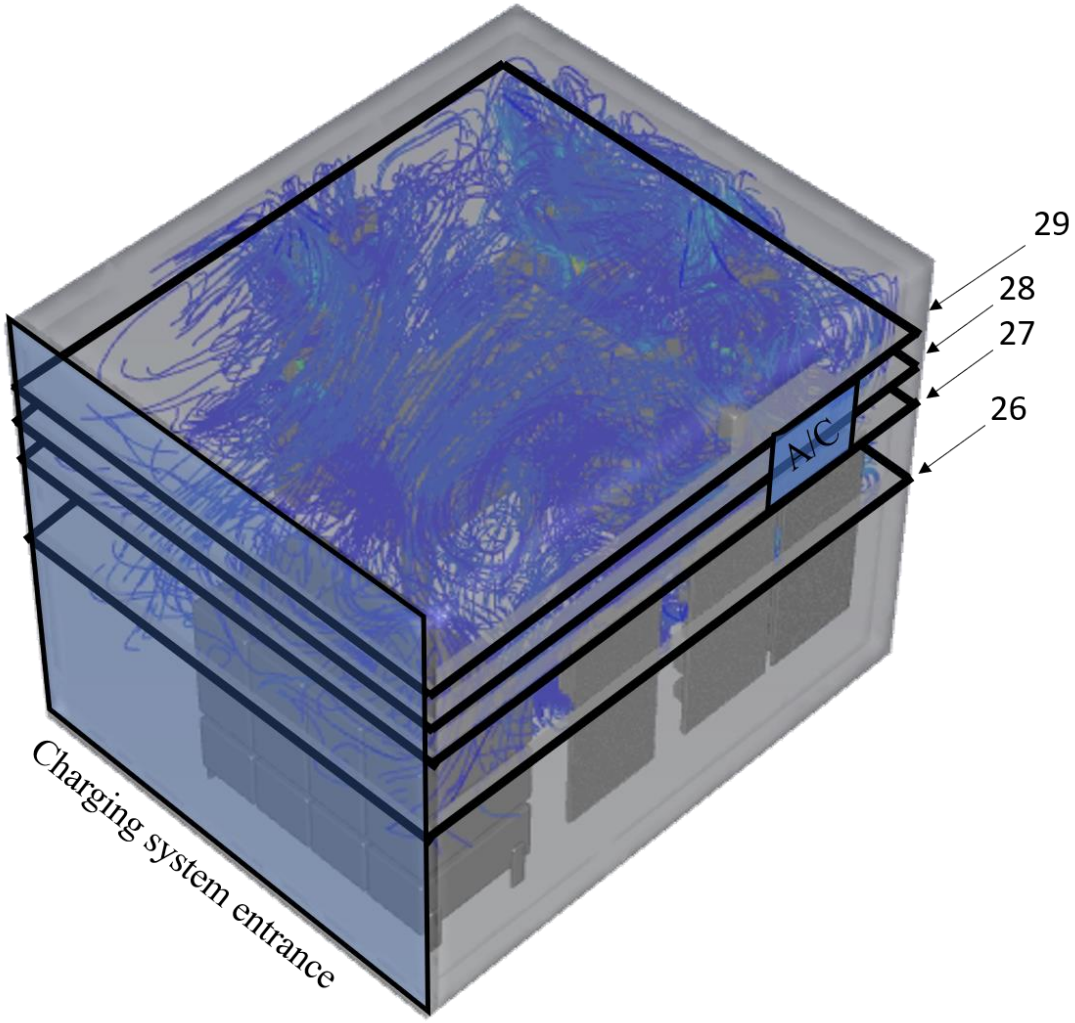

Figure 36. Planes (numbered from 26 to 29) used to display the velocity streamlines in the XZ plane

Figure 37a features Plane 26, where a view of the blowers can be identified on the left-side and top of the figure, indicated by the regions showing velocities from 7.93 m/s to 26.45 m/s. In addition to this, the velocity streamlines can be seen to exhibit two types of behaviours when encountering the safety barrier, which is in the center of the charging system. The streamlines are observed to flow around the barrier where they eventually evolve into a stagnation region on the left side of the figure, or they impact the barrier and are unable to flow around it. The extent of the velocity streamlines caused by the blower can be seen developing recirculation regions at the top and left side of Figure 37a.

Figure 37b, displays Plane 27, which can be observed to identify the end of the airflow from the blower by the regions at the top and left side where the velocities are observed to be 5.29 m/s to 7.93 m/s. On the left of the figure, the recirculation region caused by the safety barrier can also be easily identified, indicating that the region is developing in various heights of the charging system. The end of the recirculation region from the safety barrier can be identified in Figure 37b, being covered by the resulting airflow from the blower at the left-side.

Figure 38a and Figure 38b display Plane 28 and Plane 29. These figures show the movement of the airflow at the roof of the charging system. It can be identified, similar to Figure 37b, the remnants of the resulting airflow from the blowers are present. Additional observations from these figures present the movement of air from the middle of the figure towards the bottom, where the battery packs are located. This has been widely observed in many of the results, and it is seen to be present in the roof of the charging system.

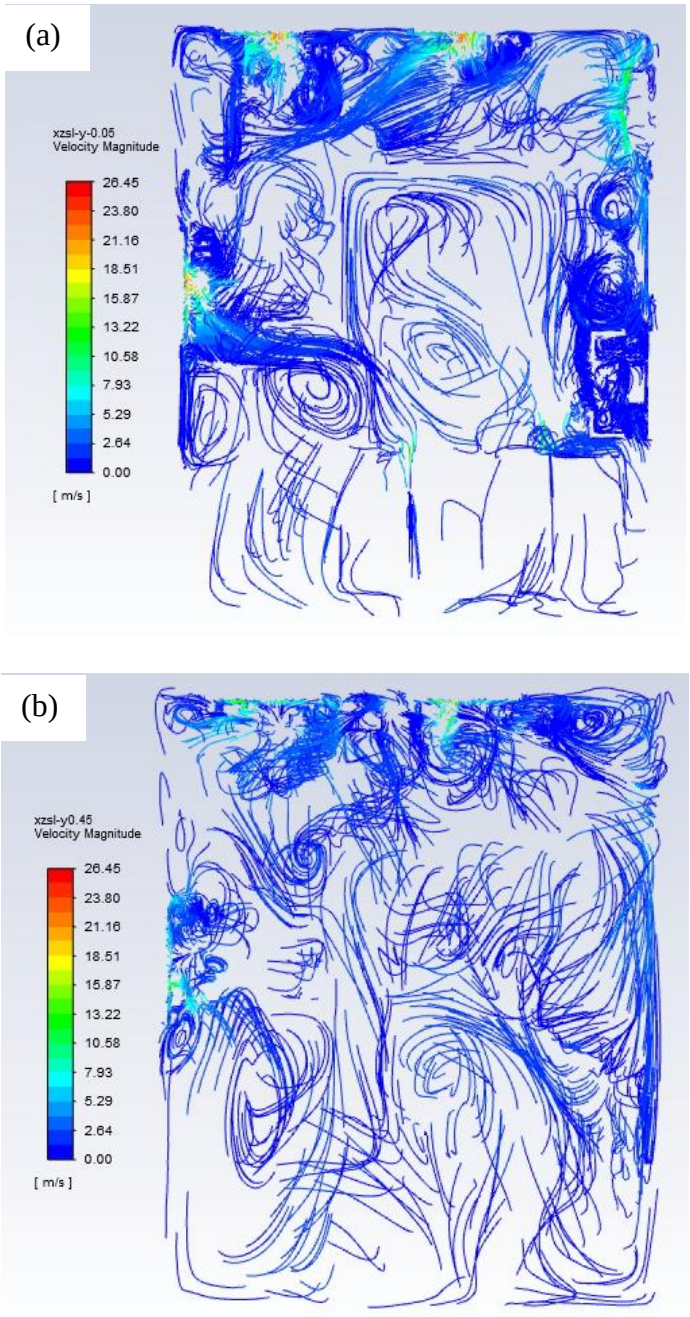

Figure 37. Velocity streamlines of (a) Plane 26, and (b) Plane 27

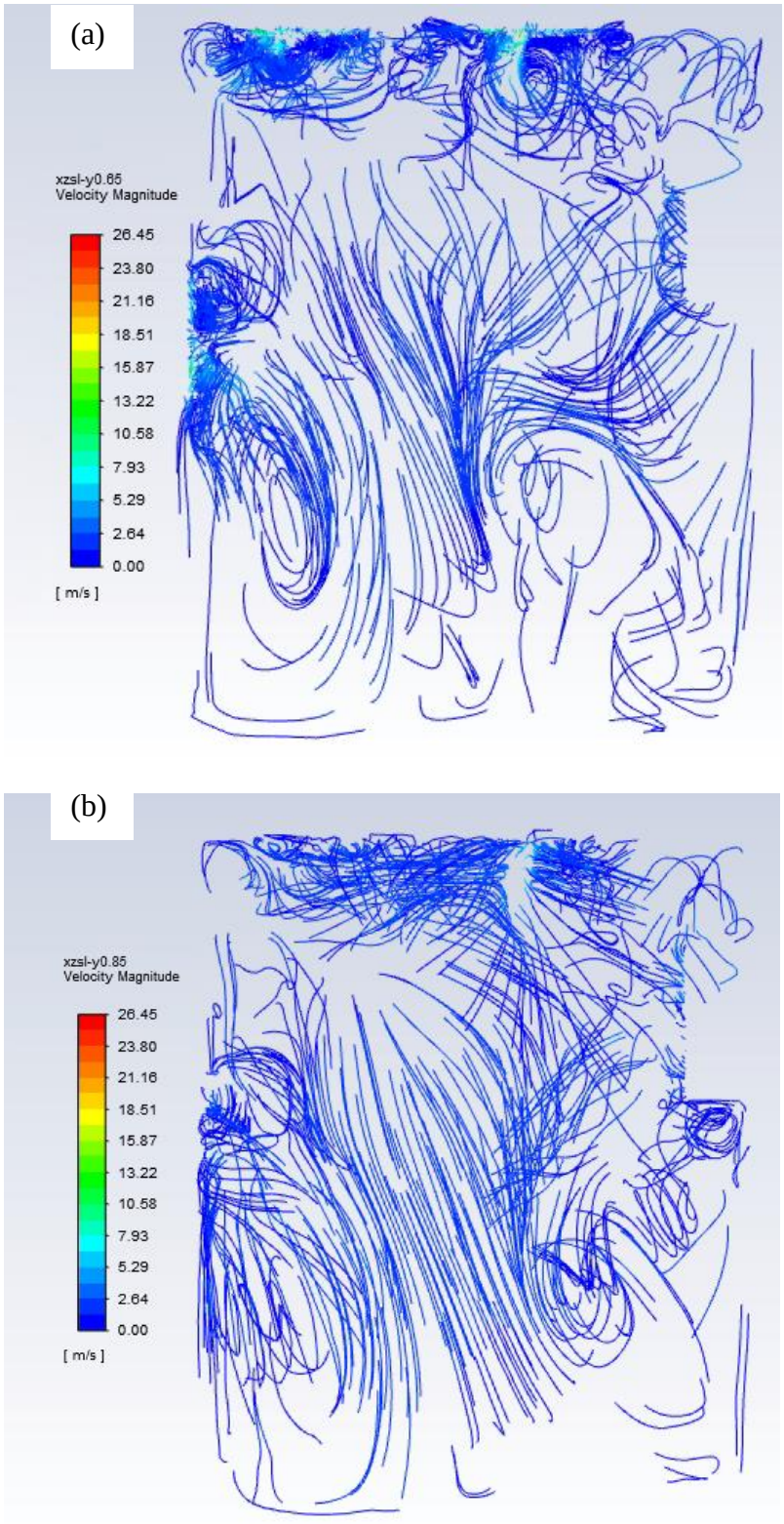

Figure 38. Velocity streamlines of (a) Plane 28, and (b) Plane 29

Chapter 5: Conclusions and Recommendations

5.1 Conclusions

In conclusion, an integrated thermal model for an innovative electric vehicle charging system was developed as a virtual design tool. It is capable of performing parametric and optimization studies by varying the boundary conditions, air conditioner settings, and the directions as well as locations of the fans/blower. This can be done without impacting the full workflow.

The temperature iso-surfaces were generated to identify the volume of the air within the charging system that was within the operating range of lithium-ion batteries. It demonstrated that a large percentage of the volume in the charging system was within this range, with the iso-surface temperatures above this range being concentrated at the electrical components that have higher heat generation.

Furthermore, it was observed that the blowing direction of the fans in proximity to the batteries has a significant impact on the cooling of the batteries. The direction of the battery fans affected the distribution of temperatures across the batteries. The existing configuration has one set of fans blowing air through the batteries, and another set of fans blowing air away from the batteries. The result was cooler temperatures in the section that experienced airflow through the batteries.

The Rack Cooling Index (RCI) results were also examined, where the resulting battery surface temperatures were quantified based on their operating temperature range. A major reduction in surface temperature was examined by comparing cases. The existing configuration of the charging system (Case 3), was identified to effectively cool the

batteries with a maximum temperature of 35.61℃. Three studies resulted in a reduction in the maximum battery surface temperatures. These studies were identified to be Case 4, where the battery fan directions were changed, Case 6 with the air-conditioner placement on a different wall, and Case 7, where the safety barrier was given perforations. The results were validated with temperatures measured at selected locations inside the charging system, as shown in Appendix A. Case 4 results in the greatest number of batteries with the highest RCI values, indicating that the configuration with the changes in battery fan directions is the most effective cooling method.

In addition, the velocity streamlines provide a better understanding of the airflow pattern inside the charging system. The results showed how the presence of the safety barrier in the charging system affects the airflow by diverting it in different directions and/or creating stagnation regions. The results show that the battery fans are instrumental in the circulation of air, but they are impacted by the presence of the barrier.

5.2 Limitations

The thesis involves a system level view of the thermal loads generated in the charging system. The limitations of the thesis are discussed in this section.

The first sources of error relate to the virtual model. The geometry of the charging system underwent essential defeaturing to allow development of a mesh that otherwise would be impossible. Defeaturing also prevented component complexities from impacting the calculation process. As stated previously, the resulting defeatured charging system maintains its unique construction and all of the components are recognizable. Although this is the case, the defeaturing may have had an effect on heat dissipation of the components as each component underwent a process to remove some features to allow for

successful mesh generation. Additional defeaturing to the charging system container may have removed gaps that allowed for air infiltration.

In addition, the heat generation source terms were used for a solid component, whereas many electrical components have an internal structure that varies in heat generation rate and construction. Thus, a simplification was made to apply a singular volumetric heat generation on the solid electrical component and assigning a material that matched the surface of the material. A further study could involve an analysis of the internal structure of the electrical components to examine the nuances of how the heat is generated and dissipated at the surface.

5.3 Recommendations for Future Work

There are several recommendations for future work to improve both the virtual model and the physical electric vehicle charging system.

For the virtual model, mesh morphing capabilities (the rbf-mesh morph add-on [87]) can be incorporated to allow for a real-time update of the mesh when certain geometrical changes need to be applied to the system. This also allows for an expedition of the mesh generation process, which can currently take up to 12 hours to complete.

For the electric vehicle charging system, it is recommended that battery fans/blowers should be oriented so that they all blow air towards the battery pack. Half of them currently blow air away from the battery pack. In addition, the safety barrier should have holes to improve airflow and cooling as there are circulation issues due to the presence of the barrier.

5.4 Contributions

This research was conducted in collaboration with eCAMION Inc. The model discussed in this thesis is used as a tool to aid the industry partner in analyze their system thermally when changes are made. This tool allows for optimization of the system when certain configurations are identified that improve exhibited temperature loads within the charging system. The model's use as a design tool was aided by the preparation of a user's guide, that guided the user through the use of the design tool by explaining how to access and use each aspect of the model (geometry, mesh, set-up, and post-processing).

References

[1] "Canada's actions to reduce emissions," 2019. [Online]. Available: https://www.canada.ca/en/services/environment/weather/climatechange/climate-plan/reduce-emissions.html. [Accessed: 04-Mar-2020].

[2] "Our low carbon transportation future," 2018. [Online]. Available: https://www.canada.ca/en/services/environment/weather/climatechange/climate-action/low-carbon-transportation-future.html. [Accessed: 04-Mar-2020].

[3] I. Husain, *Electric and Hybrid Vehicles Design Fundamentals*. New York: CRC Press, 2005.

[4] X. G. Yang, G. Zhang, S. Ge, and C. Y. Wang, "Fast charging of lithium-ion batteries at all temperatures," *Proc. Natl. Acad. Sci. U. S. A.*, vol. 115, no. 28, pp. 7266–7271, Jul. 2018, doi: 10.1073/pnas.1807115115.

[5] "An Examination of Electric Vehicle Technology, Infrastructure Requirements and Market Developments: Office of Climate Change and Energy Efficiency - desLibris." [Online]. Available: https://www-deslibris-ca.uproxy.library.dc-uoit.ca/ID/10049411. [Accessed: 05-Mar-2020].

[6] S. H. Chung and C. Kwon, "Multi-period planning for electric car charging station locations: A case of Korean expressways," *Eur. J. Oper. Res.*, vol. 242, no. 2, pp. 677–687, 2015, doi: 10.1016/j.ejor.2014.10.029.

[7] M. Z. Zeb *et al.*, "Optimal Placement of Electric Vehicle Charging Stations in the Active Distribution Network," *IEEE Access*, vol. 8, pp. 1–1, 2020, doi: 10.1109/access.2020.2984127.

[8] H. Hõimoja, M. Vasiladiotis, S. Grioni, M. Capezzali, A. Rufer, and H. B. Püttgen, "Toward Ultrafast Charging Solutions of Electric Vehicles," 2012.

[9] S. Ahmed *et al.*, "Enabling fast charging – A battery technology gap assessment," *J. Power Sources*, vol. 367, pp. 250–262, Nov. 2017, doi: 10.1016/j.jpowsour.2017.06.055.

[10] M. Al-Zareer, "Development and Modeling of Novel Battery Thermal Management Systems for Electric and Hybrid Electric Vehicles," University of Ontario Institute of Technology, 2019.

[11] G. Karimi and X. Li, "Thermal management of lithium-ion batteries for electric vehicles," *Int. J. Energy Res.*, vol. 37, no. 1, pp. 13–24, Jan. 2013, doi: 10.1002/er.1956.

[12] K. T. Chau, Y. S. Wong, and C. C. Chan, "Overview of energy sources for electric vehicles," *Energy Convers. Manag.*, vol. 40, no. 10, pp. 1021–1039, 1999, doi: 10.1016/S0196-8904(99)00021-7.

[13] P. Gao *et al.*, "Cadmium hydroxide nanowires - New high capacity Ni-Cd battery anode materials without memory effect," *J. Mater. Chem.*, vol. 22, no. 28, pp. 13922–13924, 2012, doi: 10.1039/c2jm33169a.

[14] G. Bronoel, N. Tassin, R. Rouget, and T. Potier, "Sealed Bipolar Ni-Cd Batteries," in *IEEE 35th International Power Sources Symposium*, 1992, pp. 279–280, doi: 10.1017/CBO9781107415324.004.

[15] P. Sirisinudomkit, P. Iamprasertkun, A. Krittayavathananon, T. Pettong, P. Dittanet,

and M. Sawangphruk, “Hybrid Energy Storage of Ni(OH)2-coated N-doped Graphene Aerogel//N-doped Graphene Aerogel for the Replacement of NiCd and NiMH Batteries,” *Sci. Rep.*, vol. 7, no. 1, pp. 1–9, 2017, doi: 10.1038/s41598-017-01191-8.

[16] U. Köhler, J. Kümpers, and M. Ullrich, “High performance nickel-metal hydride and lithium-ion batteries,” *J. Power Sources*, vol. 105, no. 2, pp. 139–144, 2002, doi: 10.1016/S0378-7753(01)00932-6.

[17] M. Y. Chu, L. De Jonghe, and S. Visco, “High specific power lithium polymer rechargeable battery,” *Proc. Annu. Batter. Conf. Appl. Adv.*, pp. 163–165, 1996, doi: 10.1109/bcaa.1996.484988.

[18] Z. M. Salameh and B. G. Kim, “Advanced lithium polymer batteries,” *2009 IEEE Power Energy Soc. Gen. Meet. PES ’09*, pp. 1–5, 2009, doi: 10.1109/PES.2009.5275404.

[19] Y. Ye, Y. Shi, L. H. Saw, and A. A. O. Tay, “Performance assessment and optimization of a heat pipe thermal management system for fast charging lithium ion battery packs,” *Int. J. Heat Mass Transf.*, vol. 92, pp. 893–903, 2016, doi: 10.1016/j.ijheatmasstransfer.2015.09.052.

[20] M. Al-Zareer, I. Dincer, and M. A. Rosen, “Novel thermal management system using boiling cooling for high-powered lithium-ion battery packs for hybrid electric vehicles,” *J. Power Sources*, vol. 363, pp. 291–303, 2017, doi: 10.1016/j.jpowsour.2017.07.067.

[21] M. Broussely, J. P. Planchat, G. Rigobert, D. Virey, and G. Sarre, “Lithium-ion batteries for electric vehicles: Performances of 100 Ah cells,” *J. Power Sources*, vol. 68, no. 1, pp. 8–12, 1997, doi: 10.1016/S0378-7753(96)02544-X.

[22] N. Imanishi and O. Yamamoto, “Rechargeable lithium-air batteries: Characteristics and prospects,” *Mater. Today*, vol. 17, no. 1, pp. 24–30, 2014, doi: 10.1016/j.mattod.2013.12.004.

[23] K. Kitoh and H. Nemoto, “100 Wh large size Li-ion batteries and safety tests,” *J. Power Sources*, vol. 81–82, pp. 887–890, 1999, doi: 10.1016/S0378-7753(99)00125-1.

[24] T. S. Bryden, G. Hilton, A. Cruden, and T. Holton, “Electric vehicle fast charging station usage and power requirements,” *Energy*, vol. 152, pp. 322–332, 2018, doi: 10.1016/j.energy.2018.03.149.

[25] R. Philipsen, T. Schmidt, J. Van Heek, and M. Ziefle, “Fast-charging station here, please! User criteria for electric vehicle fast-charging locations,” *Transp. Res. Part F Traffic Psychol. Behav.*, vol. 40, no. 2016, pp. 119–129, 2016, doi: 10.1016/j.trf.2016.04.013.

[26] V. Raveendran, R. Divya, P. C. S. Chandran, and M. G. Nair, “Smart level 2 DC electric vehicle charging station with improved grid stability and battery backup,” *Proc. 2017 IEEE Int. Conf. Technol. Adv. Power Energy Explor. Energy Solut. an Intell. Power Grid, TAP Energy 2017*, pp. 1–6, 2018, doi: 10.1109/TAPENERGY.2017.8397312.

[27] T. Winkler, P. Komarnicki, G. Mueller, G. Heideck, M. Heuer, and Z. A. Styczynski, “Electric vehicle charging stations in Magdeburg,” *5th IEEE Veh. Power Propuls. Conf. VPPC ’09*, pp. 60–65, 2009, doi: 10.1109/VPPC.2009.5289871.

[28] S. Bai, Y. Du, and S. Lukic, “Optimum design of an EV/PHEV charging station with DC bus and storage system,” *2010 IEEE Energy Convers. Congr. Expo. ECCE 2010 - Proc.*, pp. 1178–1184, 2010, doi: 10.1109/ECCE.2010.5617834.

[29] D. Christen, S. Tschannen, and J. Biela, “Highly efficient and compact DC-DC converter for ultra-fast charging of electric vehicles,” *15th Int. Power Electron. Motion Control Conf. Expo. EPE-PEMC 2012 ECCE Eur.*, p. LS5d.3-1-LS5d.3-8, 2012, doi: 10.1109/EPEPEMC.2012.6397481.

[30] S. Negarestani, M. Fotuhi-Firuzabad, M. Rastegar, and A. Rajabi-Ghahnavieh, “Optimal sizing of storage system in a fast charging station for plug-in hybrid electric vehicles,” *IEEE Trans. Transp. Electrif.*, vol. 2, no. 4, pp. 443–453, 2016, doi: 10.1109/TTE.2016.2559165.

[31] A. Y. S. Lam, Y. W. Leung, and X. Chu, “Electric vehicle charging station placement: Formulation, complexity, and solutions,” *IEEE Trans. Smart Grid*, vol. 5, no. 6, pp. 2846–2856, 2014, doi: 10.1109/TSG.2014.2344684.

[32] Y. Xiong, J. Gan, C. Miao, and A. Bazzan, “Optimal Electric Vehicle Fast Charging Station Placement Based on Game Theoretical Framework,” *IEEE Trans. Intell. Transp. Syst.*, vol. 19, no. 8, pp. 71–95, 2018, doi: 10.1142/9789812814500_0005.

[33] T. Chen, K. Kockelman, and M. Khan, “Locating electric vehicle charging stations,” *Transp. Res. Rec.*, no. 2385, pp. 28–36, 2013, doi: 10.3141/2385-04.

[34] S. Funke, A. Nusser, and S. Storandt, “Placement of loading stations for electric vehicles: No detours necessary!,” *J. Artif. Intell. Res.*, vol. 53, pp. 633–658, 2015, doi: 10.1613/jair.4688.

[35] H. Ding, Z. Hu, and Y. Song, “Value of the energy storage system in an electric bus fast charging station,” *Appl. Energy*, vol. 157, pp. 630–639, 2015, doi: 10.1016/j.apenergy.2015.01.058.

[36] M. Gjelaj, C. Traholt, S. Hashemi, and P. B. Andersen, “Cost-benefit analysis of a novel DC fast-charging station with a local battery storage for EVs,” *2017 52nd Int. Univ. Power Eng. Conf. UPEC 2017*, vol. 2017-Janua, pp. 1–6, 2017, doi: 10.1109/UPEC.2017.8231973.

[37] D. Rosewater and A. Williams, “Analyzing system safety in lithium-ion grid energy storage,” *J. Power Sources*, vol. 300, pp. 460–471, 2015, doi: 10.1016/j.jpowsour.2015.09.068.

[38] Z. Rao, Q. Wang, and C. Huang, “Investigation of the thermal performance of phase change material/mini-channel coupled battery thermal management system,” *Appl. Energy*, vol. 164, pp. 659–669, 2016, doi: 10.1016/j.apenergy.2015.12.021.

[39] T. M. Bandhauer, S. Garimella, and T. F. Fuller, “A Critical Review of Thermal Issues in Lithium-Ion Batteries,” *J. Electrochem. Soc.*, vol. 158, no. 3, p. R1, 2011, doi: 10.1149/1.3515880.

[40] A. Farmann, W. Waag, A. Marongiu, and D. U. Sauer, “Critical review of on-board capacity estimation techniques for lithium-ion batteries in electric and hybrid electric vehicles,” *J. Power Sources*, vol. 281, pp. 114–130, 2015, doi: 10.1016/j.jpowsour.2015.01.129.

[41] H. Wenzl *et al.*, “Life prediction of batteries for selecting the technically most suitable and cost effective battery,” *J. Power Sources*, vol. 144, no. 2, pp. 373–384, 2005, doi: 10.1016/j.jpowsour.2004.11.045.

[42] A. G. Tamirat *et al.*, "Highly stable carbon coated Mg2Si intermetallic nanoparticles for lithium-ion battery anode," *J. Power Sources*, vol. 384, no. October 2017, pp. 10–17, 2018, doi: 10.1016/j.jpowsour.2018.02.008.

[43] M. Ye, Y. Xu, and Y. Huangfu, "The structure optimization of lithium-ion battery pack based on fluid-solid conjugate thermodynamic analysis," *Energy Procedia*, vol. 152, pp. 643–648, 2018, doi: 10.1016/j.egypro.2018.09.224.

[44] B. Xia and D. W. Sun, "Applications of computational fluid dynamics (CFD) in the food industry: A review," *Comput. Electron. Agric.*, vol. 34, no. 1–3, pp. 5–24, 2002, doi: 10.1016/S0168-1699(01)00177-6.

[45] F. Romano, L. Marocco, J. Gustén, and C. M. Joppolo, "Numerical and experimental analysis of airborne particles control in an operating theater," *Build. Environ.*, vol. 89, pp. 369–379, 2015, doi: 10.1016/j.buildenv.2015.03.003.

[46] B. Blocken, W. D. Janssen, and T. van Hooff, "CFD simulation for pedestrian wind comfort and wind safety in urban areas: General decision framework and case study for the Eindhoven University campus," *Environ. Model. Softw.*, vol. 30, pp. 15–34, 2012, doi: 10.1016/j.envsoft.2011.11.009.

[47] F. Ladeinde and M. D. Nearon, "CFD applications in the HVAC&R industry," *ASHRAE J.*, vol. 39, no. 1, pp. 44–48, 1997.

[48] M. Dadashzadeh, A. Ahmad, and F. Khan, "Dispersion modelling and analysis of hydrogen fuel gas released in an enclosed area: A CFD-based approach," *Fuel*, vol. 184, pp. 192–201, 2016, doi: 10.1016/j.fuel.2016.07.008.

[49] M. R. Giuliano, A. K. Prasad, and S. G. Advani, "Experimental study of an air-cooled thermal management system for high capacity lithium-titanate batteries," *J. Power Sources*, vol. 216, pp. 345–352, 2012, doi: 10.1016/j.jpowsour.2012.05.074.

[50] X. Li, F. He, and L. Ma, "Thermal management of cylindrical batteries investigated using wind tunnel testing and computational fluid dynamics simulation," *J. Power Sources*, vol. 238, pp. 395–402, 2013, doi: 10.1016/j.jpowsour.2013.04.073.

[51] S. Shahid and M. Agelin-Chaab, "Development and analysis of a technique to improve air-cooling and temperature uniformity in a battery pack for cylindrical batteries," *Therm. Sci. Eng. Prog.*, vol. 5, no. January, pp. 351–363, 2018, doi: 10.1016/j.tsep.2018.01.003.

[52] R. Mahamud and C. Park, "Reciprocating air flow for Li-ion battery thermal management to improve temperature uniformity," *J. Power Sources*, vol. 196, no. 13, pp. 5685–5696, 2011, doi: 10.1016/j.jpowsour.2011.02.076.

[53] H. Sun, X. Wang, B. Tossan, and R. Dixon, "Three-dimensional thermal modeling of a lithium-ion battery pack," *J. Power Sources*, vol. 206, pp. 349–356, 2012, doi: 10.1016/j.jpowsour.2012.01.081.

[54] J. Xie, Z. Ge, M. Zang, and S. Wang, "Structural optimization of lithium-ion battery pack with forced air cooling system," *Appl. Therm. Eng.*, vol. 126, pp. 583–593, 2017, doi: 10.1016/j.applthermaleng.2017.07.143.

[55] A. Greco, D. Cao, X. Jiang, and H. Yang, "A theoretical and computational study of lithium-ion battery thermal management for electric vehicles using heat pipes," *J. Power Sources*, vol. 257, pp. 344–355, 2014, doi: 10.1016/j.jpowsour.2014.02.004.

[56] M. Y. Ramandi, I. Dincer, and G. F. Naterer, "Heat transfer and thermal

management of electric vehicle batteries with phase change materials," *Heat Mass Transf. und Stoffuebertragung*, vol. 47, no. 7, pp. 777–788, 2011, doi: 10.1007/s00231-011-0766-z.

[57] W. Wu, W. Wu, and S. Wang, "Thermal optimization of composite PCM based large-format lithium-ion battery modules under extreme operating conditions," *Energy Convers. Manag.*, vol. 153, no. September, pp. 22–33, 2017, doi: 10.1016/j.enconman.2017.09.068.

[58] T. Mikjaniec, A. Manning, D. Small, and J. VanGilder, "Data center design using improved CFD modeling and cost reduction analysis," *Annu. IEEE Semicond. Therm. Meas. Manag. Symp.*, pp. 97–104, 2011, doi: 10.1109/STHERM.2011.5767185.

[59] N. Serra and V. Semiao, "Comparing displacement ventilation and mixing ventilation as HVAC strategies through CFD," *Eng. Comput. (Swansea, Wales)*, vol. 26, no. 8, pp. 950–971, 2009, doi: 10.1108/02644400910996844.

[60] S. Iizuka, M. Sasaki, G. Yoon, M. Okumiya, J. Kondo, and Y. Sakai, "Coupling strategy of HVAC system simulation and CFD part 2: Study on mixing energy loss in an air-conditioned room," *Proc. Build. Simul. 2011 12th Conf. Int. Build. Perform. Simul. Assoc.*, pp. 2096–2101, 2011.

[61] T. Catalina, J. Virgone, and F. Kuznik, "Evaluation of thermal comfort using combined CFD and experimentation study in a test room equipped with a cooling ceiling," *Build. Environ.*, vol. 44, no. 8, pp. 1740–1750, 2009, doi: 10.1016/j.buildenv.2008.11.015.

[62] T. Yu, H. Yang, R. Xu, and C. Peng, "Simulation Study on Ventilation & Cooling for Main Transformer Room of an Indoor Substation," *J. Multimed.*, vol. 9, no. 8, Aug. 2014, doi: 10.4304/jmm.9.8.1040-1047.

[63] M. K. Herrlin and C. Belady, "Gravity-assisted air mixing in data centers and how it affects the Rack cooling effectiveness," *Thermomechanical Phenom. Electron. Syst. -Proceedings Intersoc. Conf.*, vol. 2006, pp. 434–438, 2006, doi: 10.1109/ITHERM.2006.1645375.

[64] M. K. P. Herrlin, "Airflow and Cooling Performance of Data Centers: Two Performance Metrics," *ASHRAE Trans.*, vol. 114, pp. 182–187, 2008.

[65] J. Cho, J. Yang, and W. Park, "Evaluation of air distribution system's airflow performance for cooling energy savings in high-density data centers," *Energy Build.*, vol. 68, no. PARTA, pp. 270–279, 2014, doi: 10.1016/j.enbuild.2013.09.013.

[66] M. K. Herrlin and K. Khankari, "Method for optimizing equipment cooling effectiveness and HVAC cooling costs in telecom and data centers," *ASHRAE Trans.*, vol. 114 PART 1, no. Fluent, pp. 17–21, 2008.

[67] S. Murakami, S. Kato, and T. Kim, "INDOOR CLIMATE DESIGN BASED ON FEEDBACK CONTROL OF HVAC COUPLED SIMULATION OF CONVECTON , RADIATION , AND HVAC CONTROL FOR ATTAINING GIVEN OPERATIVE TEMPERATURE Shuzo Murakami , Shinsuke Kato , and Taeyeon Kim Institute of Industrial Science , University," pp. 1–8.

[68] "Keystone Through-the-Wall Air Conditioners Specification Sheet." .

[69] "Keystone Through Wall Air Conditioners - KSTAT10-2HC." [Online]. Available: https://www.compactappliance.com/keystone-through-wall-air-

conditioners/KSTAT10-2HC.html. [Accessed: 31-Mar-2020].

[70] ANSYS, “Fluent User’s Guide,” 2019.

[71] M. Ibrahim, “Design and Analysis of an Active Underbody Aerodynamic Device for Tractor Trailers,” University of Ontario Institute of Technology, 2018.

[72] F. R. Menter, “Two-equation eddy-viscosity turbulence models for engineering applications,” *AIAA J.*, vol. 32, no. 8, pp. 1598–1605, 1994, doi: 10.2514/3.12149.

[73] S. Shahid and M. Agelin-Chaab, “Analysis of Cooling Effectiveness and Temperature Uniformity in a Battery Pack for Cylindrical Batteries,” *Energies*, vol. 10, no. 8, p. 1157, Aug. 2017, doi: 10.3390/en10081157.

[74] ANSYS, “Lecture 2 Introduction to CFD Methodology,” 2010.

[75] M. Lanfrit, “Best practice guidelines for handling Automotive External Aerodynamics with FLUENT,” vol. 2, pp. 1–18, 2005.

[76] “Thermoplastics - Physical Properties.” [Online]. Available: https://www.engineeringtoolbox.com/physical-properties-thermoplastics-d_808.html. [Accessed: 14-Apr-2020].

[77] “Thermal Properties of Metals, Conductivity, Thermal Expansion, Specific Heat | Engineers Edge.” [Online]. Available: https://www.engineersedge.com/properties_of_metals.htm. [Accessed: 14-Apr-2020].

[78] B. Sanborn and B. Song, “Frequency-based Impact Energy Dissipation in Silicone,” 2016.

[79] “Properties: Silicone.” [Online]. Available: https://www.azom.com/properties.aspx?ArticleID=920. [Accessed: 14-Apr-2020].

[80] R. Ferreira and E. Alves, *River Flow 2006, Two Volume Set: Proceedings of the International Conference*, vol. 1. Boca Raton: CRC Press, 2006.

[81] “Specific Heat of some common Substances.” [Online]. Available: https://www.engineeringtoolbox.com/specific-heat-capacity-d_391.html. [Accessed: 14-Apr-2020].

[82] “Thermal Conductivity of selected Materials and Gases.” [Online]. Available: https://www.engineeringtoolbox.com/thermal-conductivity-d_429.html. [Accessed: 14-Apr-2020].

[83] “Density of Polypropylene.” [Online]. Available: https://www.aqua-calc.com/page/density-table/substance/polypropylene-coma-and-blank-crystalline. [Accessed: 14-Apr-2020].

[84] “Polypropylene - online catalogue source - supplier of research materials in small quantities - Goodfellow.” [Online]. Available: http://www.goodfellow.com/E/Polypropylene.html. [Accessed: 14-Apr-2020].

[85] “Scientific Principles.” [Online]. Available: http://matse1.matse.illinois.edu/ceramics/prin.html. [Accessed: 14-Apr-2020].

[86] “Melamine Formaldehyde (MF) :: MakeItFrom.com.” [Online]. Available: https://www.makeitfrom.com/material-properties/Melamine-Formaldehyde-MF. [Accessed: 14-Apr-2020].

[87] “(rbf-morph) ANSYS Fluent Add-On.”

Appendix A: Validation

Validation data was provided by eCAMION Inc, where temperatures were measured by thermocouples placed at selected locations within the charging system as indicated in Table A-1. The data shown represents the charging and discharging periods that occurred over 17 hours. The charging and discharging period is shown in Figure A-1 where it can be examined that the recorded state of charge is from 0% to 65%. As seen from Figure A-1, the measurement begins at 0% SOC where it abruptly reaches 40%, subsequently plateauing. After this, it drops to 30% briefly, where it quickly rises again to 55%. Following this rise, it quickly drops to 45% SOC. At 45% SOC, there is not much change as the readings remain in the region, as the recorded SOC can be observed to be discharging slowly. After over 500 of the measurements are completed it quickly charges to 65% and the data set ends. In all, 1084 temperature data points were recorded. The experimental system power output was examined and compared with the power output from the simulation data. Each component was considered to impact the overall power output from the charging system. In order to reflect the power output from the simulation data with the experimental data the boundary conditions were changed for each component. This method was able to appropriately reflect the temperatures during the charging and discharging periods identified in Figure A-1. Figure A-2 shows the resulting simulation temperatures in comparison to the experimental data. The graphs clearly show an excellent match between the simulation and experimental data.

The steady-state simulation data was also extracted and compared with the average temperature from the experimental data. Table A-2 compares the average measured temperatures and steady-state simulation temperatures. As shown, the resulting percentage

differences are all less than 7%, which shows that the results are consistent and there is a good match. In addition, Figure A-3 displays the measured temperatures from the charge and discharge cycles and the resulting steady-state temperatures. It is evident that the simulation results do not capture the temperature peaks but the magnitudes match quite well. Based on these validation analyses, it can be concluded that the simulation results are well validated.

Table A-1. Thermocouple name and location

Thermocouple Name	Thermocouple Location
Temp_4	Roof
Temp_5	On an electrical panel
Temp_6	Battery racks
Temp_7	Over PLC

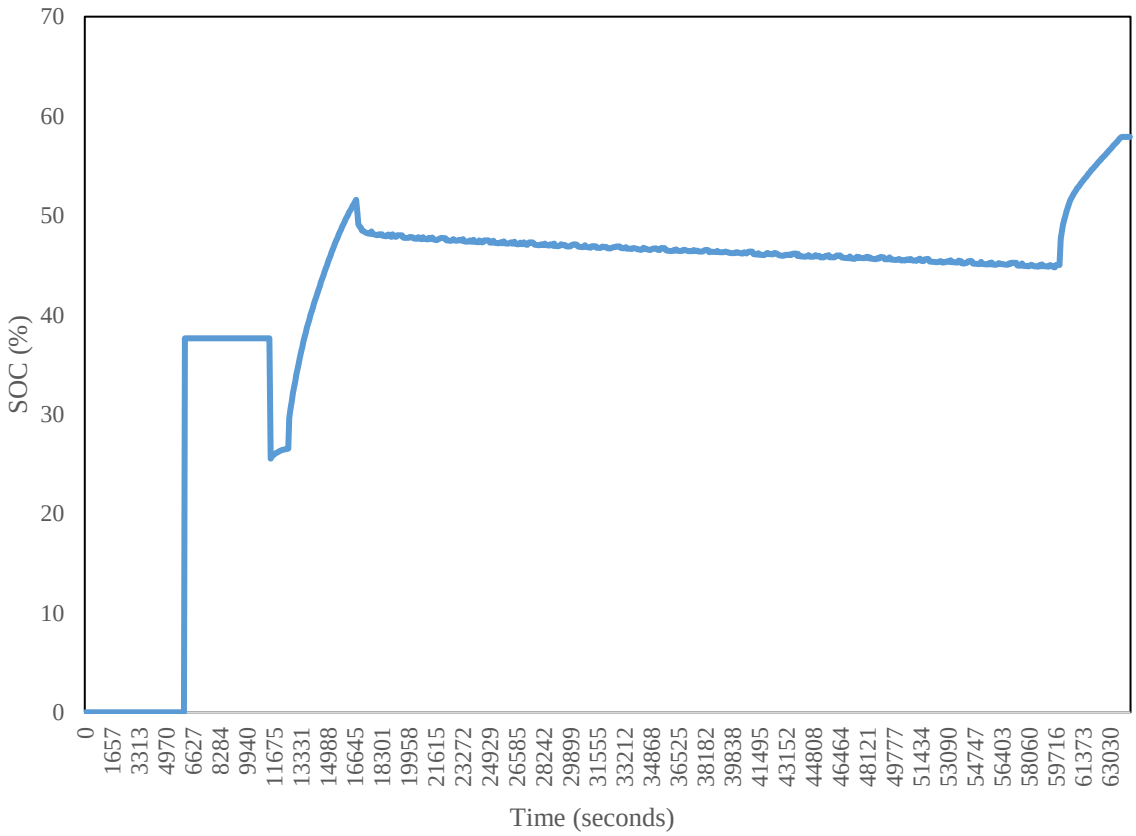

Figure A-1. Recorded SOC over time in seconds

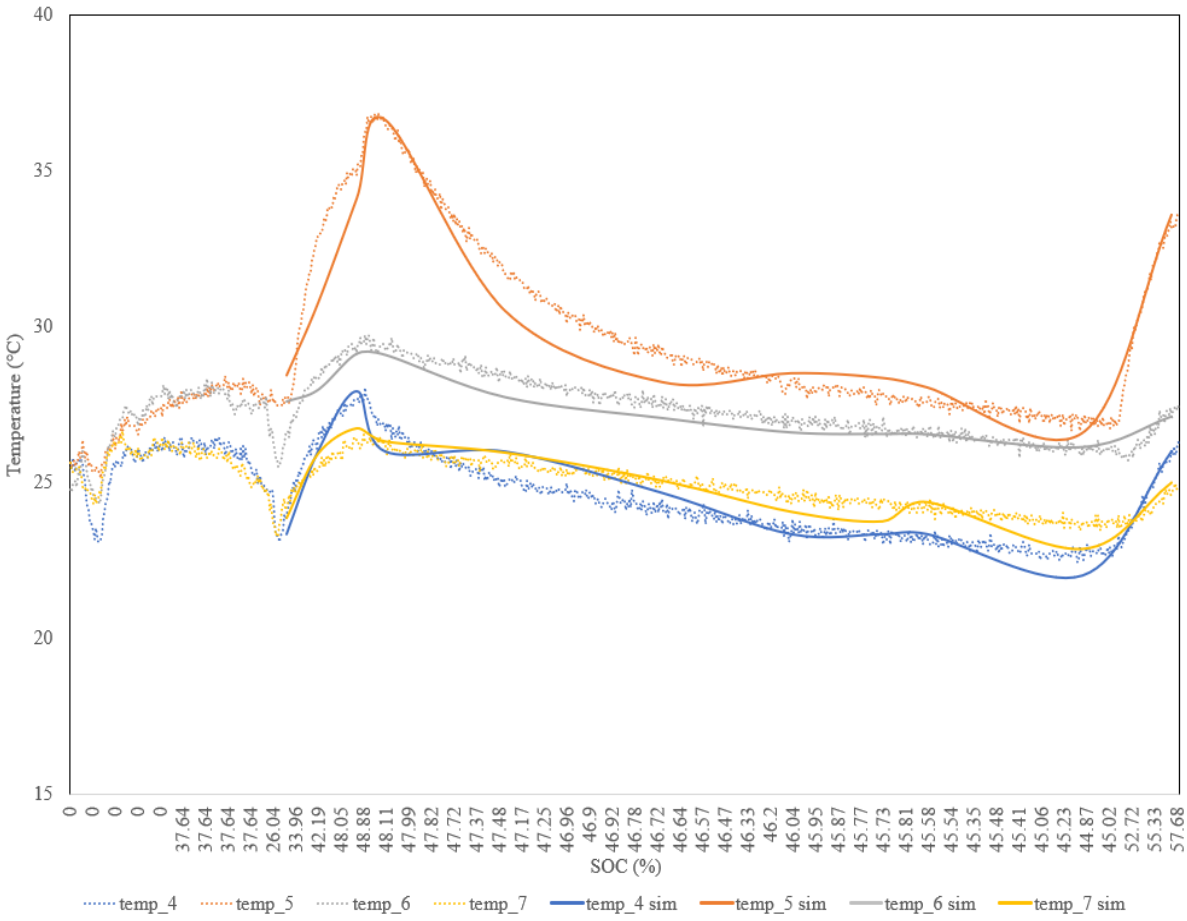

Figure A-2. Simulation temperature plotted with experimental temperature over SOC, (blue) temp_4, (orange) temp_5, (grey) temp_6, (yellow) temp_7

Table A-2. Measured temperature data and resulting simulation temperature data comparison (steady-state)

Thermocouple	Average Measured Temperature (℃)	Steady-State Simulation Temperature (℃)	Percentage Difference (%)
Temp_4	23.92	24.81	3.70%
Temp_5	29.32	30.02	2.38%
Temp_6	26.41	27.46	3.99%
Temp_7	24.33	25.87	6.32%

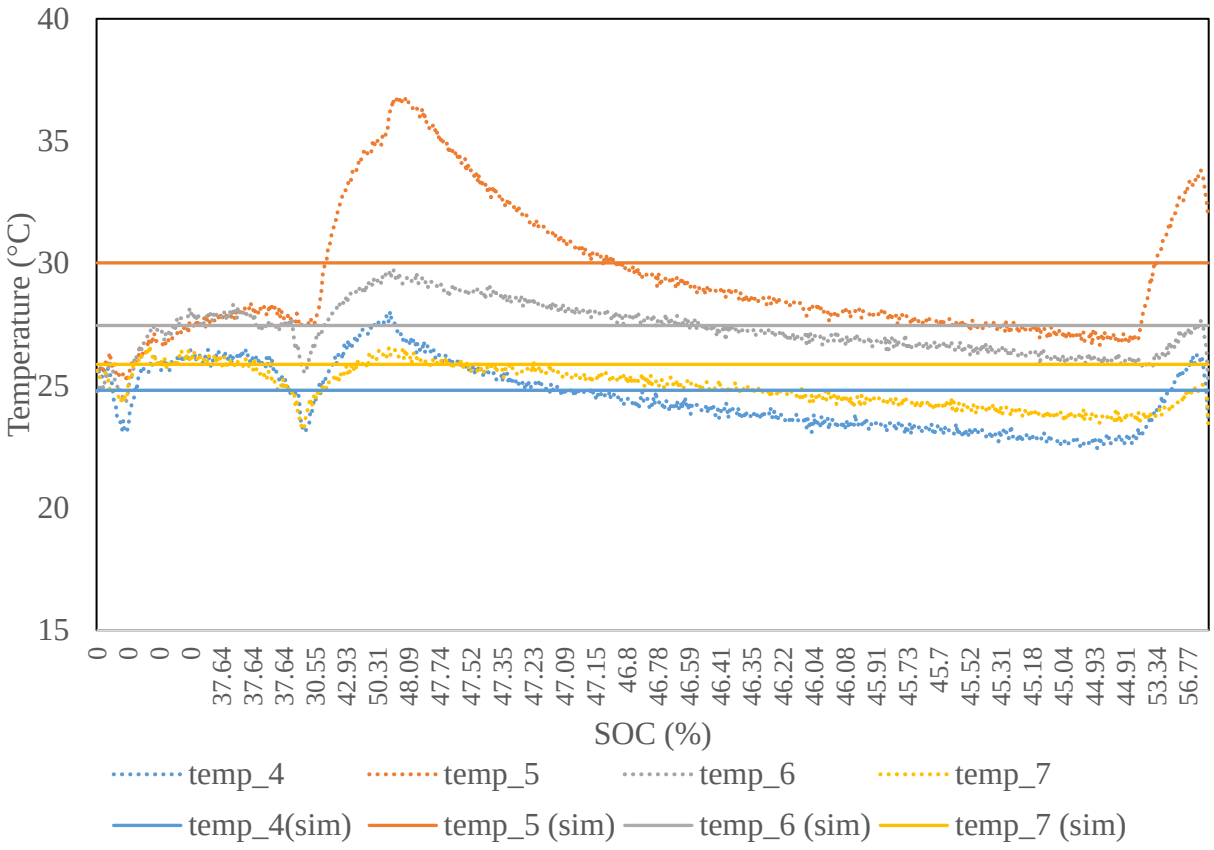

Figure A-3. Steady-state simulation temperature plotted with experimental temperature over SOC, (blue) temp_4, (orange) temp_5, (grey) temp_6, (yellow) temp_7